Study of QCD Critical Point at FAIR Energies

Dissertation

submitted for the award of the degree of

Master of Philosophy

in

Physics

by

Suraya Bashir

Under the Supervision of

Dr. M. Farooq Mir

Department of Physics,

University of Kashmir, Srinagar, 190 006

September, 2012

Post Graduate Department of Physics, University of Kashmir, Srinagar.

Certificate

This is to certify that the dissertation entitled "**Study of QCD Critical Point at FAIR Energies**" submitted by **Suraya Bashir**, in partial fulfilment for the award of the degree of **Master of Philosophy** in **Physics**, is the original research work carried out by her under our supervision and guidance. It is further certified that the dissertation has not been submitted for the award of M. Phil or any other degree to this University or any other University. The scholar has attended the department for statutory period as required under rules.

Dr. M. Farooq Mir   Prof. Sheikh Javid Ahmad

(*Supervisor*)   (*Head of the Department*)

Acknowledgements

First of all, I am thankful to the "Almighty Allah" for giving me patience and persistence and showering his endless blessings to carry out my work successfully.

I would like to take this opportunity to thank all those people who contributed to the completion of this work. First, I would like to gratefully acknowledge and extend my heartfelt gratitude to my Research Supervisor, **Dr.M. Farooq Mir** for introducing me into the field of High Energy Physics and offering me the great opportunities to participate in other collaborating centres. I appreciate his continuous supervision and support in my research work. His constant guidance helped me a lot to finish this research work in time.

I would like to express my thanks to **Prof. Sheikh Javid Ahmad**, Head of Physics Department, University of Kashmir for providing me with necessary infrastructure, help, support and other facilities during my tenure of research. I also extend my thanks to the whole teaching faculty of the department for their generous help whenever needed.

My sincere thanks to **Dr. Subhasis Chattopadhayay**, an eminent experimental particle physicist, VECC, Kolkata for his valuable suggestions and timely help in the completion of my analysis work in appropriate time. I greatly benefited from their profound and broad understanding of physics.

My special thanks are also to our CBM Collaborators especially **Dr. Y.P. Viyogi**,and **Dr. Zubyer Ahmad** from VECC, for their guidance, academic

Suraya Bashir

Dedicated

to

My Parents

and

Sisters

Contents

List of Figures

List of Tables

Chapter 1

Heavy Ion Collision

1.1 Introduction

In the course of the past century, unprecedented progress has been achieved in our understanding of the fundamental laws of nature and their implications for the complex structure of the world at all scales,ranging from the substructure of elementary hadrons to the universe as a whole. The revolutionary concepts of special and general relativity and quantum mechanics have resolved many of the puzzling experimental findings that had accumulated by the beginning of the 20th century, such as the particle wave duality.

Our universe originated from "Big Bang" in a state of almost infinite energy density and temperature . Immediately after the Big Bang, the energy density in our universe was so high that hadrons (which are colour singlet bound states quarks, anti-quarks and gluons), could not be formed. Instead these quarks and gluons were de confined and permeated the entire universe in a thermalized state. High Energy Physics searches for the fundamental particles and forces which build the world around us.

The comprehension of quantum Chromodynamics (QCD), the theory which describes strong interaction and its features is an important task of modern physics. The theory is instrumental in understanding both, the early universe as well as the nature of objects in the universe in its currents form (such as neutron stars). One of the main features of QCD is "asymptotic freedom". Contrary to most fields in

physics (e.g electrodynamics), here interactions are only small as long as only short distances are considered and become stronger for increased distances.

A great part of the research on QCD is dedicated to the phase diagram of QCD, the diagram which maps the physically preferred phase as a function of temperature and density/chemical potential as shown in fig 1.1. It is known that, at
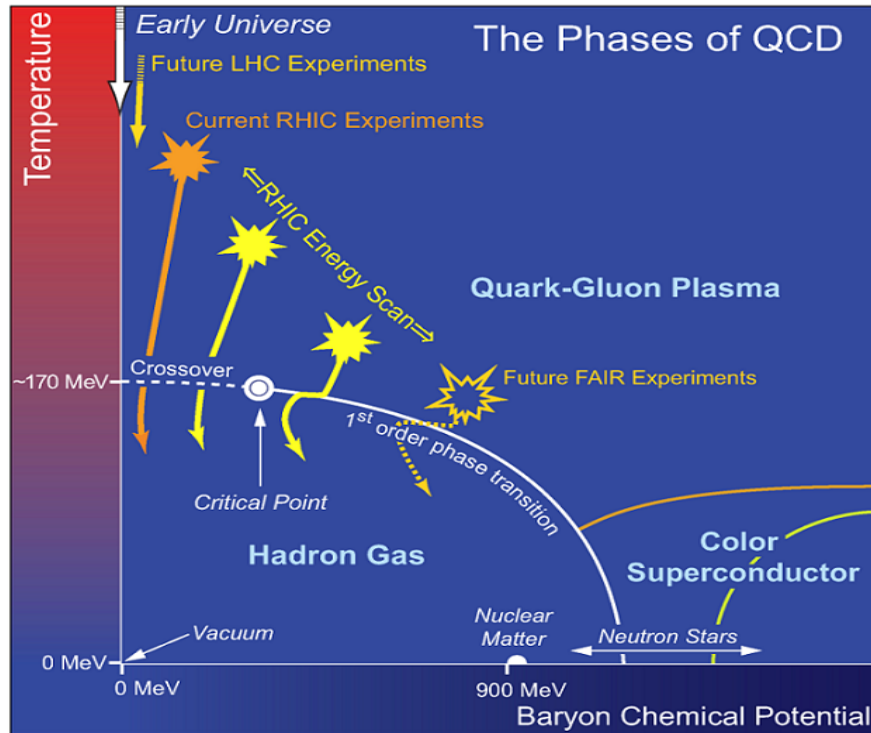
Figure 1.1: *The phases of QCD*

low temperature and low chemical potential, the phase diagram of QCD is governed by the hadronic phase, where only bound states of two or three quarks are observed. In the realm of high temperature and/or high chemical potential, on the other hand, the phase diagram is governed by the quark gluon plasma (QGP), where quarks are not confined in bound states [1]. In addition, a color-superconducting (CSC) phase is predicted for the region of low temperature and high chemical potential [1, 2]. The transition between these phases may happen in different manner. While the order parameter defining the phases is known to change from its hadronic phase

value to its QGP phase value continuously (cross-over) at high temperature and low chemical potential, a discontinuous transition (first-order phase transition) is found for high chemical potential and moderate temperature. It is still subject to speculation whether a cross-over can also be found for the transition from the hadronic phase to the CSC phase [3]. The point where the type of phase transition changes is commonly referred to as critical point (CP). Since the CP represents an important landmark of the phase diagram, it is investigated not only in theoretical physics but also in heavy-ion collision experiments conducted at numerous research facilities worldwide as the Brookhaven National Laboratory (BNL), the European Organization for Nuclear Research (CERN) and the GSI Helmholtz Centre for Heavy Ion Research (GSI).

In order to interpret such experiments, it is crucial to know which observables are suitable probes for the critical point. For instance, it is known that susceptibilities, i.e quadratic fluctuations with long wave length diverge at the critical point (CP) [4] and they are thus considered possible probes for heavy ion collision experiments [5, 6]. Furthermore fluctuations of third and fourth order have been suggested as probes for the critical point (CP) recently. It has been argued that they may offer better probes than susceptibilities, since (i) a change of sign in the third moments might provide additional information on the phase diagram [7] and (ii) higher-order fluctuations diverge more radically than susceptibilities at the critical point [8].

In the present study, we want to contribute to the discussion of the multiplicity fluctuations as a probe for the CP and also want to address charge particle multiplicity fluctuations. For this reason, we will employ the Monte Carlo model to calculate the fluctuations near the critical point and analyse the critical mode, which leads to the divergence at the critical point (CP).

1.2   The Standard model

Our present understanding of the elementary particles and forces in nature are described by the Standard Model. The SM is a relativistic quantum field theory in which matter is described by fermions, which are spin 1/2 particles, and the forces between them by mediating bosons with integer spin. The fermions are point like

objects and consist of the leptons and the quarks. In the theory, hadrons consist of quarks, which are arranged in three generations. The generations are symmetric except for mass as shown in fig 1.2. The quarks carry fractional electromagnetic charge, as well as "color" which is the charge of the strong nuclear force. The mediators of the strong nuclear force are called gluons, which are themselves colored.

Figure 1.2: *The fermions and bosons of the Standard Model of particle physics*

According to the Standard Model, matter is composed from twelve basic building blocks called fundamental particles, governed by four fundamental forces. Particles in the Standard Model are generally separated in fermions and bosons and the forces in four types: electromagnetic force, weak force, strong force and gravitational forces. Fermions are elementary particles of spin-1/2 and consist the building blocks of matter. The interaction among the particles is mediated by bosons which are particles with spin 1. Fermions are classified, according to how they interact, into quarks (up, down, charm, strange, top, bottom) and leptons (electron, μ, τ and the corresponding three neutrinos). Quarks carry electric and colour charge

Interaction	Mediators	Range	Typical lifetime	Typical coupling
Strong	8 gluons	$1fm \simeq 1m\phi$	18^{-23}	1
Electromagnetic	photon	∞	$10^{-20} \sim 10^{-16}$	10^{-2}
Weak	$W^{\pm}, Z^0$	$1/M_W$	10^{-12} or longer	10^{-6}
Gravitational	G	∞	∞	10^{-38}

Table 1.1: *Forces and their interactions. The lifetime is referred to particles decaying via strong, electromagnetic and weak interactions*

and can interact with the electromagnetic and strong interaction respectively. They also carry a weak isospin which allows them to interact with the weak force too. The leptons cannot interact with the strong force because they do not carry colour charge. They all interact with the weak force and only three of them (e, μ, τ) carry electric charge which allows them to interact with the electromagnetic force. Table-1 describes the properties of these interactions. The theory that describes the strong interaction is called Quantum Chromodynamics (QCD).

1.3   Quantum Chromodynamics

Quantum Chromodynamics (QCD)introduced by Gell - Mann in 1972 [9] is developed to describe the strong interaction which is one of the two parts of the Standard Model Theory of particle physics. The other one is so called the electro-magnetic and weak interactions can be described in a uniform way.

QCD [10] is a renormalized non-abelian guage theory based on the $SU(3)_c$ group. The subscript c denotes the quantum number - color, which is an exact symmetry. Quarks belong to a color triplet representation in this symmetry while the hadronic states are assumed to be color singlet in QCD. There are three different charges ("colors") red, green and blue compared to only one charge (electric) in quantum electrodynamics (QED) - the guage theory describing electromagnetic interaction. Due to the non - abelian character of the SU(3)c group, the invariant QCD Lagrangian requires guage (gluon) self interactions which do not appear in QED. There are eight different gluons and gluon exchange can change the color of a quark but not its flavour. Multi-gluons, such as 3 or 4 gluons interactions are

allowed in QCD. The most of the two basic properties of the QCD theory are

(i)Asymptotic freedom and

(ii) Confinement.

1.3.1 Asymptotic Freedom and Confinement

Confinement specifies that free quarks are unobservable and that only colorless objects, such as the proton or pion, can be seen in the laboratory. Although analytically unproven, the property is generally attributed to the idea that the potential energy increases infinitely as quarks are pulled infinitely for apart. It is therefore more advantageous, from an energy perspective, to create quark-anti-quark pairs from the vacuum to form colorless objects when the quarks are being pulled apart.
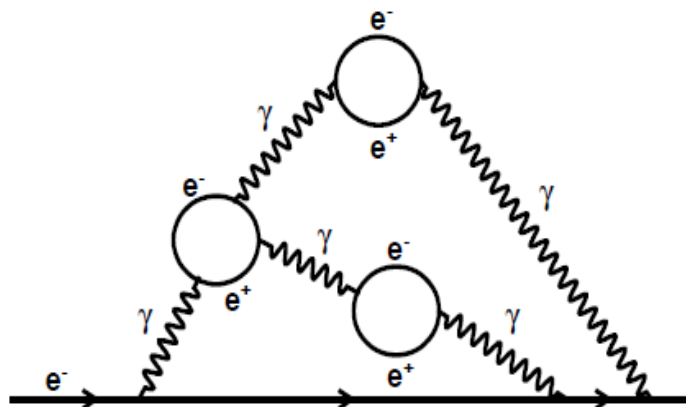
Figure 1.3: *Electric charge screening in QED. The initial electron radiates a photon which splits into electron-positron pairs. The positrons are attracted to the original electron the electrons are repelled. This shielding reduces the measured charge of the original electron.*

To understand asymptotic freedom,it is useful to draw an analogy to QED, an Abelian theory in which the photons do not interact with each other. Imagine that one wants to measure the charge of an electron in a vacuum. This electron, however, can radiate photons which then split into electron-positron pairs. The positrons of the electron-positron pairs are attracted to the original electron and the electrons are repelled (see fig 1.3). This creates an effect called screening in which

the measured effective charge of the electron is reduced as the distance between the observer and the electron increases. The analogues screening effect happens for color charge in QCD when a quark emits gluons which then split into quark-anti-quark pairs as shown in fig 1.4(a). However, because of the self-coupling of gluons in QCD, the gluons can also radiate additional gluons as shown in fig 1.4(b). Since color charges like to be surrounded by charges of a similar color the latter effect dominates and thus the strength of the color charge decreases the closer one comes to the original quark, a property called **asymptotic freedom**.
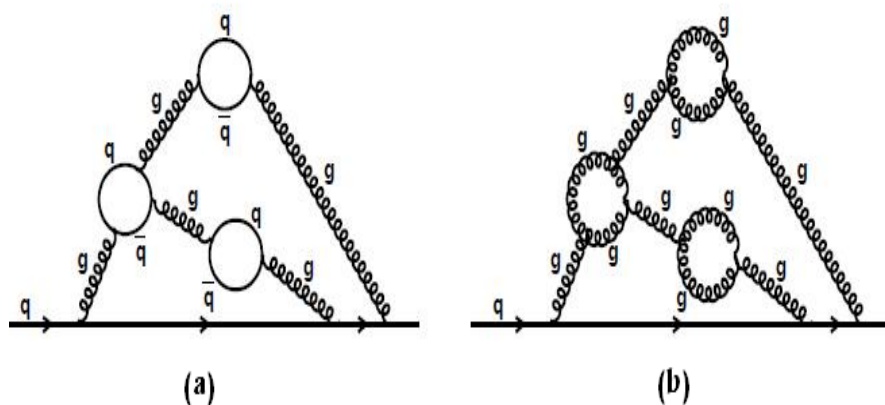
Figure 1.4: *Color charge screening in QCD: (a) The initial gluon can radiate a gluon which splits quark-anti-quark pairs in analogy to screening in QED. (b) The gluons may also split into gluon-gluon pairs.*

1.3.2 Perturbative QCD

As will appear in the following sections, asymptotic freedom is the perturbative concept. Yet, as searches for free quarks, let alone gluons, continued to give null results, it became evident that the perturbation theory of quantum chromodynamics had to be approached somewhat differently than, that of, say, quantum electro-dynamics. The usual S matrix and cross sections for isolated quarks and gluons in QCD all vanish, completely replaced by bound-state dynamics. This is the hypothesis of "confinement". After some time it also became obvious that although asymptotic freedom is a perturbative prediction, confinement is not. The use of

perturbation theory in quantum chromodynamics, that is, "perturbative QCD", or pQCD, therefore developed rather slowly and even haltingly, amid considerable scepticism. Nevertheless, many predictions of the theory, primarily but not exclusively associated with inclusive processes, do not depend upon its long-distance behaviour. These short-distance predictions are the realm of perturbative QCD.

Since QCD remains an "unsolved" theory, with no single approximation method applicable to all length scales, the justification for the use of perturbative QCD rests in large part directly on experiment. In this regard, many of us remember vividly the rapid transformation of quantum chromodynamics from a promising but controversial candidate theory to a full-fledged part of the Standard Model, taken perhaps too confidently for granted. In this transformation, the achievements of lattice-based numerical studies also played an important role.

1.3.3 Lattice QCD

Lattice QCD [11] is a well-established non-perturbative approach to solve the QCD theory of quarks and gluons exactly from first principle and without any assumptions. It is a lattice gauge theory formulated on a grid or lattice of points in space and time. Most importantly, lattice QCD provides a framework for investigation of non-perturbative phenomena such as confinement and quark gluon plasma formation, which are intractable by means of analytic field theories.

Lattice QCD calculations often involved analysis at different lattice spacing to determine the lattice-spacing dependence, which can then be extrapolated to the continuum. On the other hand, the calculation power is limited, which requires a smart use of the available resources. One needs to choose an action which gives the best physical description of the system, with minimum errors, using the available computational power. The limited computer resources force one to use physical constants which are different from their true physical values, such as quark masses are steadily going down, but to-date they are typically too high with respect to the real value.

1.3.4 Confinement and Chiral Symmetry Breaking

Confinement is the physical phenomenon that color charged particles such as quarks, cannot be isolated, and therefore cannot be directly observed. Intuitively, confinement is due to the force-carrying gluons having color charge. As any electrically-charged particles separate, the electric fields between them diminish quickly, allowing electrons to become unbound from atomic nuclei. However, as two quarks separate, the gluon fields from narrow tubes (or strings) of color charge, which tend to bring the quarks together as through they were some kind of rubber band. This is quite different in behaviour from electrical charge. Because of this behaviour, the color force experienced by the quarks in the direction to hold them together, remains constant, regardless of their distance from each other. The color force between quarks is large, even on a macroscopic scale, being on the order of 100,000 newtons. As discussed above, it is constant and does not decrease with increasing distance after a certain point has been passed. In fig 1.5, when two quarks become
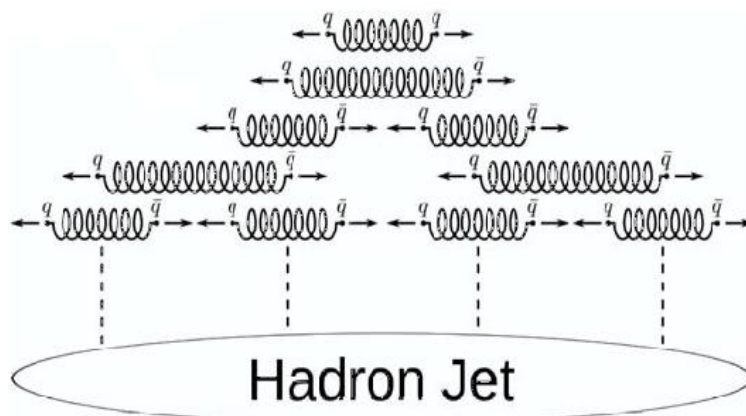
Figure 1.5: *Schematic of quark confinement. The color force favors confinement because at a certain range it is more energetically favourable to create a quark-antiquark pair than to continue to elongate the color flux tube [12].*

separate, at some point it is more energetically favourable for a new quark anti quark pair to spontaneously appear, than to allow the tube to extend further. As a result of this when quarks are produced in particle accelerators instead of seeing the individual quarks in detectors, scientists see particle -antiparticle pairs or jets

of many color -neutral particles (mesons and baryons), clustered together. This process is called hadronization formation, or string breaking and is one of the least understood processes in particle physics.

In the absence of quark masses, the QCD Lagrangian can be split into two independent sectors: the left and right handed components [13]. This Lagrangian is invariant under chiral symmetry transformations. This symmetry which is the extension of classical SU(3), is a global $SU_L(n_f) \times SU_R(n_f)$ symmetry for n_f massless quark flavours. However, it is spontaneously broken in the vacuum in the Nambu Goldstone modes of QCD: their small masses being generated by the quark - mass matrix which explicitly breaks the global chiral symmetry of the QCD Lagrangian.

1.4   Heavy Ion Collisions

In th early 80's lattice QCD theorists proposed [14] that their exist a deconfined phase of quarks and gluons t a high temperature region of the theory. This phase is nowadays referred to as the Quark Gluon Plasma (QGP). One can imagine this phase as a system where the quarks and gluons have such high energies, that the asymptotic freedom of QCD allows them to travel freely in this medium. However, as one might expect, the experimental verification of such matter was still for away as experiments capable of producing it had to be designed and built.

The first hadron colliders ISR (Intersecting Storage Rings) and SPS (Super Proton Synchrotron) at CERN (European Centre for Nuclear Research) as well as the later Tevatron at Fermi-lab collided mainly protons with fixed targets or with anti-protons and, although they made other great particle physics discoveries, they were not ideally suited for QGP production. It took until the year 2000 that RHIC (Relativistic Heavy Ion Collider), a dedicated heavy ion collider, started taking data at BNL (Brookhaven National Laboratory) and now after a decade of running RHIC has provided compelling evidence that indeed QGP exists and can be produced in laboratory conditions. With the continuing RHIC experiments, the LHC (Large Hadron Collider) heavy ion program is about to start, attempt to produce hotter and larger volumes of QGP with longer lifetimes. Further more there comes the CBM (Compressed Baryonic Matter) experiment at FAIR (Facilities for Anti-Proton and Ion Research) facility in Germany which is supposed to probe the

high net baryon density region of the QCD phase diagram.

With respect to the properties of hadronic matter, the chirally broken phase occurs at low temperature and or low densities of the phase diagram. Much like the spontaneous magnetisation in a ferromagnet, though, it is expected that the chiral symmetry breaking will gradually weaken as the temperature or the density is increased. This eventually leads to novel phase of strongly interacting matter in which chiral symmetry is restored.

The opportunity to analyse such forms of matter in all its facets in the laboratory is possible only by colliding two heavy nuclei so that they inter-penetrate and compress but also heat each other due to the microscopic collisions.

In collisions at the very high energies characteristic of the collider facilities, a large number of newly created particles will fill the collision zone which by far surpasses the number of incident particles. As the newly created particles are balanced with respect to their matter-anti-matter content, the net baryon density is relatively small in such matter.

It is obviously a difficult task to anticipate the outcome of such collisions, to identify the novel physics phenomena they may occur and to determine how they are best observed.

1.4.1 Collision geometry and dynamics
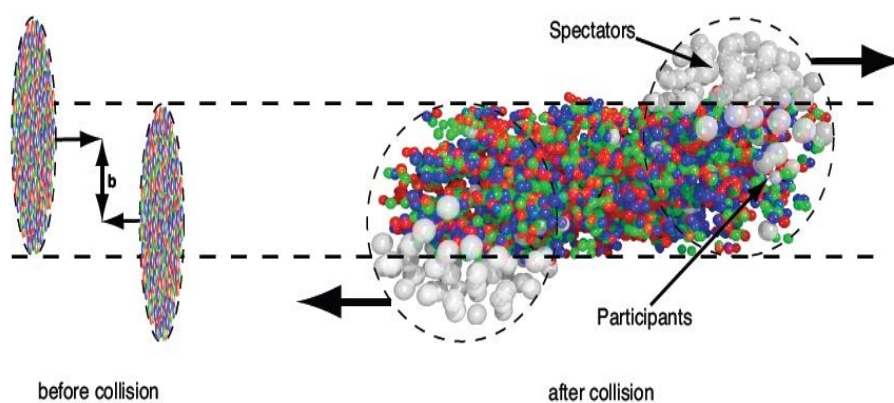
Figure 1.6: *Perspective view of the nuclear collision geometry.*

Figure 1.6 contains views of the nuclear collision geometry from different angles.The nuclei, represented as spheres, collide at an impact parameter b > 0 (in the figure). The parts of the two nuclei which overlap/collide (colored in figure) form the so-called participant region while the rest of the nuclei is called the spectator region. At relativistic energies, the spectator parts of the nuclei move apart and fragment in a very narrow cone around their original direction. The participant region has a very different behaviour which is schematically illustrated in figure 1.7. There is not a clear delimitation for the steps in the evolution of the participant region from a nuclear collision but the sketch in fig 1.6 gives at least a temporal hierarchy.

Right before the collision, the two approaching Lorentz contracted nuclei are in a state which is still under vivid debates. The observed suppression of high transverse momentum particles seen at forward rapidity in d+Au collisions at $\sqrt{S_{NN}} = 200$ GeV [15] gave rise to the idea that the energetic incoming nuclei are in a state called Color Glass Condensate (CGC) [16]. The partonic stage occurs in the first

Initial state   Partonic stage   Hydrodynamic expansion   Mixed phase   Hadronic phase
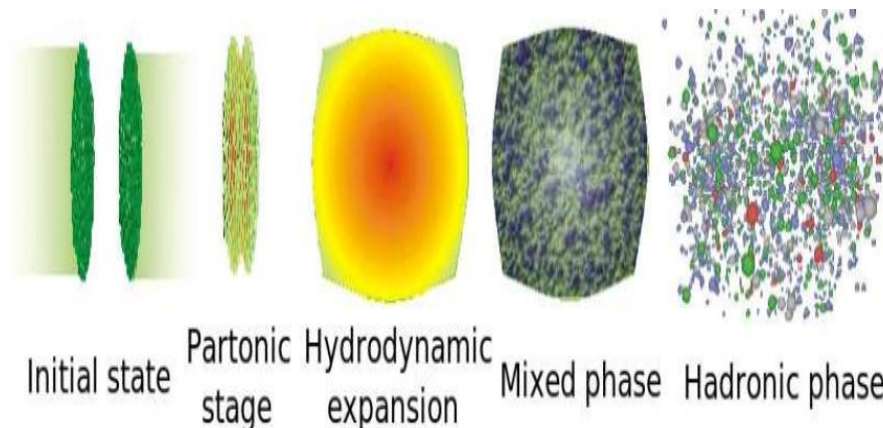
Figure 1.7: *Schematic view of the nuclear collision time evolution. Art is courtesy of S.A.Bass.*

instants of the collision. All the hard interactions between the incoming partons (quarks and gluons) take place now resulting in the production of high transverse momentum jets and heavy quarks. The multi-particle production leads to the formation of a very dense and hot medium with a mean free path much smaller than the nuclear radius. It is believed that this system thermalizes very quickly (t $\sim$ 1

fm/c) and starts to expand due to huge pressure gradients. This motivates the supposition that after the initial step, the nuclear fireball expands hydrodynamically. It is during this stage, which lasts for 10 fm/c, that the nuclear matter is expected to exist in the deconfined state named QGP.

After the nuclear fireball has expanded and cooled sufficiently, the lower densities force matter to hadronize (quarks get confined in bound states).Since at RHIC energies, this transition is expected to be a smooth cross over (second or higher order phase transition), there should be a stage when the nuclear matter exists in a phase which is a mixture between deconfined and confined matter. When the temperature lowers further, the nuclear matter hadronizes completely and after some time becomes a gas of free streaming particles.

1.4.2 Global measurements in relativistic collisions

One of the first questions that must be asked in relativistic heavy ion collisions is how much of the initial energy is available for particle production? This can be found by measuring the rapidity density of the number of baryons minus the number of antibaryons. Knowing that initially all the baryons (protons and neutrons) had the beam rapidity and using the baryon number conservation law, one can extract the amount of stopping from the average rapidity loss. An illustration of the net-proton rapidity distributions at three colliding energies is shown in fig 1.8(a). It is very visible how the collision dynamics changed with energy. At AGS energies, the initial baryons lost almost all their initial momentum and were shifted to mid-rapidity. At top SPS energy, net proton distributions shows a double hump structure representing the fragmentation peaks of the two colliding nuclei. At top RHIC energy, the initial protons passed almost completely through each other leaving a net-baryon poor region at mid-rapidity. At this energy,$\sqrt{S_{NN}} = 200$ GeV, it was found that as much energy as 73 ± 6 GeV per nucleon out of the initial 100 GeV is released in the collision region and is available for particle production [17]. By measuring the charged particle pseudo-rapidity density and the average transverse momentum one can calculate the energy density reached in the collision by using the Bjorken estimate [19]:

$$\epsilon = \frac{1}{\pi R^2 \tau} \frac{d < E_T >}{dy} \qquad (1.1)$$
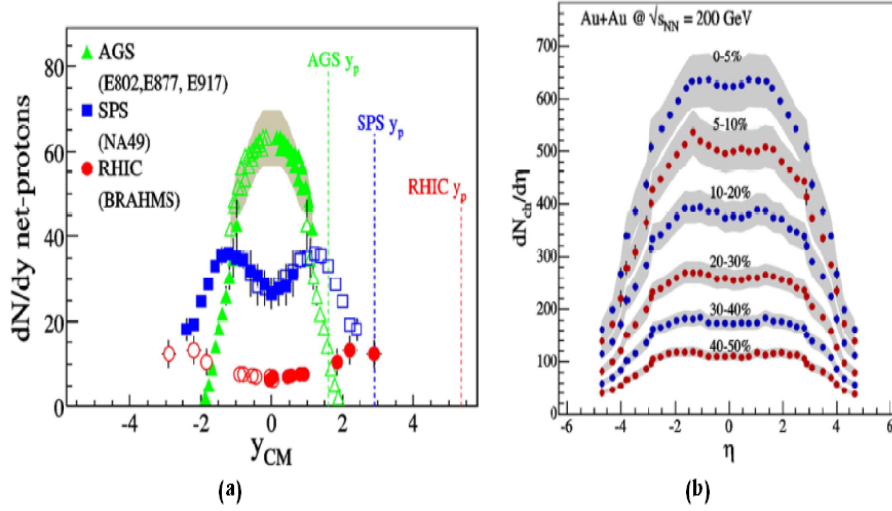
Figure 1.8: *(a) Net-proton (dN/dy(B) $-$ dN/dy($\overline{B}$)) rapidity density in central collisions at top AGS energy, top SPS energy and top RHIC energy [16]. (b) Charged particle pseudo-rapidity density [18].*

Where R is the effective radius of the overlapping disk between the colliding nuclei, and τ is the formation time of the plasma usually taken to be 1 fm/c as a conservation estimate.

1.5   Quark Gluon Plasma

The quark gluon plasma is a state of the extremely dense matter with the quarks and gluons being its constituents. Soon after the Big Bang the matter was just in such a phase. When the universe was expanding and cooling down the quark - gluon plasma turned into hadrons - neutrons and protons, in particular - which further formed the atomic nuclei. The plasma is not directly observed in Nature nowadays, but the astrophysical compact objects as the neutron stars may conceal the quark gluon suggest in their dense centres. The most exciting however re the prospects to study the plasma in the laboratory experiments. A broad research program of the heavy ion collision, which provide a unique opportunity to produce the quark-ion collisions, which provide a unique opportunity to produce the quark - gluon droplets in the terrestrial conditions, is under way. While the question,

whether the plasma is already produced with the currently operating heavy-ion accelerators, is right now vigorously debated, there are hardly ny doubts that we will have a reliable evidence of the plasma within a few years.

1.5.1   Signatures of Quark Gluon Plasma

In the last few years researchers at Brookhaven and CERN have succeeded to measure a wide spectrum of observables with heavy ion beams, Au+Au and Pb+Pb. While these programs continue to measure with greater precision the beam energy, nuclear size, and centrality dependence of those observables, it is important to recognize the major milestones passed thus far in that work. The experiments have conclusively demonstrated.

- stopping and directed collective transverse and longitudinal flow of baryons and mesons in and out of the impact plane, both at AGS and SPS energies,

- hadronic resonance production,

- strangeness enhancement,

- the existence of strong nuclear A dependence of, among others, J/Ψ and Ψ meson production and suppression.

- dilepton-enhancement below and above the r meson mass, and

These observations support that a novel form of "resonance matter" at high energy and baryon density has been created in nuclear collisions.

1. <u>Direct Photons</u>

Photons are produced in a QGP in annihilation processes

$$q + \overline{q} \longrightarrow \gamma + g \qquad (1.2)$$

or Compton like processes

$$g + q(q) \longrightarrow \gamma + q(\overline{q}) \qquad (1.3)$$

It has been shown theoretically [20] that the momentum distribution of the γ photons emitted in these processes is strongly related to the corresponding distribution of the quarks and gluons from the plasma. Hence, the temperature of these photons is a good indicator of the QGP temperature.

During the time when the matter is in the quark-gluon plasma phase, it will emit particles. Photons arising from the electromagnetic interactions of the constituents of the plasma will provide information on the properties of the plasma

at the time of their emission. Since photons are hardly absorbed by the medium, they form a relatively 'clean' probe to study the state of the quark-gluon plasma. The presence of these photons in high-energy heavy-ion collisions can also possibly provide evidence for the production of the quark-gluon plasma [21, 22, 23].

2. Dilepton Production

Dileptons can be produced in QGP through the annihilation process

$$q + \overline{q} \longrightarrow \gamma^* \longrightarrow l^+ l^- \tag{1.4}$$

The invariant mass of the lepton pair carries information about the quark distributions [24] meaning that, as in the photon case, these can be used to measure thermal properties of the plasma. The other sources which produce dileptons are annihilation processes with quarks from the initial nuclei, hadronic scatterings like

$$\pi^+ + \pi^- \longrightarrow l^+ l^- \tag{1.5}$$

or decay of particles like $\pi^0, \eta, \omega, \phi, J/\Psi, \Psi$. At high invariant masses there is also a large background from correlated heavy quark decays. All these must be taken into account in order to see the net effect of the QGP.

Lepton pairs from hadronic sources in the invariant mass range between 0.5 and 1 GeV are important signals of the dense hadronic matter formed in nuclear collisions [25, 26]. They provide exclusive information about possible medium modifications of hadronic properties, especially of the ρ-meson, at high density [27, 28]. Another strategy for using the leptonic ρ-meson decay as a probe of the hadronic phase of the fireball is based on the idea that the ρ-peak is expected to grow strongly relative to the ω peak in the lepton pair mass spectrum, if the fireball lives substantially longer than 2 fm/c. Because of the short averagem lifetime of the ρ-meson, the ρ/ω ratio can therefore serve as a fast clock for the fireball lifetime [29].

3. J/Ψ suppression

The suppression of J/Ψ production [30] in a quark-gluon plasma occurs because a $c\overline{c}$ pair formed by fusion of two gluons from the colliding nuclei cannot bind inside the quark-gluon plasma [31].J/Ψ particles are bound states of a c quark and a $\overline{c}$ anti-quark. Since the charm quarks are heavy, they are likely to be produced in the initial moments of a collision mainly from hard parton scatterings. In p+p or p+A collisions, the created J/Ψ's would simply escape the collision region and be

detected through their decay channels. In nucleus-nucleus collisions however, the J/Ψ mesons need to pass through the extended hot and dense nuclear medium.

The J/Ψ meson is a tightly bound particle but in a quark-gluon plasma environment the charm quarks are screened pretty much like in the analogous phenomen called Debye screening from QED. Moreover, in a QGP the quarks and gluons are free and the string tension vanishes. In consequence, the interaction between the c and $\bar{c}$ quarks is weakened to a point in which the J/Ψ meson can dissociate leading to a suppression of the J/Ψ yield compared to p+p or p+nucleus collisions [27]. The free charm and anti-charm quarks travel through the plasma until the system cools down and they can hadronize by combining with the more abundant u, d and s quarks and forming open charm particles like D(c$\bar{u}$ or c $\bar{d}$), $\overline{D}$(c $\bar{u}$ or c $\bar{d}$), Ds(c $\bar{s}$) and D $\bar{s}$(c $\bar{s}$). If the density of charm quarks formed is high enough they can also recombine into J/Ψ or excited states like Ψ, and x_C, thus complicating the signal.

4. Strangeness enhancement

Strangeness enhancement refers to the increased production of strange particles in nuclear collisions due to the opening of new production channels in quark-gluon plasma. This signal was first predicted in [32] and explained through interactions between partons in the dense and hot QGP. At low energy, strange particles are produced mainly in hadronic channels but in a QGP environment processes like quark anti-quark annihilation and gluon fusion produce an excess of strange quark pairs. It is expected that for a high enough temperature, T $\geq$ 160 MeV, the strangeness abundance saturates in the plasma in a very short time $\sim 10^{-23}$ sec and will lead to an enhanced production of strange and multi-strange particles. This enhancement was observed at the top SPS energy for strange hyperons like Λ, Ξ, Ω in nucleus nucleus collisions compared to small interacting systems like proton-nucleus collisions. Moreover, in nucleus-nucleus collisions, the enhancement grows with the number of wounded nucleons (or reaction centrality) but also with the number of component strange quarks. This is consistent with the QGP creation hypothesis.

1.6   QCD Phase diagram and QCD critical point

1.6.1   QCD Phase diagram

Many of the various facets of normal nuclear matter are also expected to appear in the strongly regime. Some of the states of nuclear matter are illustrated in fig 1.1.

At a very high temperatures or baryonic densities, a phase transition from hadronic matter to quark-gluon matter is predicted to take place: quarks and gluons are confined into hadrons ("deconfinement") forming a new state of matter: the Quark Gluon Plasma (QGP). To create this deconfinement partonic matter, one needs to increase the energy density of the nuclear system above a certain critical energy density (ε_C) where the average distance between quarks becomes sufficiently small (asymptotic freedom) so that confinement disappears. There are two possible ways to achieve this: either by compressing cold nuclear matter or by heating the matter at zero net baryon density. The heating process consists in increasing the temperature of the system, which can be achieved at high energies. In the compressing mode, one tries to increase, in a given volume, the baryon number density. It is therefore possible to map out the nuclear phase diagram in the (T,μ_B) plane by compressing or heating or by combinations of both.

The exploration of this phase diagram is not only important for the understanding of QCD, but it has also strong implications in cosmology and for astrophysical compact objects. The matter at zero net baryon density and high temperatures is believed to have existed in the early universe a few microseconds after the Big Bang. At zero temperature and high net baryon densities, one expects a deconfined high density phase predicted to exist in the interior of neutron stars.

It is hoped that the experimental study of the nuclear matter phase diagram, in particular the study of phase transitions, the deconfined matter, as well as the existence and the location of the critical end point, will provide answers to some of the most fundamental open questions of modern high energy physics:

- What are the properties of strong interaction?
- Why are quarks not observed as free particles?
- How do hadrons acquire their mass?
- What are the properties of hadrons in dense baryonic matter?

Experimentally, one needs to vary the temperature and/or the net baryonic

density in order to create hot and dense matter. In high energy heavy ion collision, such conditions an be reached, as the energy lost by the colliding nuclei is deposited in the vicinity of centre of mass. This makes heavy ion collisions an excellent tool to probe the phase diagram.

1.6.2 QCD Critical Point

It is long standing open question, whether a critical point exist on the QCD phase diagram and how to predict hypercritically its location. Since the phase transition at zero μ_B is not a thermodynamic singularity but a rapid crossover from the region dominated by a gas of hadrons to the one dominated by quark and gluon degrees of freedom [33]. This basic picture has been built up by finite temperature lattice calculation. On the other hand, the transition at (T = 0, $\mu_B > 0$) region is thought to be first order phase transition. This conclusion is less robust, since the first principle lattice calculation are not controllable in this region due to serious fermion sign problem. But the results from different models indicate that the transition at this region should be first order phase transition. Thus, people argue that their
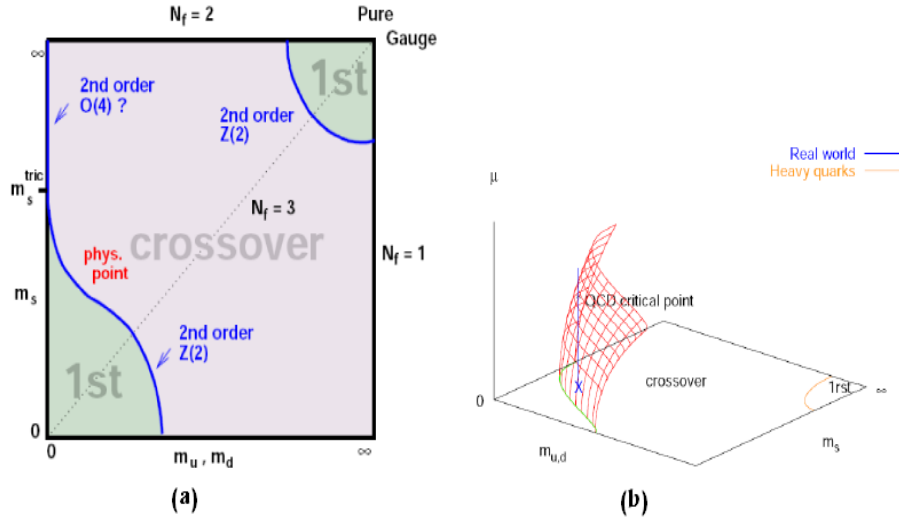
Figure 1.9: *(a) Schematic phase transition behaviour of $N_f = 2 + 1$ flavour QCD as a function of quark masses ($m_{u,d}, m_s$) at $\mu = 0$ [50]. (b) ($m_{u,d}, m_s$) first order phase transition line evolution with the chemical potential [36].*

must be a critical point somewhere in the midst of the QCD phase diagram as the end point of the first order line [34].

It is generally agreed that a phase transition line separating bound hadronic matter from deconfined matter which starts from (T $\sim 0, \mu_B > m_N$) and meets the zero μ_B axis at a critical temperature T_C in the range 170-190 MeV (see figure 1.1). Lattice QCD calculations [35] show that at $\mu = 0$, the order of the phase transition depends on the light and strange quark masses as shown in fig 1.9 (a). At small and very high u, d and s masses the phase transition is of the first order while at intermediate masses the transition is continuous (higher order). All existing lattices calculations at zero chemical potential suggest a continuous transition (the physical point is marked on the figure). Recent studies with non-vanishing chemical potential [36] suggest that the $(m_{u,d}, m_s)$ phase transition line moves towards higher quark masses and at some critical μ_C it reaches the physical quark masses point (see fig 1.9 (b)). For $\mu > \mu_C$, the physical point for quark masses falls inside the first order phase transition region. This would determine the existence of a critical
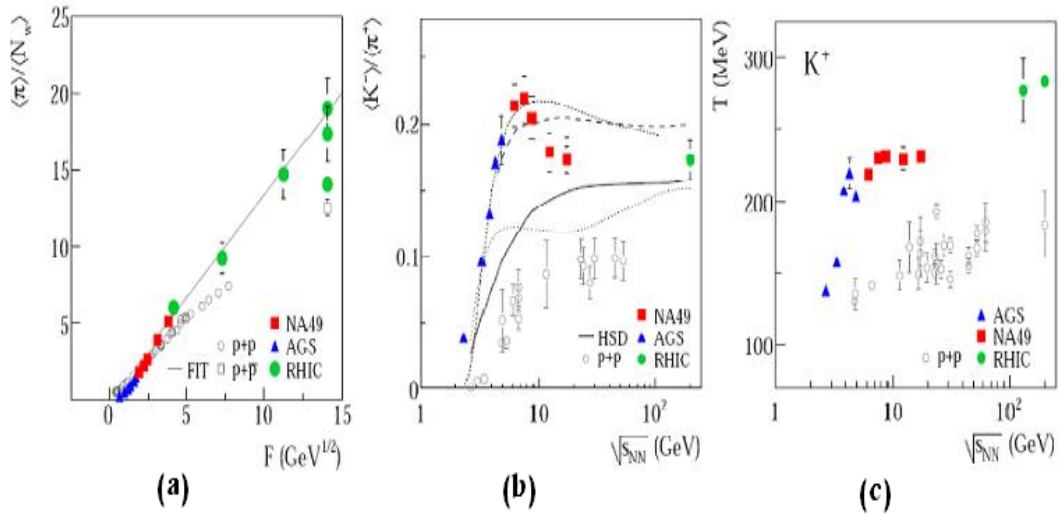
Figure 1.10: *(a) Energy dependence of the mean pion multiplicity per wounded nucleon (the kink). (b) Energy dependence of the $< K^+ > / < \pi^+ >$ ratio (the horn). (c) Energy dependence of the inverse slope parameter T for K^+ spectra (the step) [39].*

point (T_C, μ_C) which separates a first order phase transition region at $\mu > \mu_C$ and a smooth cross-over region at $\mu < \mu_C$.

The exact location of the critical point is not yet known but it has been speculated that it lies in the phase space reachable at lower SPS energies ($5 < \sqrt{S_{NN}} < 8 GeV$). Lattice QCD calculations suggest that the critical chemical potential μ_C might be approximately $\mu_C = 360$ MeV [37] or $\mu_C = 470$ MeV [38] which might be reachable at the above mentioned energies. Fig 1.10 suggest discontinuities in the excitation functions of hadronic observables measured in nucleus-nucleus collisions compared to the nucleon-nucleon collisions [39]. The 4π pion yield normalized to the number of participant (wounded) nucleons, proportional to the entropy production, is at AGS energies lower for A + A collisions than for N + N collisions. The slope in the energy dependence is however steeper for A + A collisions so that a $\sqrt{S_{NN}} \sim 7$ GeV the $< \pi > / < N_W >$ ratio becomes higher than the one for N + N collisions. The excitation function of the $< K^+ > / < \pi^+ >$ ratio,
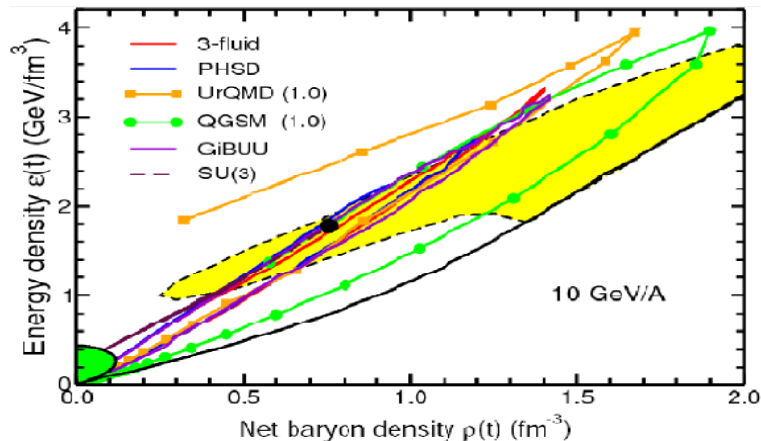
Figure 1.11: *Phase trajectories $(\rho_B(t), \varepsilon(t))$ at the centre of head-on Au+Au collisions at $\sqrt{S_{NN}} = 4.7 GeV$ from several dynamical models. The hadronic freeze-out is indicated at the lower left of the figure while the dashed contour denotes the phase coexistence region [40]. The markers in the figure represent time steps in the collision evolution starting with 1 fm/c and continuing up to 12 fm/c with 1 fm/c time intervals [41].*

and also the strangeness ratio E_S show a steep increase with a sharp maximum at

$\sqrt{S_{NN}} \sim 7 GeV$ followed by a decrease and a flattening behaviour toward RHIC energies. The inverse slopes of kaons show a sharp increase at AGS energies, then a flat region at SPS followed by another increase in temperature at RHIC energies. This behaviour resembles the behaviour of intensive thermodynamical quantities at a phase transition in a macroscopic system.

Although evidence of the collision energy range where the critical point might be accessible exist, its exact location in the phase diagram is still unclear from both a theoretical and experimental point of view. The search for the critical point is limited experimentally due to the fixed dynamical phase trajectories available in heavy ion collisions. An attempt to find the optimum collision energy where the decomposed nuclear matter spends maximum time in the phase coexistence region has been carried out in [40] by using a large variety of theoretical models. It was found that despite of the very different theoretical approaches the models are in good agreement on the energy and baryonic densities reached during nuclear collisions (see figure 1.11). The main conclusion was that the optimal conditions for exploring the hadronization phase transition and the critical point lies in the energy range $3.6 < \sqrt{S_{NN}} < 6.4 GeV$.

Chapter 2

FAIR and its experiments

2.1 Introduction

The Facility for Antiproton and Ion Research, FAIR, is a new particle accelerator facility to be build at the GSI site in Germany. The research at FAIR will cover a wide range of topics in nuclear and hadron physics, high density plasma and atomic physics, and applications in condensed matter physics and biology. A 1.1 km circumference double ring of rapidity cycling 100 and 300Tm synchrotrons, will be FAIR's central accelerator system. It will be used to produce, inter alia, high intensity secondary beams of antiprotons and short-lived radio active nuclei. A subsequent suit of cooler and storage rings will deliver heavy ion and antiproton beams of unprecedented quality.

The main focus of FAIR research is on the structure and evolution of matter on both a microscopic and on a cosmic scale deepening our understanding of fundamental questions like:

• How does the complex structure of matter at all levels arise from the basic constituents and the fundamental interactions?

• How can the structure of hadronic matter be deduced from the strong interaction? In particular, what is the origin of hadron masses?

• What is the structure of matter under the extreme conditions of temperature and density found in astrophysical objects?

• What were the evolution and the composition of matter in the early Universe?
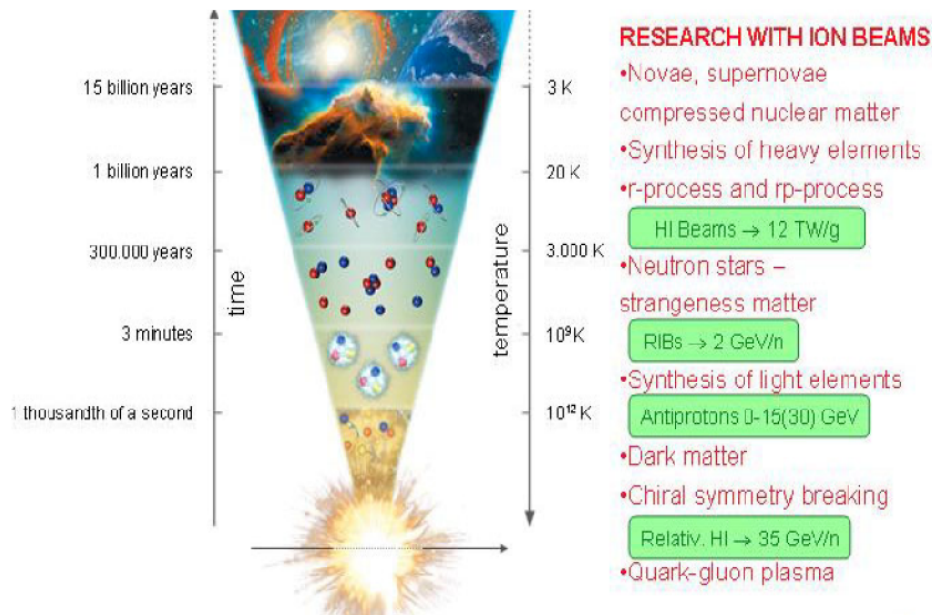
Figure 2.1: *Schematic illustration of the potential interconnections between the evolutionary phases of the universe and the research areas to be pursued at the FAIR facility with beams of ions and antiprotons.*

- What is the origin of the elements in the Universe?

FAIR will provide the scientific community with a world wide unique and technically innovative particle accelerator system to perform cutting edge research in the sciences concerned with the basic structure of matter [42, 43, 44]. The facility will provide an extensive range of beams from protons and anti protons to ions upto uranium with world record intensities and excellent beam quality in the longitudinal as well as transverse phase space. The scientific goals pursued at FAIR are described in fig 2.1 include:

- Studies with beams of short-lived radioactive nuclei, aimed at revealing the properties of exotic nuclei, understanding the nuclear properties that determine what happens in explosive processes in stars and how the elements are created, and testing fundamental symmetries.

- The study of hadronic matter at the sub-nuclear level with beams of antiprotons, in particular of the following key aspects: the confinement of quarks in hadrons, the generation of hadron masses by spontaneous breaking of chiral sym-

metry, the orgin of the spins of nucleons, and the search for exotic hadrons such as charmed hybrid mesons and glueballs.

- The study of compressed, dense hadronic matter through nucleus-nucleus collisions at high energies.

- The study of bulk matter in the high density plasma state, a state of matter of interest for inertial confinement fusion and for various astrophysical sites.

- Studies of quantum electrodynamics (QED), of extremely strong electromagnetic field effects and ion-matter interactions.

- Hadron structure and the nature of the strong force in the non perturbation regime of QCD with high energy beams of antiprotons.

- The QCD phase diagram and the quark gluon plasma in nucleus nucleus collisions.

2.2   Overview of the FAIR Facility

Figure 2.2 shows a schematic view of the facility. The central part of the FAIR facility consists of the SIS 100 and SIS 300 accelerators, two up to 4T/s rapidly cycling synchrotrons along a perimeter of 1100m and with maximum magnetic rigidities of 100 and 300 Tm, respectively. Heavy ion (HI) beams will be injected from the existing GSI UNILAC and SIS 18 accelerators, high intensity proton beams, as needed for antiproton production from a new linear accelerator in front of the SIS 18. Both HI and proton beams will be compressed to very short bunch lengths for the production of exotic nuclei (60ns)or anti protons (25ns)

The primary goals of FAIR are substantial increases in ion beam intensity over the present facility for both primary (factor 100 to 1000) and secondary (factors upto 10000) heavy ion beams and the generation of intense anti proton beams. All beams will be available over a brand range of energies, essentially from thermal to highly relativistic velocities (several tens of GeV/u for ions and 15 GeV/c for antiprotons).

A major goal is the preparation of high-quality ion and antiproton beams via beam cooling in storage rings. This is particularly useful for secondary beams produced in nuclear reactions with, necessarily, broad momentum distributions. The storage/cooler rings also serve as experimental systems of high-resolution in

internal-target experiments.
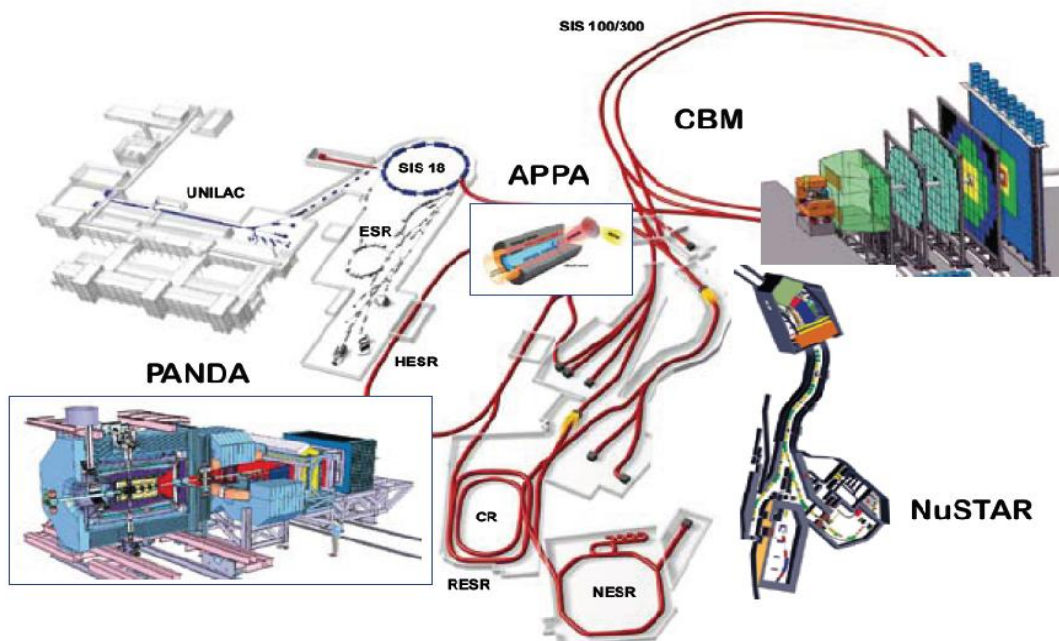
Figure 2.2: *The FAIR accelerator/storage ring complex and the large experiments APPA, CBM, NuSTAR (including the Super-FRS) and PANDA (at the antiproton accelerator/storage ring HESR). GSIs UNILAC and SIS18 will serve as injectors into the SIS100/300 synchrotrons. Antiprotons or radioactive isotopes will be collected in CR, accumulated in RESR and accelerated or decelerated and stored in HESR and NESR.*

The accelerators will be complemented by a number of cooler and storage rings run in parallel operation:

• The Collector Ring (CR) for stochstic cooling of antiproton or radioactive ion beams. In addition, this ring offers the possibility of measuring the masses of short-lived nuclei by operating it in isochronous mode.

• The Accumulator Ring (RESR) for the accumulation of antiprotons and for the fast deceleration of short-lived nuclei.

• The new Experimental Storage Ring (NESR) for various experiments with ion or antiprotons beams. Equipped with stochastic and electron cooling devices it will house a variety of experimental devices including a precision mass spec-

trometer, internal target set-ups for experiments with atoms and electrons and an electron nucleus collider. The NESR will be capable of further decelerating ions and antiprotons and extracting them for use in the antimatter FLAIR experiments.

• The 50 Tm High Energy Storage Ring (HESR) is optimised for acceleration and storage of antiprotons of energies upto 14GeV. The ring will operate with an internal target and associated detector set-up (PANDA Experiment). It will be equipped with a stochastic cooling system and a 5 MV electron cooler to compensate for beam degradation due to target interaction and intra-beam scattering.

The physics program at FAIR addresses three main areas of research: Nuclear and Astrophysics with radio active beams (NUSTAR Collaboration), strong QCD physics with (polarised) antiprotons (PANDA Collaboration) and high-energy HI beams (CBM Collaboration).

2.2.1   Experiments at SIS 100

Heavy-ion beams in the energy range between 2 and about 14A GeV are ideally suited to explore the properties of dense baryonic matter. According to transport calculations, energy densities up to 2.5 GeV fm^3 and baryon densities of 2 - 7 times saturation density ρ_0 are expected to be reached in the center of the reaction zone. Such conditions prevail in core collapse supernovae and in the core of neutron stars. Measurements at SIS 100 energies will focus on the investigation of the properties of resonance matter in the vicinity of the phase boundary, and, therefore, will provide important information on this transition region of the QCD phase diagram. The following fundamental questions can be addressed experimentally with heavy-ion collisions at SIS 100:

• What is the electromagnetic structure of dense baryonic matter?

• What are the properties of hadrons in dense baryonic matter?

• Is chiral symmetry restored at very high baryon densities?

• What is the equation-of-state of nuclear matter at neutron star core densities?

• What are the relevant degrees-of-freedom in the vicinity of the deconfinement phase transition?

• Does strange matter exist in the form of heavy multi-strange objects?

• How is charm produced at threshold beam energies?

• How does charm propagate in nuclear matter?

The heavy-ion experiments at SIS 100 will concentrate on the measurement of the following observables:

The production of multi-strange hyperons at threshold beam energies proceeds via strangeness exchange reactions in multistep processes. The "cooking" of Ξ and Ω hyperons is favored at high densities where the mean free path between consecutive collisions is short. Therefore, the yield of multi-strange hyperons depends very much on the density, and, hence, on the compressibility of baryonic matter at these particular densities. In conclusion, a detailed measurement of the excitation function of the multiplicities and the collective flow of multi-strange hyperons in heavy-ion collisions at beam energies between 2 and 11A GeV will provide new information on the equation-of-state of nuclear matter at high densities. No multi-strange particles have been measured in heavy-ion collisions in this energy range (except for a Ξ data point at 6A GeV).

According to model calculations, the yield of meta-stable exotic multi-hyper-nuclear clusters (consisting of nucleons and hyperons) increases with increasing baryon density, and has a maximum in heavy-ion collisions at FAIR energies. Therefore, the search for composite objects with multiple units of strangeness is very promising at SIS 100. These objects can be identified, e.g. via their weak decay into a pair of lambda hyperons.

2.2.2   Experiments at SIS 300

The heavy-ion beams from SIS 300 are required for the CBM core research program which is the search for the most prominent landmarks of the QCD phase diagram at high net baryon densities: the first order deconfinement phase transition and the critical endpoint. Moreover, the research program at SIS 300 includes the study of the equation-of-state of high-density baryonic matter, and the search for modifications of hadronic properties in the dense baryonic medium as signatures for chiral symmetry restoration.

As pointed out in the previous chapters, the most promising observables from nucleus-nucleus collisions in the SIS300 energy range are:

• particles containing charm quarks (D mesons and charmonium): heavy quarks are created in the early phase of the collision and, hence, probe the highly compressed baryonic matter.

• low-mass vector mesons decaying into dilepton pairs (ρ, ω and ϕ mesons): electron and muon pairs are penetrating probes which carry undisturbed information on hadron properties in the dense and hot fireball.

• the collective flow of identified hadrons: the flow is driven by the pressure created in the early phase of the collision and carries information on the equation-of-state of dense matter.

• kaons, hyperons (Λ, Ξ, Ω and their antiparticles) and hadronic resonances (as ϕ, K^*, Λ^*): the yield of particles carrying strange quarks is expected to be sensitive to the fireball evolution.

• dynamical fluctuations of particle multiplicities and momenta: event-wise fluctuations are expected to occur if the system passes a first order phase transition or the critical endpoint.

• photons: photons are penetrating probes and can provide information on direct radiation from the early fireball

• two-particle correlations: two-particle correlations carry information on the source size and time evolution of the fireball and particle production

Phase transitions occur above a critical energy density and can only be observed if the matter extends over a certain volume. Therefore, a key feature of the CBM experimental program is a systematic and comprehensive measurement of excitation functions and system size dependencies of all observables.

Particular emphasis will be put on rare diagnostic probes which are not accessible by other experiments in this energy range. The identification of rare probes requires high beam intensities, a large duty cycle, excellent beam quality, and running times of several months per year. Observables like event-by- event fluctuations require full azimuthal coverage of the produced particles in a wide acceptance of rapidity and transverse momentum and excellent centrality determination.

2.3 NUSTAR Experiment

Research in natural sciences has provided us with an increasingly detailed picture of the structure of matter. This search is ongoing and we continue to analyse the elementary building blocks of matter and the fundamental forces acting between them on an increasingly deeper level. Particle accelerators have and will continue

to play a key role in those aspects. Next-generation facilities will allow us an even deeper probing into the structure of matter and the structure of Universe.

One of the scientific pillars of the forthcoming FAIR Facility [45] is the program centred around the unprecedented range of exotic, radioactive beams, with several orders of magnitude higher intensities than currently available that will be delivered from the planned super-FRS fragment separator [46, 47]. This program is governed by the NUSTAR (Nuclear Structure, Astrophysics and Reactions) Collaboration.

The new Facility for Antiproton and Ion Research (FAIR) at Darmstadt will offer completely new possibilities for the exploration of phases and structures created by the strong interaction. In order to investigate the full structure of the nuclear many-body problem the Nuclear structure, Astrophysics and Reaction (NUSTAR) collaboration was formed. The NUSTAR collaboration contains both experimental and theoretical programs that will provide the ideal interplay needed to tackle the exciting and challenging questions of the NUSTAR physics program.

The NUSTAR Facility at FAIR aims at the investigation of Nuclear Structure,nuclear Astrophysics,and Reactions. The goal is the understanding of structure and dynamics of nuclei for away from stability in order to make major contributions towards answering fundamental questions such as:

• What are the limits of existence of nuclei?

• What is the isospin dependence of the effective nucleon-nucleon interaction and of the equation of state of nuclear matter?

• How are the heavy elements produced in the universe?

To investigate these questions, the NUSTAR Collaboration will produce exotic nuclei and investigate them with dedicated complementary setups each of them specialized for particular observables.

2.3.1 Observables

The NUSTAR Collaboration will study nuclei at the limits of their existence [48]. The central facility of NUSTAR is the Super Fragment Separator, which will analyse very short lived radioactive nuclei at intensities as shown in fig 2.3. As one moves away from stability from the neutron-rich side one approaches a region where the proton/neutron ratio is drastically different from that in stable nuclei. Here, the isospin dependence of nuclear structure phenomena can be studied and weaker

binding is expected to bring about extended surface zones of neutron-enriched, low density matter. The study of these neutron skins or halos determines the effective interactions in such nuclear environments and thus will help to investigate the equation-of-state of cold neutron matter between saturation and low density. Investigations of the most neutron-rich isotopes also offer direct access to part of
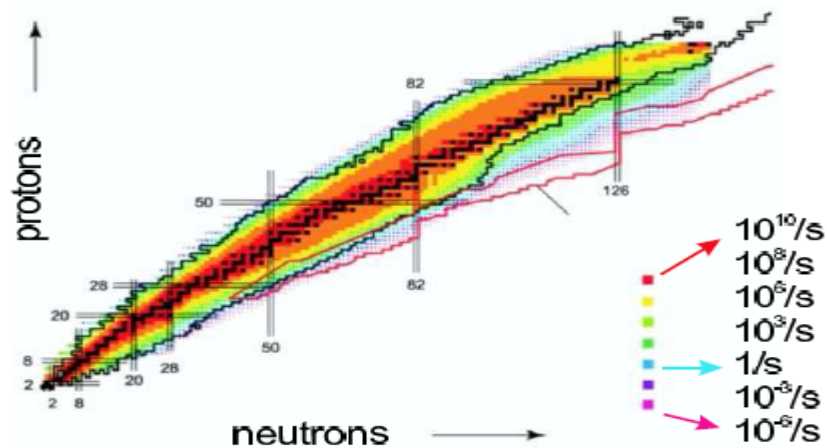
Figure 2.3: *Production rates of radio active nuclei at the Super-FRS. The r-process in supernovae explosions is believed to proceed within the zone outlined in red on the right hand side of the figure.*

the astrophysical r-process path, leading to a fruitful synergy of nuclear structure and nuclear astrophysics. The location of the nucleon drip-lines is determined by a whole range of effects; the Coulomb force, changing shell structure, nucleon-nucleon correlations and proton-neutron asymmetry, amongst other things. The proton drip-line lies quit close to stability because of the effects of the coulomb force. The beams from FAIR will allow us to produce nuclei at the proton drip-line in abundance and allow us to study them in detail. More interestingly, the neutron drip-line is thought to lie a long way from stability in the heavy elements because there is no coulomb repulsion between neutrons. It is known only for light elements up to oxygen ($Z = 8$) and it will be very difficult to reach beyond $Z = 25$.

2.3.2   Experimental Set-Up

The Nuclear Structure and Astrophysics (NUSTAR) Collaboration, which comprises a vast number of experiments to be performed using radioactive beams from stopped up to relativistic energies. At the high-energy branch, the R^3B concept builds upon an ion-by-ion identification and momentum analysis with maximum precision of the incoming outgoing ions, in addition to detection of all other reaction products (light ions, protons, neutrons and γ-rays). This permits precision experiments with the relativistic radio active species with beam characteristic as produced in-flight in the super-FRS and allows studies of the most exotic nuclei that the future facility will be able to produce.

R^3B **Reactions with Relativistic Radioactive Beams**

The high energy cave houses the reactions with relativistic radioactive beams (R^3B) set-up which provides unique opportunities for kinematically complete measurements of reactions of the most exotic nuclei with high resolution at relativistic energy (see fig 2.4). For decades, reaction experiments at relativistic energies have been proven extremely useful as a tool for nuclear structure investigations. Here a large range of reaction types are accessible and the intrinsic structure can normally be readily disentangled from thr reaction mechanism. Furthermore, the possibility of using thick secondary targets and large, efficient coverage of a wide variety of detector types makes such experiments matches the scarce, most exotic nuclear species excellently.

The R^3B collaboration has designed an experimental set-up capable of fully benefiting from the Super-FRS beams (0.32 GeV/u) with the characteristics inherent to the in-flight production method. Located at the focal plane of the high-energy branch of the Super-FRS, R^3B is a versatile fixed-target set-up with high efficiency, acceptance and resolution for kinematically complete measurements of reactions with high-energy radio active beams. The heart of the R^3B set-up is a large-acceptance superconducting dipole magnet, permitting identification and momentum analysis of the reaction products with a coverage approaching 4π due to the forward-directed Lorenz boost(see fig 2.4.) Here, the R^3B programme will focus on the most exotic short-lived nuclei, which cannot be stored and cooled efficiently, and on reactions with large-momentum transfer allowing the use of thick targets. The proposed experimental setup is adapted to the highest beam energies
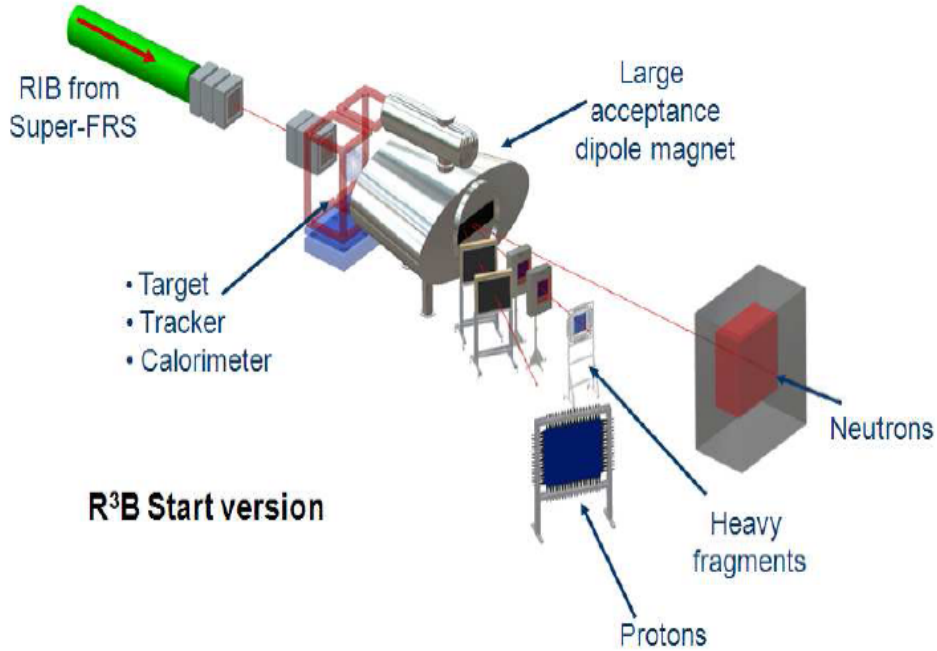
Figure 2.4: *Schematic drawing of the R3B experimental set-up comprising γ-ray and target recoil detection, a large-acceptance dipole magnet, a high-resolution magnetic spectrometer, neutron and light-charged particle detectors and a variety of heavy-ion detectors.*

delivered by the Super-FRS, thus exploiting fully the highest possible transmission efficiency of secondary beams. The most essential upgrades concern the target recoil detector and the two magnetic spectrometers. A schematic view of the R3B experimental setup is shown in Fig 2.4. The incoming secondary beams are tracked and identified on an event-by-event basis. Measurements of the magnetic rigidity B_ρ (position measurement at the dispersive focus in the Super-FRS), time-of flight ToF, and energy loss ΔE provide unique isotope identification and momentum determination. Although the secondary beam has a momentum spread of $\pm 2.5\%$, the momentum will be determined to an accuracy of 10^{-4} (event-wise). After the secondary target, the kinematically forward focused projectile residues are again identified and momentum analyzed.

Two modes of operation are foreseen depending on the demands of the experiments: i) A large-acceptance mode: Heavy fragments and light charged particles

(i.e. protons) are deflected by a large-acceptance dipole and detected with full solid-angle acceptance, for most reactions envisaged. Resolutions for velocity and B_ρ measurements amount to about 10^{-3} allowing unique identification in mass and nuclear charge of also heavy fragments. ii) A high-resolution mode: here, the dipole magnet is operated in reversed mode, deflecting the fragments into a magnetic spectrometer. The envisaged resolution of 10^{-4} will allow, e.g., a precise measurement of the fragment recoil momentum in single-nucleon knock-out and quasi-free scattering experiments even for heavy nuclei.

2.4 PANDA Experiment

There are many fundamental questions which remain basically unanswered. Phenomena such as the confinement of quarks, the existence of glueballs and hybrids, the origin of the masses of hadrons in the context of the breaking of chiral symmetry are long-standing puzzles and represent the intellectual challenge in our attempt to understand the nature of the strong interaction and of hadronic matter.

The FAIR facility (Facility for Antiproton and Ion Research), which will be built as a major upgrade of the existing GSI laboratory in Germany, will provide antiproton beams of the highest quality in terms of intensity and resolution, which will provide an excellent tool to answer these fundamental questions. One of the attractions of the FAIR Facility is the provision of cooled antiproton beams of unprecedented intensity and quality,stored in the High Energy Storage Ring (HESR). The HESR will deliver 10^{11} stored and stochastically or electron cooled antiprotons at luminosities up to 2.10^{32}. Its energy resolution will lie between 10^{-5} and 10^{-4} at energies between 3 and 14 GeV. Antiproton annihilation in this energy regime will produce strange and charmed quarks in addition to large amounts of gluons.

The PANDA experiment (Pbar ANnihilations at DArmstadt) will use the antiproton beam from the High-Energy Storage Ring (HESR) colliding with an internal proton target and a general purpose spectrometer to carry out a rich and diversified hadron physics program, which includes charmonium and open charm spectroscopy, the search for exotic hadrons and the study of in-medium modifications of hadron masses.

PANDA has been designed to achieve almost full 4π hermiticity. It is based

on two magnetic spectrometers that analyse the momentum of the emitted charged particles in a wide range from 100 MeV/c to 8 GeV/c. The superconducting target solenoid surrounds the interaction region and has a forward opening of 22^0 to allow high momentum particles enter the forward dipole spectrometer. Since many hadron decay channels include charmed mesons, a micro vertex detector with excellent position resolution is required. Other important components of PANDA are the electromagnetic calorimeters with good energy resolution down to very low energies, and the hadron calorimeter. To separate kaons from protons and muons, particle identification using various time-of-flight and Cherenkov detector systems will be performed.

2.4.1 Physics Aspects of PANDA Experiment

The PANDA experiment has a rich experimental program whose ultimate aim is to improve our knowledge of the strong interaction and of hadron structure. The experiment is being designed to fully exploit the extraordinary physics potential arising from the availability of high-intensity, cooled antiproton beams. The main focus of the experiment are investigations related to the strong force at medium energy. The PANDA Collaboration has proposed to study fundamental questions of hadron and nuclear physics and to carry out precision tests of the strong interaction. This program includes the study of charmonium spectroscopy, the search for glueballs and hybrids in the charmonium mass region and the investigation of in-medium modifications of hadrons as they interact with nuclear matter.The PANDA physics program, also include the spectroscopy of single and double hypernuclei and the study of electromagnetic processes.

In order to gather all the necessary information from the antiproton-proton collisions a versatile detector will be build being able to provide precise trajectory reconstruction, energy and momentum measurements and an efficient particle identification system. The PANDA collaboration plans to build a state-of-the-art universal detector for strong interaction studies at the high-energy storage ring HESR at the international FAIR facility. The detector is designed to take advantage of the extraordinary physics potential, which will be available utilizing high intensity, phase space cooled antiproton beams.

Spectroscopy has been a prime tool for physics in the last century and has

played a leading role in the development of quantum mechanics and the standard model of physics. Quantum Chromo Dynamics (QCD) is generally accepted to be the correct underlying theory of the strong interaction. However, our knowledge of the behavior at large distances is still rather primitive. Spectroscopy experiments within hadron physics are the tool to investigate both in the dynamics governing the interaction of fundamental particles and the existence of new forms of matter. The latter could consist of gluonic degrees of freedom, like glueballs and hybrids, previously undiscovered charmonium states, the extension of the nuclear chart into the strangeness dimension, or particles produced inside nuclear matter. Only when we can predict, confirm, and explain the physical states of the theory, we can hardly claim that we understand the strong interaction. Such a deep understanding might have farther- reaching implications in particle physics. For example, it is quite possible that the weak interactions becomes strong at high energies and field theories of the strong interaction may be relevant to the mechanism of the electroweak symmetry breaking. In strong-interaction studies based on QCD we have the ideal laboratory to test our understanding of theory against experimental results.

2.4.2 Detector Design

The design of PANDA is based on previous experience in antiproton experiments and takes advantage of ongoing detector developments performed at the high-energy laboratories for experiments. The general layout of PANDA is based on two magnetic spectrometers and is shown in Fig 2.5. The target spectrometer surrounds the interaction region and has a superconducting solenoid as momentum analyser. A forward opening of 5-10 (depending on the respective axis) allows high momentum tracks to enter the forward spectrometer with a large-gap dipole magnet. The superconducting solenoidal magnet has a length of 2.5 m, a diameter of 1.9 m and provides an axial field of 2 T. It has to accommodate a gap for pipes of the target device. The target spectrometer is then made up of the following components:

Micro Vertex Detector

The Micro-Vertex-Detector (MVD) is situated in the target spectrometer and is the closest detector part with respect to the primary interaction vertex. The MVD is a tracking device for charged particles and thus essential for a very precise determination of secondary decay vertices of short-lived particles such as hyperons or mesons

with charm or strangeness content. In the current MVD design four barrel layers and eight disks are foreseen. Being equipped with either fine granular silicon pixel detectors or double sided silicon strip detectors the envisaged spatial resolution for secondary vertices is about 100 μm.

Central Tracking Detector

The cylindrical central detector will be the key device for momentum measurement of charged particles. Currently there are two different options under discussion: a time projection chamber (TPC) or a straw tube tracking system (STT). Although the concept of track reconstruction will be rather different both options will be able to fulfil the requirement of providing a momentum resolution Δp/p of about 1-2%. In addition both devices will contribute to particle identification via a dE/dx measurement.

Gas Electron Multiplier Stations

A set of large area planar Gaseous Electron Multipliers (GEM) detectors forms a GEM-Tracker, which will be used as a first forward tracking detector after the central tracker. Located in the middle of each GEM-Disc is a double-sided readout pad plane which allows particle track position measurement in four projections. The high number of projections per GEM-Disc allows unambiguous determination of the particle trajectory position with a resolution of better than 100 μm.

Forward Mini Draft Chamber System

The forward tracker (FT) is designed for momentum analysis of charged particles deflected in the field of the PANDA dipole magnet. The FT covers angular acceptance defined by the aperture of the magnet equal to $\pm 10^0$ horizontally and $\pm 10^0$ vertically with respect the beam direction. The FT consists of three pairs of planar tracking stations. With expected position resolution of σ=0.1 mm per detection layer and the material budget in one tracking station of 0.3%. X_0, the momentum resolution is better than 1%.

The PANDA detector is a hybrid detector designed to achieve 4π acceptance, high resolution for tracking, particle identification, calorimetry and high rate capabilities (2 x 10^7 annihilations/s). The detector (Figure 2.5) consists of two parts: a target spectrometer and a forward spectrometer. The target spectrometer surrounds the interaction region and is based on a superconducting solenoid magnet. The innermost sub-detector of the target spectrometer is a micro-vertex-detector
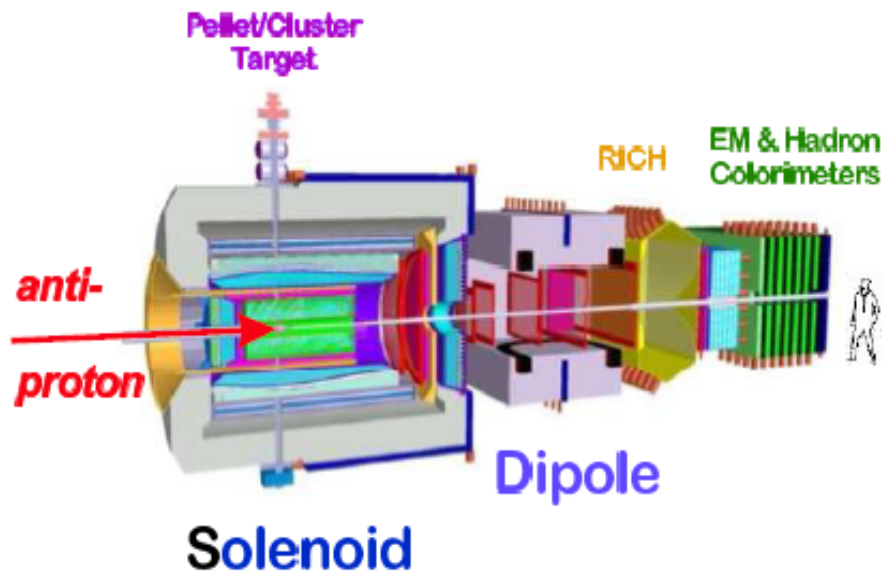
Figure 2.5: *The PANDA experiment. The antiproton beam enters from the left and hits the target one quarter into the superconducting solenoid. Particles emitted in the forward direction are momentum analysed in a dipole magnet. The setup is 12m long.*

for precise tracking information. It consists of several layers of silicon pixel detector and silicon strip detector. At larger distances from the interaction point the vertex tracking is done either by straw tubes (STT) or a high-rate time projection chamber (TPC) in the barrel part, and a set of multi-wire drift chambers (MDC) in the forward direction. For particle identification, a Cherenkov counter, detection of internally reflected Cherenkov light (DIRC) is foreseen. Following the Cherenkov detector, there will be a compact electromagnetic calorimeter made of $PbWO_4$ crystals with avalanche photodiode readout. The last layer of the target spectrometer is a muon detector which is located outside the solenoid magnet yoke. The forward spectrometer consists of a dipole magnet with a set of MDC for tracking, a RICH detector for particle identification, electromagnetic and hadronic calorimeters for charged and neutral particles, and muon counters for detection of muons. The target and forward spectrometers will provide high-resolution particle tracking, identification and momentum reconstruction for both charged as well as

neutral particles that will enable us to detect the complete spectrum of final states relevant to the PANDA physics objectives.

The High-Energy Storage Ring

The antiproton beam will be produced by a primary proton beam from the SIS100. The $\bar{p}$ production rate will be of approximately $2 \times 10^7/s$. After 5×105 $\bar{p}$ have been produced they will be transferred to the HESR, where internal experiments in the $\bar{p}$ momentum range from 1 GeV/c to 15 GeV/c can be performed
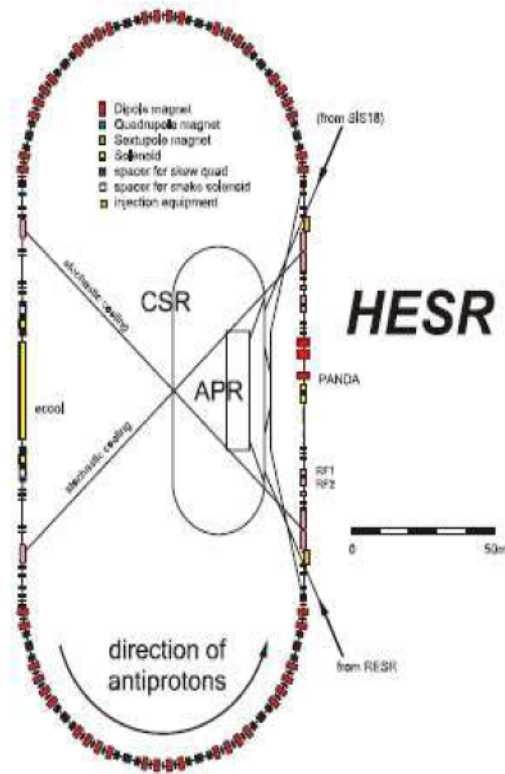
Figure 2.6: *Layout of the HESR.*

The layout of the HESR is shown in Fig 2.6. It is a racetrack ring, 574 meters in length, with two straight sections which will host the electron cooling and, respectively, the PANDA experiment. Two modes of operation are foreseen: in the high-luminosity mode peak luminosities of $2 \times 10^{32} cm^{-2}s^{-1}$ will be reached with a beam momentum spread $\delta p/p = 10^{-4}$, achieved by means of stochastic cooling; in the high-resolution mode for beam momenta below 8 GeV/c electron cooling will

yield a smaller beam momentum spread $\delta p/p = 10^{-5}$ at a reduced luminosity of $10^{31} cm^{-2} s^{-1}$. The high-resolution mode will allow to measure directly the total width of very narrow (below 1 MeV) resonances.

2.5   CBM Experiment

The FAIR Facility at GSI [49] will offer unique possibilities for the investigations of the QCD phase diagram at extreme net-baryon densities, besides serving a variety of other fields of physics with anti-proton beams for hadron physics, radioactive beams for nuclear structure physics, and highly pulsed ion beams for plasma physics. For the nuclear collision programme, a synchrotron with 300 Tm bending power (SIS 300) will deliver fully stripped external heavy-ion beams up to uranium with intensities of up to 2.10^9 per second at beam energies from 8 to 35 AGeV. Lighter ions (Z/A= 0.5) can be accelerated up to 45 AGeV, while proton beams will be available upto 90 GeV. The unprecedented beam intensities will allow studying extremely rare probes with high precision but also constitute a high challenge for detectors and electronics.

The CBM (Compressed Baryonic Matter) experiment [50] will be a next-generation fixed target detector to be operated at the FAIR heavy-ion synchrotron SIS-300. It is designed to measure hadronic, leptonic and photonic probes in a large acceptance and at the extreme interaction rates offered by the accelerator. CBM aims at a systematic investigation of A+A, p+A and p+p collisions, in terms of collision energy ($\sqrt{S_{NN}} = 4.5$ - 9.3 GeV for heavy nuclei) and system size, with high precision and statistics. In contrast to the low-energy programs at RHIC and SPS, which due to low collision rates will focus on bulk particle production,

The high μ_B region of the phase diagram can be explored by means of heavy ion collisions in the energy range of 10 - 40 AGeV, in which the chemical freeze-out line is depicted for Au-Au Collisions, as expected on the temperature and net baryonic density plane. The number refer to beam energies (in GeV per nucleon). The available energy at the RHIC collider (solid squares) is expressed as a sum of the energy of each beam i the laboratory (2+2 upto 100+100 AGeV). For FAIR, (energy range (10-45 AGeV)) the numbers refer to the kinetic energy of the incident beam on a stationary target. The highest baryonic densities at chemical freeze-out

are reached for incident energies between 20 and 40 AGeV corresponding to centre of mass energies per nucleon pair ($\sqrt{S_{NN}}$) in the range 6 - 10 GeV. For this reason, CBM is designed o operate in this energy range. In this region, CBM will search for the phase boundary between hadronic and partonic, the QCD critical point and for modification of hadron properties in dense matter serving as signature of the chiral symmetry restoration. The study of the equation of state of the nuclear matter at high baryon densities is also among the main goals of CBM.

The major challenge is to find diagnostic probes which are connected to the onset of chiral symmetry restoration, to the deconfinement phase transition, and to the equation of state of hadronic and partonic matter.

2.5.1   Chiral Symmetry Restoration

The in-medium spectral functions of short-lived vector mesons, which are expected to be sensitive to chiral symmetry restoration, can be studied in the dense nuclear medium via their decay into lepton pairs [51]. Since the leptons are affected very little by the passage through the high-density matter, they provide, as a penetrating probe, almost undistorted information on the conditions on the interior of the collision zone. Another observable sensitive to in-medium effects is open charm, e.g; D-mesons. The effective masses of D-mesons, a bound state of a heavy charm quark and a light quark, are expected to be modified in dense matter similarly to those of kaons. Such a change would be reflected in the relative abundance of charmonium ($c\bar{c}$) and D-mesons.

2.5.2   Deconfinement Phase Transition and The QCD Critical Endpoint

The onset of a first order phase transition is expected to cause a discontinuity in the excitation function of a particular observables. Such a non-monotonic behaviour has been observed around 30 AGeV in the kaon-to-pion ratio and in the inverse slope parameter of kaons [52]. A beam energy scan looking at a variety of observables is needed to clarify the experimental situation. This includes the measurement of the phase-space distributions of strange particles, in particular multistrange baryons (antibaryons), and particles containing charm quarks. For example, a disconti-

nuity in the excitation function of the J/Ψ to Ψ' ratio would indicate sequential charmonium dissociation due to color screening in the deconfined phase. Moreover, event-by-event fluctuations are expected to appear when crossing a first order phase transition and particularly in the vicinity of the critical endpoint. The identification of a critical point would provide direct evidence for the existence and the character of a deconfinement phase transition in strongly interacting matter.

2.5.3   The equation-of-state at high baryon densities

The formation of a mixed phase indicating the onset of deconfinement leads to a softening of the equation of state at a given beam energy [53]. The location of the so-called softest point may be discovered by measuring carefully the excitation function of the collective flow of particles.

Charm production plays a particular role at FAIR energies, because charmonium, D-mesons and charmed hyperons are created at beam energies close to the kinemitical threshold. Therefore, these particles are sensitive of probes of the early, high-density stage of the collision (more than ten times saturation density!). Collective effects contributing to charm production may be visible for the first time. Charm exchange processes may become important, reviling basic properties of charm propagation in a dense baryonic matter. The situation is analogous to strangeness production at SIS 18 energies, where 2-3 times saturation density is probed in Au-Au collisions. In order to perform high statistics measurements, the low cross sections for charm production at threshold beam energies have to be compensated by high beam intensities.

Chapter 3

The CBM Experiment

3.1 Introduction

At the future Facility for Antiproton and Ion Research in Darmstadt (FAIR) a dedicated heavy-ion experiment investigating the properties of highly compressed baryonic matter is proposed (CBM). The CBM Experiment will investigate heavy-ion collisions at beam energies from 8 to 45 AGeV at the future accelerator facility FAIR from 2015 on. The goal is to study the QCD phase diagram in the region of moderate temperatures and highest net-baryon densities in search of the first-order phase transition from confined to deconfined matter and the QCD Critical point. CBM will cover hadronic, leptonic and photonic observables at extreme interaction rates, thus having access to rarest probes like charm near threshold.Physics objectives, their experimental challenge, the resulting layout of the CBM detector, and first feasibility studies of key observables are discussed.

Besides secondary beams with rare isotopes and antiprotons the new accelerator will deliver primary beams of protons up to 90 GeV as well as heavy-ion beams from 2 to 35 AGeV for Uranium and up to 45 AGeV for nuclei with Z/A = 0.5. This energy range will allow the study of strongly interacting matter at the highest baryon densities which can be reached with heavy-ion collisions in the laboratory (fig 3.1). Within this energy range, the maximum of relative strangeness production in A + A interactions as well as the charm production threshold are located. Due to the extremely high design beam intensity of $10^9/s$, rare probes such as charm

production will be accessible experimentally. These features open up interesting physics objectives to be studied for the first time, e.g. the investigation of charm production in dense media.
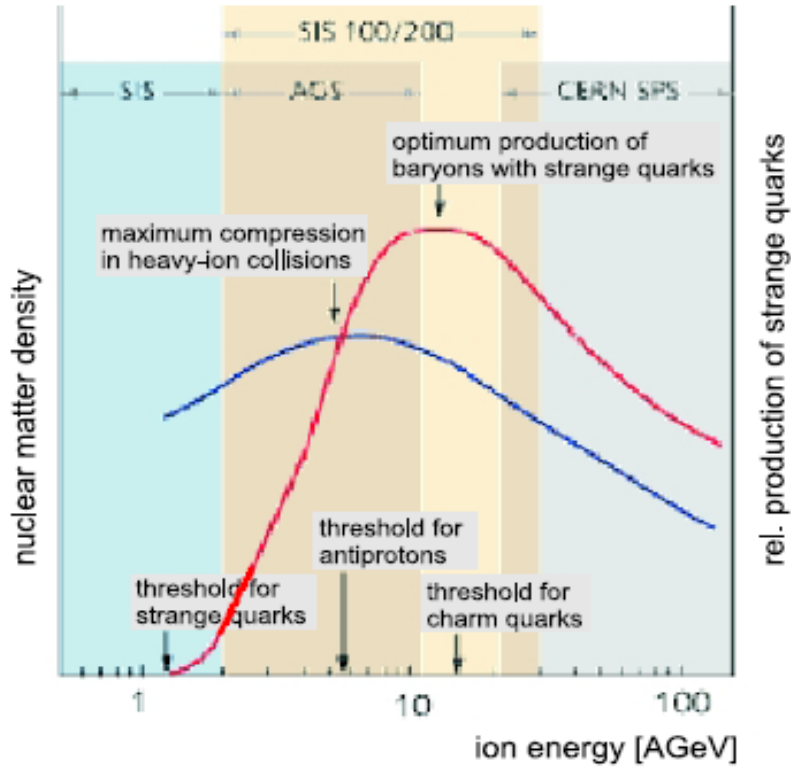
Figure 3.1: *Nuclear matter density and relative strangeness production in dependence on the incident beam energy. SIS 300 as it is currently planned at GSI will extend the energy range of the indicated SIS 100/200 up to 35 AGeV for heavy-ions and 45 AGeV for nuclei with Z/A = 0.5.*

The CBM (Compressed Baryonic Matter) experiment [54] will be a next-generation fixed-target detector to be operated at the FAIR heavy-ion synchrotron SIS-300. It is designed to measure hadronic, leptonic and photonic probes in large acceptance and at the extreme interaction rates offered by the accelerator. CBM aims at a systemtic investigation of A+A, P+A and P+P collisions, in terms of collision energy ($\sqrt{S_{NN}}$ = 4.5 - 9.3 GeV for heavy nuclei) and system size, with high precision and statistics. In contrast to the low-energy programmes at the RHIC and the SPS,

which due to low collision rates will focus on bulk particle production, CBM will put special emphasis on the measurement of extremely rare probes which have not been accessible by previous heavy-ion experiments at the AGS and the SPS.

The observables to be covered by CBM include multiplicities, phase space distributions and flow of strange and multi-strange hadrons (K,φ, Λ, Ξ, Ω) and charmed hadrons (D,D_s, Λ_c). The in-medium properties of short-lived vector mesons (φ, ω, φ) will be investigated via their di-leptonic decay. The measurement of lepton pairs will also give access to charmonium states which, together with the open charm measurements, will allow a comprehensive study of charm production near threshold. Signatures of the critical point will be looked for in event-by-event fluctuations of quantities like particle yield ratios, charged multiplicity or average p_t

3.2 Physics Aspects and Observables

The high-intensity heavy-ion beams of the future FAIR accelerators, together with the planned Compressed Baryonic Matter (CBM) experiment, offer excellent possibilities to produce and to investigate baryonic matter at highest densities in the laboratory. The research program concentrates on the study of the structure and of the equation-of-state of baryonic matter at densities comparable to the ones in the inner core of neutron stars [55]. This includes the search for the phase boundary between hadronic and partonic matter, the critical endpoint, and the search for signatures for the onset of chiral symmetry restoration at high net-baryon densities.

The experimental and theoretical challenge is to study the probes. In high-energy nucleus-nucleus collisions the evolution of the fireball from the early hot and dense stage to its disintegration into hadrons-takes only a few 10^{23}s. The experimental observables are the yields and phase-space distributions of newly created particles, and their correlations and fluctuations. The different particle species probe different phases of the transient fireball depending on their mass, energy, production, and interaction cross-sections, and decay channels. This is schematically illustrated in fig 3.2, which depicts three snapshots succeeding in time as calculated with a microscopic transport model for a U + U collision at 23 GeV/nucleon beam energy [56].

Particles containing heavy quarks like charm are created in the early phase of

the collision, in particular at FAIR energies that are close to the threshold for the production of charm-anti-charm pairs. Therefore, the yield and the phase space distributions of charmed particles are expected to be particularly sensitive to the
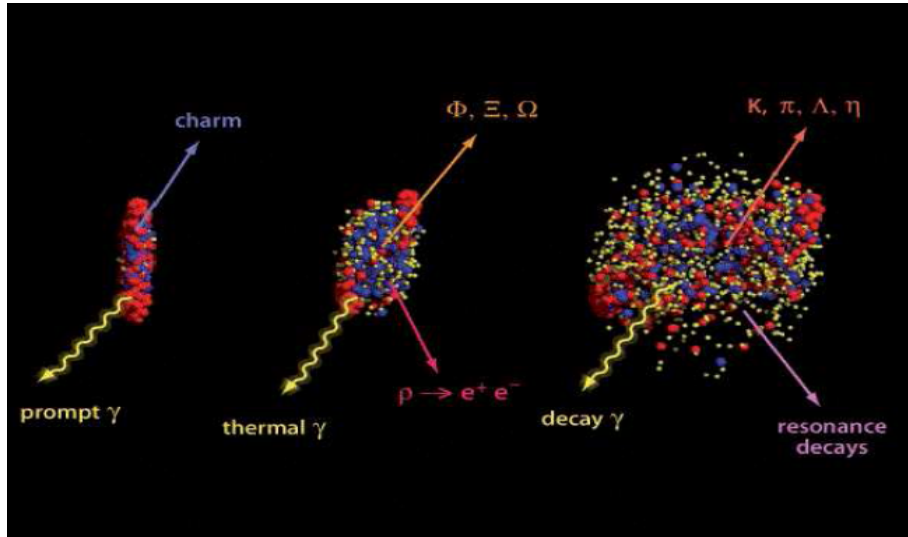
Figure 3.2: *Sketch of the expansion phase of a U + U collision at 23 GeV/nucleon beam energy at different time steps [56].*

conditions inside the early fireball. Most of the charm quarks are carried away in D-mesons, which contain one charm and one light quark. Theory predicts that the properties of D-mesons are modified in the dense medium [57], and, hence, offer the possibility to study the effect of chiral symmetry restoration at highest densities. Some of the created charm-anti-charm pairs form charmonium, which disintegrates much easier in quark-gluon matter than in hadronic matter, thus probing the structure of the fireball [58]. No charmed particles have been measured in the FAIR energy range.

The aim of the CBM experiment is to provide a comprehensive and precise data set based on the measurements of the observables mentioned earlier for a variety of projectile and target masses, beam energies, and impact parameters. Important for the interpretation of results of the heavy-ion collision experiments are comparisons to data obtained in proton-nucleus and proton-proton collisions. The FAIR accelerators deliver proton beams up to an energy of 90 GeV, which permits investigations of elementary processes like charm production in an energy

range where no data exist. Nuclear reactions in the energy range from 2 to 10 GeV/nucleon will be studied with an upgrade of the HADES spectrometer, which is currently being operated at the GSI SIS-18 accelerator.

3.3   The CBM Detector System

The detectors and their readout electronics should be fast, radiation hard and should cover a large acceptance with full azimuthal coverage. The data acquisition system should be efficient and fast.

The track reconstruction algorithms should provide high precision and fast on-line tracking, with high efficiency and excellent momentum resolution. A very good particle identification capability both for hadrons and leptons is required.

A schematic view of the proposed detector concept is shown in fig 3.3. In the present design, CBM has two detector configurations: one is specialized for electron identification (electron configuration) and the second is specialized for muon identification (muon configuration). Both setups are not compatible as the muon measurements require efficient particle absorbers which would not allow for electron measurements.

The two configurations of the CBM detector which are being evaluated for electron-hadron and muon-hadron measurements (see fig 3.3) may be realized at different stages. They have in common a low mass silicon tracking system (STS), the central detector to perform charged-particle tracking and high-resolution momentum measurement with radiation tolerant silicon microstrip or pixel detectors. Combined with an ultra-thin micro-vertex detector (MVD) based on monolithic active pixel sensors, it will be installed in the gap of a dipole magnet in short distance downstream of the target, typically a gold foil of 250 μm thickness corresponding to 1% nuclear interaction length.In the electron-hadron configuration, the CBM experiment comprises a ring imaging Cherenkov (RICH) detector downstream of the magnet to identify electron pairs from vector meson decays. Transition radiation detectors (TRDs) provide charged particle tracking and the identification of high energy electrons. Hadron identification will be realized in a time-of-flight (TOF) system built from resistive plate chambers (RPC). An electromagnetic calorimeter (ECAL) will be used for detecting direct photons. The projectile spectator de-
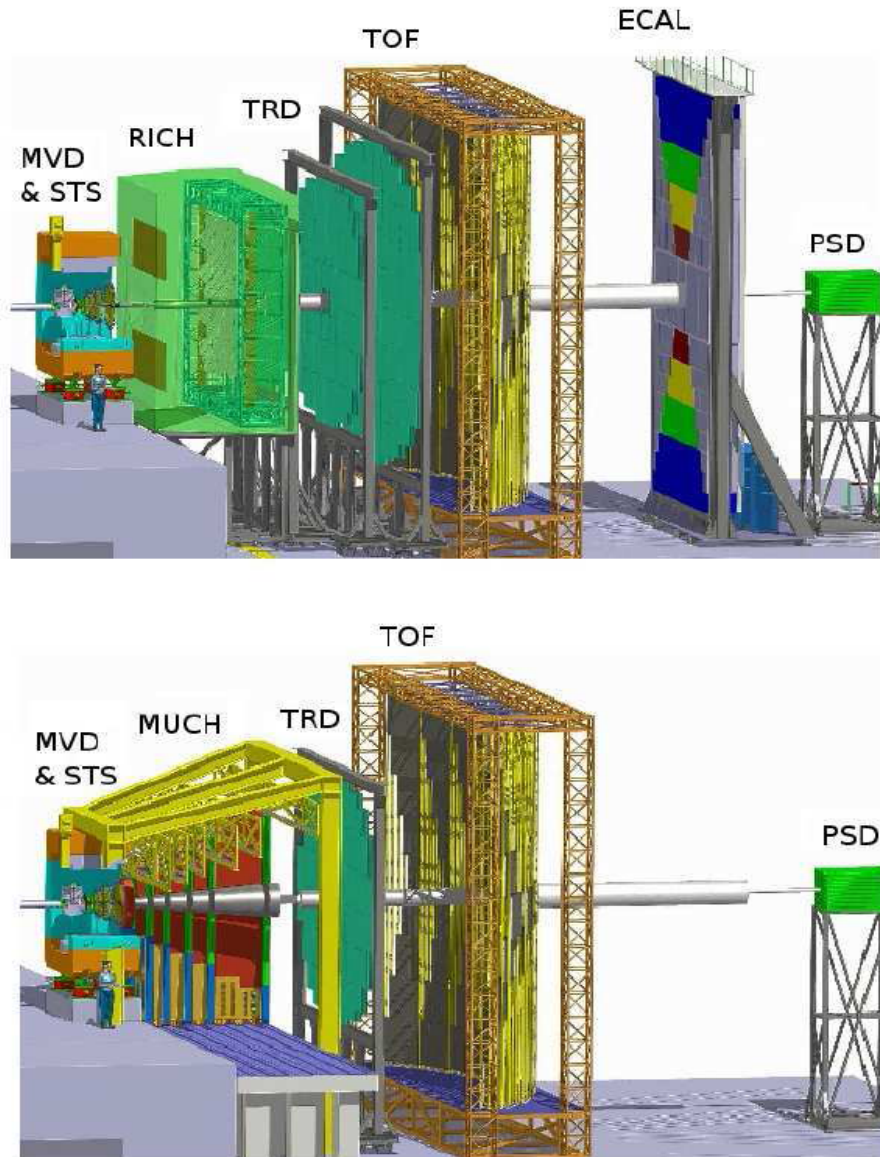
Figure 3.3: *Current setup for the CBM experiment planned at FAIR. The upper part shows the option which allows an electron measurement with a RICH and three stations TRD with 3-4 layers each. The lower part shows muon detection system consisting of hadron absorber layers and tracking detector layers.*

Observables	MVD	STS	RICH	MUCH	TRD	RPC	ECAL	PSD
π,K,p		x	(x)		(x)	x		x
Hyperons		x			(x)	(x)		x
Open charm	x	x	(x)		(x)	(x)		x
Electrons	x	x	x		x	x		x
Muons		x		x		(x)		x
Photons							x	x
Photons ($e^{\pm}$)	x	x	x		x	x		x

Table 3.1: *Observables and required detectors: Micro-Vertex Detector MVD, Silicon Tracking Station STS, Ring Imaging Cherenkov detector RICH, Muon Chambers MuCh, Transition Radiation Detector TRD, timing Resistive Plate Chambers RPC, Electromagnetic Calorimeter ECAL, Projectile Spectator Detector PSD. Detectors marked as (x) can be used to suppress background*

tector (PSD) is a calorimeter that determines centrality and reaction plane of the collisions. In the muon-hadron configuration of the experiment, the RICH detector system is replaced by a compact active absorber system (MUCH). Vector mesons are detected via their decays into muon pairs. Hadrons can be measured with the absorbersmoved out. A particular feature of the experiment is its data acquisition and trigger concept, imposed by the physics programme with rare probes, e.g. charm production near threshold, and the necessity for interaction rates between 0.1 and 10MHz. It is based exclusively on self-triggering front-end electronics to time-stamp and to ship the detector signals to a fast computing farm for event building and high-level trigger generation.

A key feature of the CBM experiment is online event selection which requires free streaming read-out electronics and fast algorithms running on computer farms based on future many-core architectures.

The CBM detector components required for the measurement of the different observables are listed in Table 3.1.

3.3.1 Silicon Tracking Systems (STS)

The Silicon Tracking System (STS) is the central component of the CBM experiment.The task of the STS is to provide track reconstruction and momentum determination of charged particles. The multiplicity of charged particles is up to 600 per event within the detector acceptance. A particular challenge for the STS is to achieve high track reconstruction efficiency in a high track density environment (typically, several hundreds charged particles per central Au+Au event within the acceptance of the STS). The requirements for precise and fast tracking in a combination with the high hit rates expected, put strong constraints on the material budget, the radiation tolerance and the readout speed of the STS.
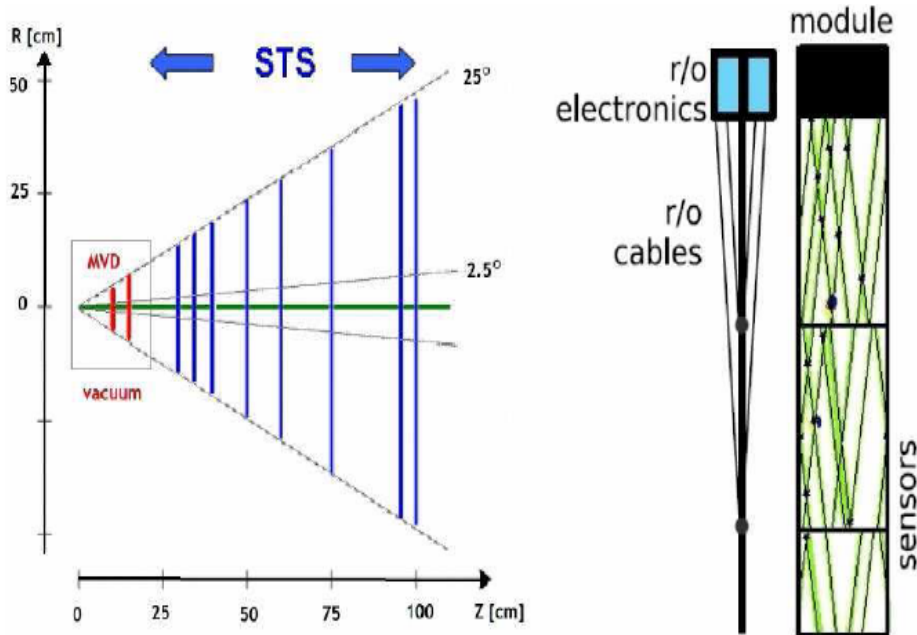
Figure 3.4: *(a) Layout of the STS and MVD stations. The locations of the stations and their polar angle coverage are indicated. (b) One STS module with the read-out electronics: side view and front view.*

In its currently studied versions the STS consists of up to 8 tracking layers of silicon detectors as shown in fig 3.4. They are located downstream of the target at distances of 30, 35, 40, 50, 60, 75, 95, and 100 in a magnetic dipole field of about 1 Tm bending power. The required momentum resolution is of the order of $\Delta p/p =$

1%. This performance can only be achieved with an ultra low material budget of the stations, imposing particular restrictions on the location of power-dissipating front-end electronics in the fiducial volume. The concept of the STS tracking is based on silicon micro-strip detectors on lightweight ladder-like mechanical supports.

3.3.2 Micro-Vertex Detector (MVD)

The identification of D mesons via their weak hadronic decay into pions and kaons requires a dedicated Micro-Vertex Detector in addition to the STS. The D meson lifetimes are $\tau = 123\mu m/c$ for D^0 and $\tau = 314\mu m/c$ for $D^\pm$. In order to suppress the background of promptly emitted pions and kaons one has to determine the secondary decay vertices of D mesons with extremely high precision.

The Micro-Vertex Detector of CBM will be composed of two or three ultra-thin detector layers based on monolithic active pixel sensors (MAPS) operated in vacuum close to the target. These type provides a low enough material budget and sufficient coordinate resolution for high-precision vertex detection, as shown in fig 3.5. However, both radiation hardness and read-out speed do not fulfill the CBM requirements at present. R&D to improve on these issues is ongoing at IPHC Strasbourg.

The MVD will be installed for dedicated measurements of open charm where the secondary vertex has to be determined with high resolution, and for electron measurements where close pairs have to be rejected in order to reduce the combinatorial background. The MVD information improves hyperon identification and the detector might be used also for this purpose

3.3.3 Ring Imaging Cherenkov Detector (RICH)

In CBM, the RICH detector will serve for electron identification with momenta upto 10-12 GeV/c and for π identification for higher momenta in order to improve the K/π separation which quickly deteriorates for p > 4 GeV/c if only time-of-flight information is used. A pion suppression of $10^2 - 10^3$ has to be provided by the RICH. In the current CBM detector layout the RICH would be placed behind the magnet (roughly 1.5m downstream the target) and in front of the first transition radiation detector. High detection efficiency of electrons is required which calls for
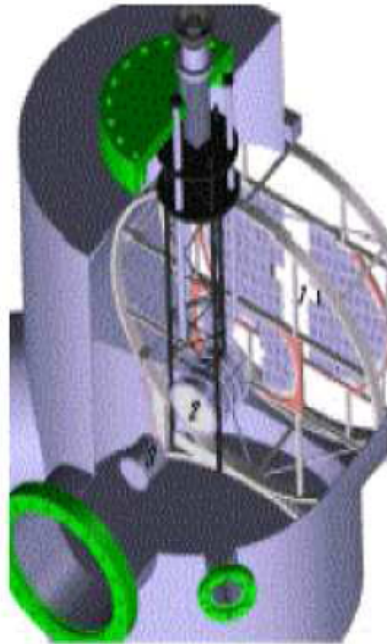
Figure 3.5: *First design studies of the MVD detector.1: MAPS stations can be moved to allow beam tuning, 2:target holder, 3: engine to move detector stations.*

10-15 hits per electron ring at minimum. As global tracking has to connect tracks in the STS and TRD, the RICH detector should not exceed 3m and a material budget of 3-4% radiation length in order to reduce multiple scattering. A large acceptance of 25^0 in polar laboratory angles has to be covered to identify the vector mesons in a wide range of rapidity and transverse momentum.

3.3.4   Transition Radiation Detector (TRD)

The TRD contributes to the electron identification and tracking of charged particles. For discriminating electrons from pions in the momentum region of a few GeV/c, a TRD exploits, one hand, their different energy loss through ionisation. On the other hand, electrons produce additional transition radiation which is then used by the TRD for their identification. Transition radiation is produced when a relativistic particle traverses an inhomogeneous medium, in perticular the boundary between materials with different di-electric constants. Currently, the TRD is envisaged to

be a system composed of three stations with three to four layers each, located at distances of 5m, 7.25m, and 9.5m from the target. The total active area covered is about $600m^2$. Each layer consists of a radiator where the transition radiation is produced by electrons, and of gaseous detector in which the deposited energy of charged particles and the transition radiation can be measured.

The detector development concentrates on the improvement of the electron identification performance, and on the development of highly granular and fast gaseous detectors in particular for the inner part of the detector planes covering forward emission angles. For example, at small forward angles and at a distance of 5 m from the target, we expect particle rates on the order of 100 kHz/cm^2 for 10 MHz minimum bias Au+Au collisions at 25A GeV.

3.3.5   Time of Flight (TOF)

The identification of pions, kaons and protons emerging from close to the interaction point will be accomplished by a time-of-flight (TOF) system located about 10m downstream of the target. The measurement of flow and event-by-event fluc-

Figure 3.6: *(a) Time resolution of a prototype single-gap RPC as function of counting rate, obtained at LIP Coimbra. (b) Reconstructed squared mass of primary hadrons in the TOF acceptance as a function of momentum [60].*

tuations of particle yield ratios requires a large ($\approx 2\pi$) and approximately uniform acceptance; consequently, a large area of about $120m^2$ must be covered. The timing resolution required for the separation of kaons and pions for momenta upto 4 GeV

is about 80ps.

A time-of-flight (TOF) measurement which is used to identify charged particles: the determination of the particle mass is based on the measurement of the time of flight, the particle momentum and the particle track length. The TOF wall, consists of approximately 60,000 independent cells providing a resolution of $\sigma_{TOF} \leq 80$ ps [59]. The TOF stop detector of CBM has an active area of about $150m^2$ located at a distance of 10 m from the target. A diamond pixel (or micro-strip) detector provides the start signal for the TOF measurement. It directly counts the beam particles at intensities of up to 10^9 ions/s. The requirements for the TOF detector can be satisfied by a tRPC (timing Resistive Plate Chamber) with $25^{'}30^0$ coverage in $\theta(\sim 150m^2)$.

Fig 3.6(b) demonstrates the hadron identification capabilities of the TOF system. Kaons can be separated from pions for momenta upto 4 GeV, while protons can be identified upto 8 GeV. The acceptance for identified hadrons, shown in fig 3.7, covers the bulk of the production for all three particle species.
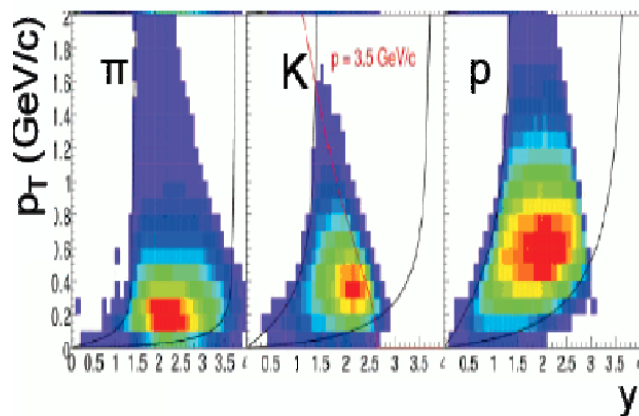
Figure 3.7: *Distribution of TOF-identified primary hadrons in rapidity and transverse momentum in central Au+Au collisions at 25 AGeV. Mid-rapidity is 1.98.*

3.3.6   The Electromagnetic CALorimeter (ECAL)

A "shashlik" type calorimeter as installed in the HERA-B, PHENIX and LHC experiments will be used to measure direct photons and neutral mesons (π^0, η)

decaying into photons. The ECAL will be composed of modules which consist of 140 layers of 1 mm lead and 1 mm scintillator, with cell sizes of $3 \times 3\ cm^2$, $6 \times 6\ cm^2$, and $12 \times 12\ cm^2$. The shashlik modules can be arranged either as a wall or in a tower geometry with variable distance from the target. Ongoing studies concentrate on an optimization of the layout, in particular in terms of required azimuthal coverage.

3.3.7 The Projectile Spectator Detector (PSD)

The PSD will be used to determine the collision centrality and the orientation of the reaction plane. A very precise characterization of the event class is of crucial importance for the analysis of event-by-event observables. The study of collective flow requires a well defined reaction plane which has to be determined by a method not involving particles participating in the collision. The detector is designed to measure the number of non-interacting nucleons from a projectile nucleus in nucleus-nucleus collisions. The PSD is a full compensating modular lead-scintillator calorimeter which provides very good and uniform energy resolution [61]. The calorimeter comprises 12×9 individual modules, each consisting of 60 lead/scintillator layers with a surface of $10 \times 10\ cm^2$. The scintillation light is read out via wavelength shifting (WLS) fibers by Multi-Avalanche Photo-Diodes (MAPD with an active area of $3 \times 3\ mm^2$ and a pixel density of $10^4/mm^2$).

By using this layout, within a simulation of Au+Au collisions at 10 AGeV, an impact parameter resolution of $\Delta b/b = 0.1$ was determined for peripheral collisions and worsens to $\Delta b/b = 0.5$ for most central collisions [62]. Note that the resolution is dominated by the physical fluctuations of the number spectators.

3.4 Muon Chamber System (MUCH)

The second detector configuration in CBM (lower part of fig 3.3) includes a muon chamber system. In this configuration, vector mesons, ρ, ω, ϕ, and J/Ψ, will be reconstructed via their decay into dimuons instead of dielectrons. A possible set up for the Muon Chamber system is shown in fig 3.8. The CBM Indian group holds the responsibility of designing and building of a muon detector system to enable di-muon measurements [63]. An optimized version of the muon detection system has
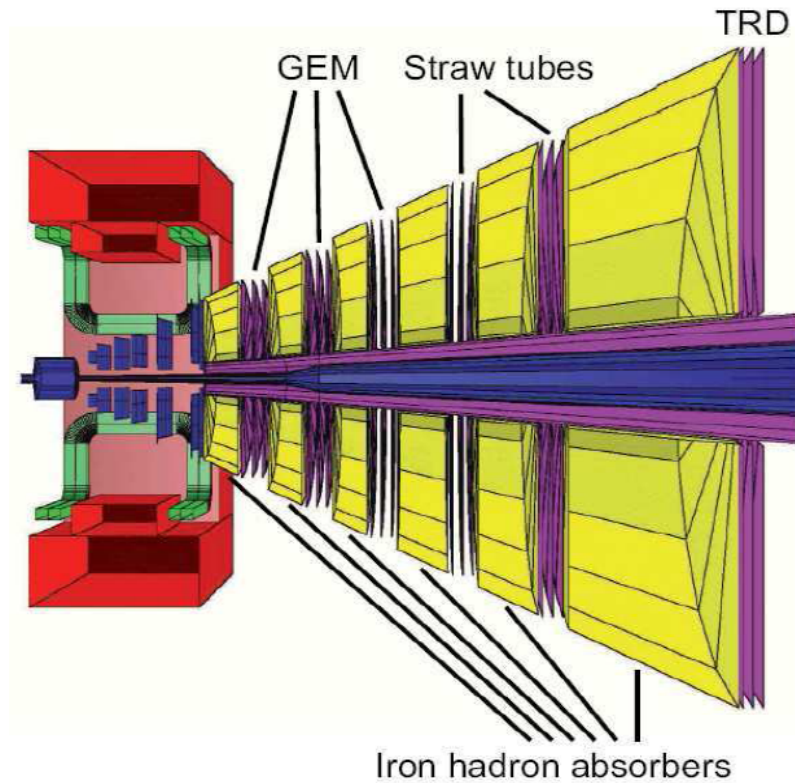
Figure 3.8: *The CBM Muon Detection System consisting of alternating layers of iron absorbers (yellow) and muon chambers (purple).*

already been designed through simulations, as shown in Fig. 3.8. It includes 6 iron absorbers and 6 tracking stations. Each tracking station consists of three chambers located in the air gap between two successive absorbers. The total absorber length in the current design amounts to 2.25 m of iron. This geometry can be used for both charmonium and low mass vector mesons (lmvm).

The alternating absorber and detector layers serve respectively for hadron suppression and track reconstruction. Candidate technology for the detectors located in the absorber gaps are GEMs and straw tubes. The tracking and momentum determination of particles is done with the STS. The current design of the muon detection system foresees 18 detector stations and 6 segmented iron absorbers. In this case, the total material budget would correspond to 13.5 times the nuclear interaction length. Promising candidates for the fast and highly granulated detectors,

located in the five gaps between the absorber layers, are gaseous detectors based on GEM technology [64], straw tubes, and one of the TRD stations. The total area covered by the muon chambers is about 70 m^2.

Currently, it is not yet decided if the "electron" or the alternative "muon setup" will be built. The solution offering the most comprehensive research program would be to build both setups which can be used alternately. In that case, the RICH has to be temporary removed and the last 3 detectors of the MuCh can correspond to tracking detectors which will anyway be in place in order to cover the gap between STS and TOF. The TRD, for example, could be used for this purpose, too. Of course, the ECAL cannot be used in conjunction with the muon detection system.

3.4.1 Gas Electron Multiplier

The gas electron multiplier (GEM) [65] invented by F. Sauli in 1996 at the Center of European Nuclear Research (CERN) [66] is part of the class of micro-pattern gas detectors and is one of its most successful representatives. In fact, interest in GEM-based radiation detectors is steadily growing.

A unique property of GEMs is the possibility of their operation in pure noble gases in the avalanche mode with a high gas gain, including operation at high pressures and cryogenic temperatures.

Gas Electron multipliers (GEM) will be used in the CBM Muon Chamber system (MUCH) located downstream of the Silicon Tracking System (STS) along with other sophisticated detectors. In the GSI detector laboratory an R&D (Research and Design) effort is launched to study the characteristics of GEM detectors for the CBM experiment. The primary goals of this R&D program are

(a) to verify the stability and integrity of the GEM detectors over a period of time, during which a charge density of the order of several C/cm^2 is accumulated in the detector;

(b) to establish the functioning of a triple GEM as a precise tracking detector under the extreme conditions of the CBM experiment;

(c) to study characteristic parameters like efficiency, rate capability, long-term stability, spark probability by varying conditions like temperature, gas composition or radiation dose.

For inclusion of a realistic scenario, modular structure has been implemented in

simulation. Each detector layer has been divided in several modules of size 30 cm. x 30 cm. (limited by the GEM foil production technology) and filled with an argon based gas mixture as the active medium. Up till now all the feasibility studies have been done with this modular design. However one practical disadvantage of this modular design is the non-availability of large size GEM modules which in turn results in complex detector design and large number of dead zones. One possible solution to this problem is to divide the detector planes into several sectors instead of modules. In case of sector design, large GEM foils limited by 60 cm size (width) in one direction and no limitation in length are available and prototypes are being made by CMS and other experiments. These GEMs are produced using single-mask technology which gives significantly larger yield of good foils compared to the conventional double-mask GEM. In this paper we report the first results of our feasibility study with sectored MUCH geometry.

3.4.2 R&D on Detectors

Prototype detectors using 10 cm $\times$ 10 cm triple-GEM stack with a drift mesh and pad readout have been built at VECC. The chambers have been tested with radioactive sources and proton beams. Argon (Ar) and Carbon dioxide (CO_2) mixed in the ratio 70:30, was used as the gas mixture. Cosmic tests performed with one such chamber yielded a charged particle detection efficiency of 95 % . A set of chambers were tested with 2.5 GeV/c proton beams at SIS-18 beam line at GSI.

Simulations are being performed for the optimization of the detector design and to study the feasibility of the di-muon measurement. The feasibility studies are done within the CBM simulation framework [67] which allows full event simulation and reconstruction.

The detection procedure involves the reconstruction of the track parameters in STS and extrapolation to muon detecting stations through the absorbers. Selection of the number of muon stations decide the identification of muons from low mass vector mesons (LMVM) and charmonia. While the LMVM muons travel shorter distances, J/ψ muons cross the thick absorber and reach till the end. They have therefore taken tracks travelling through 15 layers and 18 layers as valid muon candidates from LMVM and charmonia respectively. They have segmented the
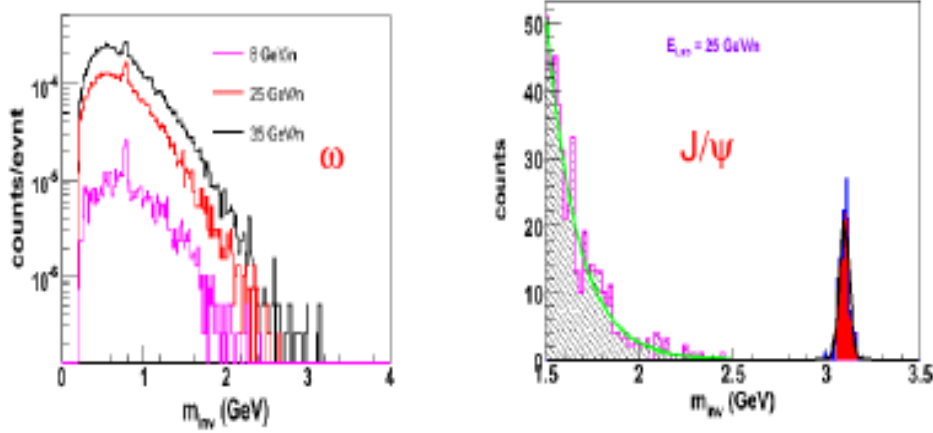
Figure 3.9: *Invariant mass spectra of ω (left) and invariant mass spectra of J/ψ (right).*

Energy (A GeV)	Efficiency (%)		S/B	
	$J/\psi \longrightarrow \mu^+\mu^-$	$\omega \longrightarrow \mu^+\mu^-$	$J/\psi \longrightarrow \mu^+\mu^-$	$\omega \longrightarrow \mu^+\mu^-$
8	4.9	0.96	3.3	1.41
25	13	1.58	7	0.49
35	13	1.82	11	0.34

Table 3.2: *Reconstruction Efficiency and (S/B) ratio of J/ψ and ω in central Au-Au collision at 8,25 and 35 AGeV beam energies(Input events: 10k UrQMD+PLUTO).*

detector into pads of varying size from 4mm × 4mm to 3.2cm × 3.2 cm depending upon the radial distribution of particle density. The reconstruction efficiency and signal to background ratio (S/B) of ω & J/ψ mesons were calculated in a $\pm 2\sigma$ window around the signal invariant mass peak and are presented in Table 3.2, for central Au-Au collisions at 8,25 and 35 AGeV beam energies. Figures 3.9 show the invariant mass spectra of ω and J/ψ via di-muon channel. The combinatorial background is calculated using Super Event (SE) Analysis technique where tracks having opposite charges from different UrQMD events are combined. Our studies indicate that both low mass vector mesons and charmonia can be identified above the combinatorial background which is dominated by muons from weak pion decays.

3.4.3 Straw Tube Subsystem of MUCH Detector

CBM Muon Detector (MUCH) should provide an identification of muons in heavy-ion collisions at FAIR energies [68]. The detector consists of several hadron absorber layers with intermediate gas tracking detectors. The coordinate detectors will be used for tracking of charged particles produced at scattering angles from 5.7 to 26.6^0. Tracking detectors based on drift tubes will be used for the two last gaps of the absorber layers (stations 4 and 5). To ensure the low occupancy and high uniformity of the detector, it is planned to make use of thin-walled 6 mm straws for these tracking stations.

Each straw station contains three identical octagonal chambers and two rotated (+10, -10) coordinates of a passing charged particle. Each chamber consists of two identical modules with some overlap between them to avoid dead regions. The chambers have an inner hole for the beam pipe with a diameter of 43 cm. Figures 3.10 show the schematic layout of the straw module and the straw chamber, respectively.
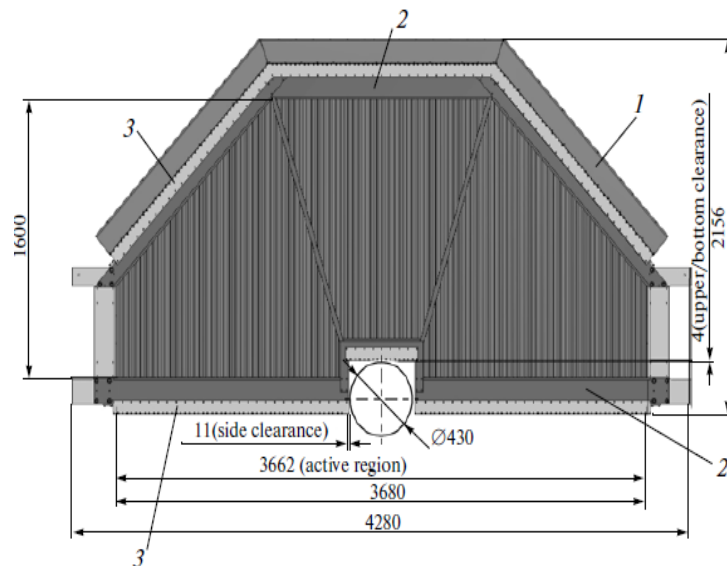
Figure 3.10: *Schematic view of the MUCH straw module. 1 mother boards for the readout and high voltage supply of the straw anodes; 2 carbon plastic elements, and 3 Al elements.*

The current MUCH straw subsystem design is based on straw tubes with a diameter of 6 mm. The tube parameters (60 ns maximum drift time and 35 ns pulse duration), as well as maximum value of the occupancy ($0 < 7\%$) in central Au-Au collisions (as found from Monte Carlo simulations), are in good match with the maximum 10 MHz rate of Au-Au collisions at 25 A GeV in the CBM setup [68]. However, even though these parameters seem to be adequate for the expected running conditions, a possibility to adapt the straw detector concept to the cases where a higher granularity is required was studied and confirmed [69, 70, 71, 72]. The beam test of the prototype with a granularity of 4 cm^2 had shown that its time and spatial parameters do not differ from those of conventional tracking detectors based on drift tubes [73, 74, 75]. The developed method for manufacturing straw coordinate detectors makes it possible to achieve a granularity as fine as 1 cm^2 with the straw full length up to 4 m.

3.4.4 MUCH Geometry

The muon detection system which will track the particles after STS will consist of series of iron absorbers, for hadron absorption and a number of tracking detectors sandwiched between them. The standard design includes 6 iron absorbers and 18 detector layers (3 behind each absorber). The total absorber length in the current design amounts to 2.25 m of iron. The detection procedure is to continuously track all charged particles through the complete absorber, starting with the tracks measured by the Silicon tracker (which defines the momentum). This will ensure high tracking efficiency even for low momentum muons which are required for the low mass vector meson measurement. An additional shielding is used around the beam pipe in order to reduce the background of secondary electrons produced in the beam pipe [76].

They also explored the possibility to perform muon detection with reduced (9 layer) and intermediate(12 layer) geometry as shown in fig 3.11.The reduced geometry consists of 3 hadron absorber layers (iron plates of thickness 30cm, 95cm and 100cm) and 9 layers(made of GEM) located in triplets behind each absorber. Here the definition of LMVM track is that it should pass through 2 layers of absorber(125cm). The intermediate geometry consists of 4 hadron absorber layers(iron plates of thickness 30cm,30cm 65cm and 100cm) and 12 detector layers made
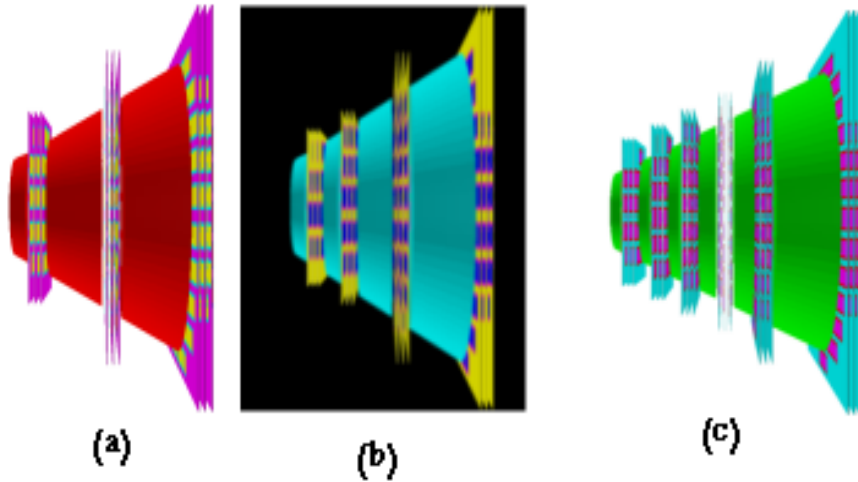
Figure 3.11: *Geometry: (a) Reduced, (b) Intermediate and (c) Standard*

of a micro-pattern detector technology known as GEM and is located in triplets behind each absorber. Here the definition of LMVM track is that it should pass through 3 layers of absorber(125cm).

3.4.5 Di-muon measurements

The emission of lepton pairs out of the hot and dense collision zone of heavy-ion reactions is a promising probe to study the electromagnetic structure of hadrons under extreme conditions. The reconstruction of vector mesons $(\rho, \omega, \phi, J/\Psi, \Psi')$ is one of the prime tasks of the CBM experiment. The proposed muon system is intended to do this study using a dimuon decay mode.

Since the dimuon yield from vector meson decays is expected to be very low, it is essential to develop a fast and efficient trigger for such events.

The muons from decays of low-mass vector mesons (LMVM), e.g., ω, will be rather soft, making it undesirable to use the total absorber thickness. Therefore, the detector stations surrounding the last but one absorber should be used in the trigger in a manner described in [77]. Here somewhat different aspects of this problem are addressed.

As in the case of the tracking performance analysis, for the LMVM trigger study both the alternative MUCH configurations were considered in order to compare

their ability to do the job. It was also useful to obtain a tool independent of the general tracking to compare two detector configurations (keeping in mind that the general tracking might not be fully tuned to properly handle the heterogeneous detector environment).

The following event selection strategy was used:

• find track segments in stations 4 and 5;

• merge track segments from different stations taking into account the multiple scattering in the absorber;

• propagate track to the target position using linear extrapolation;

• apply a cut on radial position of the extrapolated points;

• accept event if two or more tracks pass the cuts.

In order to ensure a fair comparison of the two detector configurations, the following implementation details were considered:

• simplified (planar) GEM geometry: automatic segmentation and simple digitization and hit finding;

• 6 mm straw tubes: hit producer with hit merging (i.e., only one hit per tube is kept) and left-right ambiguity (i.e., for each "true" hit a mirror one (symmetric relative to anode wire position) is added (no local left/right ambiguity resolution);

• track segments should include the maximum number of hits (i.e., 3 for GEMs and 6 for straws);

• segment merging: introduced multiple scattering parameters $\sigma_{\alpha\beta}$ and σ_{xy} (thick scatterer approximation) which were obtained from simulation.

The trigger efficiency and background rejection factor were estimated on Monte Carlo event samples of UrQMD central Au + Au events at 25A GeV mixed with $\omega \longrightarrow \mu^+\mu^-$ decays and minimum bias events, respectively. The obtained results are presented in Table 3.3. One can see that both detector configurations demonstrate the similar performance.

3.5   Muon Simulations

At FAIR energies the muon momenta can be rather low, and, therefore, we develop a muon detection concept with a dynamical definition of absorber thickness according to the muon momentum. The actual design of the muon detector sys-

Geometry	Efficiency, %	Background rejection
GEM	6.7±0.4	19.8
Straws	6.7±0.4	19.7

Table 3.3: *Trigger efficiency for the dimuon signal and background rejection factor.*

tem consists of 6 hadron absorber layers (iron plates of thickness 20, 20, 20, 30, 35, 100 cm) and 18 gaseous tracking chambers located in triplets behind each iron slab. The absorber/detector system is placed downstream of the Silicon Tracking System (STS) which determines the particle momentum. The definition of a muon depends on its momentum which varies with the mass of the vector mesons and with beam energy. For example, muons from the decay of J/ψ mesons have to pass all 6 absorber layers with a total iron thickness of 225 cm corresponding to 13.4 interaction length λ_I . The muons from the decay of low-mass vector mesons (ρ, ω, ϕ) only have to penetrate through 5 iron absorber layers with a total thickness of 125 cm (corresponding to 7.5 λ_I).

The invariant mass distributions of electron-positron pairs simulated for central Au+Au collisions at 25 AGeV are shown in Fig 3.12. The background is generated by UrQMD, the multiplicity of vector mesons is calculated with the HSD code, and the phase space distributions of the vector mesons and their decay into di-electrons is simulated with the PLUTO (thermal source) generator. The dominating electron background contribution is from γ-conversion in the target. Thus, both for low-mass vector meson and for charmonium simulations, an Au-target of 25 μm (0.1% interaction length) is used. When implementing this thin target the remaining background is dominated by electrons from $\pi^0$0-Dalitz decays. In order to enhance the statistics for J/ψ mesons a segmented target will be used in the experiment.

The J/ψ simulations are performed with 8 silicon micro-strip detectors only, no MVD was implemented. In order to reduce the contribution of electrons from γ-conversion in the target (which is the dominant background source for a 1% interaction target) the thickness of the gold target was chosen to 25 μm corresponding to an interaction probability of 0.1%. The combinatorial background is drastically reduced by rejecting single electrons with transverse momentum below 1.2 GeV/c.
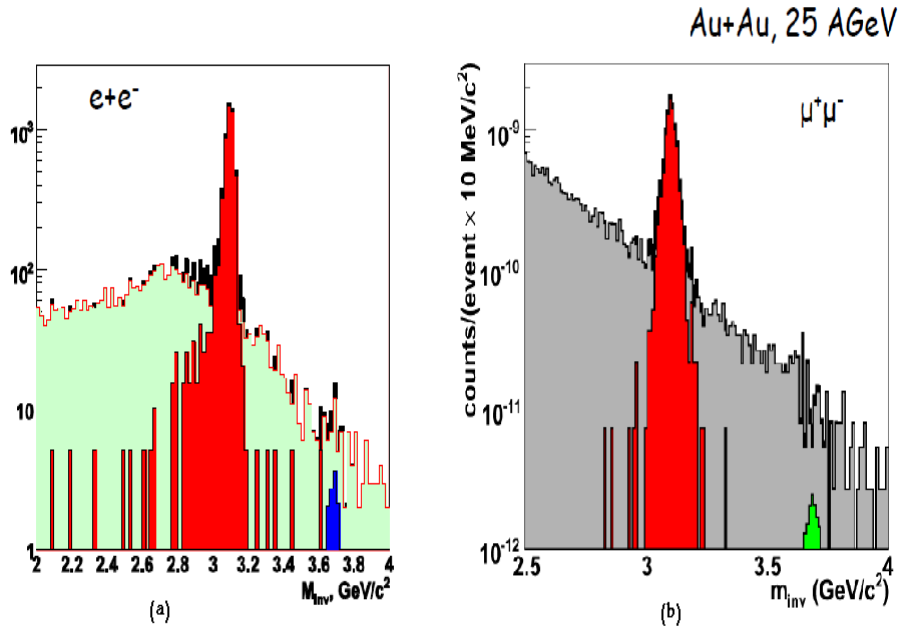
Figure 3.12: *Invariant mass spectra of electron-positron pairs simulated for central Au+Au collisions at 25 AGeV:(a) low mass di-electrons simulated for 200 k central collisions with a cut on $pT > 0.2 GeV/c$ for single electrons. (b) J/ψ and ψ' for 4.10^{10} central events, $pT > 1.2 GeV/c$ for single electrons*

The remaining background is due to electrons from π^0-Dalitz decays. In order to perform high statistics measurements for charmonium a segmented target will be used, and a trigger concept has to be developed.

Chapter 4

QCD Critical Point at FAIR Energies

4.1 Introduction

The vacuum of quantum chromodynamics (QCD) is believed to undergo a phase transition to the quark-gluon plasma (QGP) at high temperature T and/or at high quark chemical potential μ. Such a new state of matter is expected to be produced in on-going heavy-ion collision experiments at the BNL Relativistic Heavy-Ion Collider (RHIC) and in the future Large Hadron Collider (LHC) [78].

Mapping the QCD phase diagram is one of the fundamental goals of heavy-ion collision experiments. QCD critical point is a distinct singular feature of the phase diagram, the existence of which is a ubiquitous property of QCD models [79] based on chiral dynamics. Locating the point using first-principle lattice calculations is a formidable challenge and, while recent progress and results are encouraging, much work needs to be done to understand and constrain systematic errors [80]. If the critical point is located in the region accessible to heavy-ion collision experiments it can be discovered experimentally. The search for the critical point is planned at the Relativistic Heavy Ion Collider (RHIC) at BNL, the Super Proton Synchrotron (SPS) at CERN and the future Facility for Antiproton and Ion Research (FAIR) at GSI.

4.2 Critical Point in Quark Gluon Plasma

The study of critical points-the locations on a phase diagram where the boundary between phases disappears-has a very long history, starting with the observation of the critical point in water at the beginning of the 19th century. Recently, considerable attention has been paid to whether a critical point exists on the phase diagram of strongly interacting matter, which is known under various names as nuclear matter, quark matter or quark gluon plasma. One very important issue is whether the critical point can be found in experiments that involve colliding heavy nuclei. The most widely discussed signal of the critical point is the enhancement of fluctuations of final state observables, for example, the number of pions emitted in a collision.

As the Universe cools down, the interaction becomes strong and two things happen. The first is confinement: quarks and gluons are combined into hadrons (bound states of three quarks, or one quark and one antiquark). There does not have to be a phase transition associated with confinement alone (in a later state in the evolution of the Universe, electrons and protons would recombine into hydrogen without going through a true phase transition). The second phenomenon is spontaneous breaking of chiral symmetry. Under chiral symmetry, different types of quarks of left handedness (with spin pointing against the direction of motion) transform into each other, while independently right-handed quarks (spin pointing to the same direction as momentum) transform into each other. Chiral symmetry would be an exact symmetry of QCD if the quarks were massless. In the real world the u and d quarks (i.e., the two types of quarks that combine to form neutrons and protons) are not massless, but very light, so the chiral symmetry is not exact, but very good.

In the limit of massless quarks, there must be a phase transition related to chiral symmetry breaking The point where the phase transition line terminates is a critical point, similar to the critical point of water. It should be emphasized that the existence of the critical point follows from one single assumption, that the finite-μ chiral phase transition is first order.

In order to find critical point experimentally, The only way one can achieve temperatures and densities relevant for strong interactions is to collide heavy nu-

clei,like the nuclei of gold (with atomic number A = 197). Such collisions are currently performed at the Relativistic Heavy Ion Collider (RHIC) at Brookhaven National Laboratory. When two such nuclei are smashed together, a sequence of complicated processes occurs, but there are good indications that, for a brief time interval after the collision, one has a chunk of matter that behaves like a thermalized system, characterized by a temperature and a chemical potential. This tiny hot fireball expands, cools down, and eventually disintegrates into particles, tracing a trajectory on the phase diagram. With luck, one might be able to get this trajectory to pass close to the critical point.

It has been discussed in [81] from some years ago that near the critical point, the system has a "soft" mode, which is susceptible to external force. For example, in a magnetic system near the Curie point, the magnetic susceptibility χ of an Ising ferromagnet diverges as a power of the correlation length ξ as $\chi \sim \xi^{2-\eta}$, where $\eta \approx 0.12$. The susceptibility is not directly measurable in experiment, but is proportional to thermodynamic fluctuations, which are accessible experimentally. The signal of a critical point would be a non-monotonic behaviour of fluctuations. In the case of heavy-ion collisions one would see, for example, a bump in the fluctuations of the number of final state pions emitted in different collision events, $< (\delta N)^2 >$.
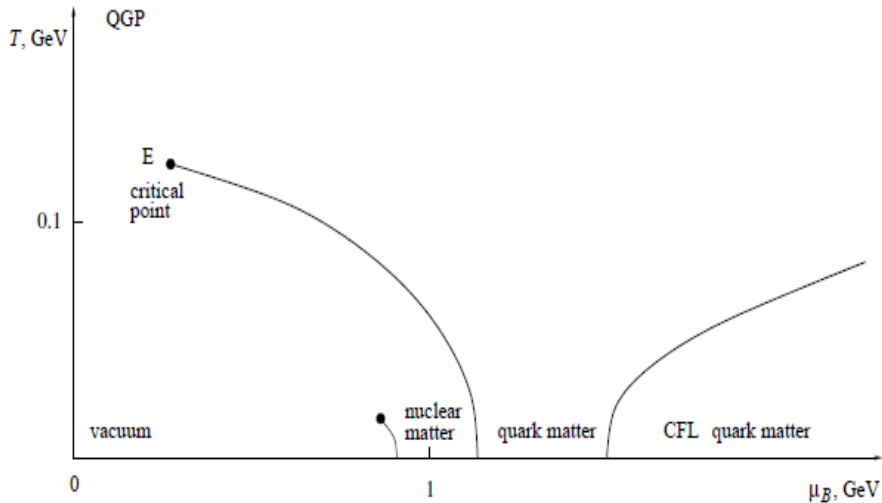
Figure 4.1: *QCD phase diagram*

The argument that the point E as shown in fig 4.1 must exist is short, and is based on a small number of reasonable assumptions The two basic facts that it relies on are as follows:
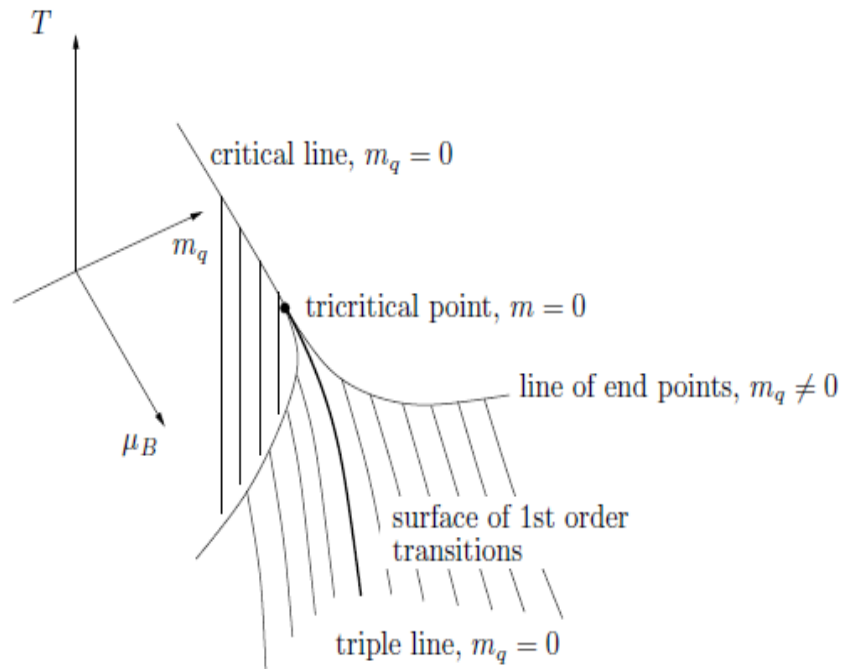
Figure 4.2: *A three-dimensional view (T , μ_B, m_q) of the QCD phase diagram near the tricritical point.*

(1) The temperature driven transition at zero μ_B is not a thermodynamic singularity. Rather, it is a rapid, but smooth, crossover from the regime describable as a gas of hadrons, to the one dominated by internal degrees of freedom of QCD quarks and gluons. This is the result of finite T lattice calculations [82].

(2) The μ_B driven transition at zero T is a first order phase transition. This conclusion is less robust, since the first principle lattice calculations are not controllable in this regime (naive Euclidean formulation of the theory suffers from the notorious sign problem at any finite μ_B). Nevertheless a number of different model approaches [83, 84, 85] indicate that the transition in this region is strongly first order.

(3) The last step of the argument is a logical product of (1) and (2). Since the first order line originating at zero T cannot end at the vertical axis $\mu_B = 0$ (by

virtue of (1)), the line must end somewhere in the midst of the phase diagram.

The end point of a first order line is a critical point of the second order. This is a very common critical phenomenon in condensed matter physics. Most liquids possess such a singularity, including water. The line which we know as the water boiling transition ends at pressure p = 218 atm and T = 374^0C. Along this line the two coexisting phases (water and vapour) become less and less distinct as one approaches the end point (the density of water decreases and of vapour increases), resulting in a single phase at this point and beyond.
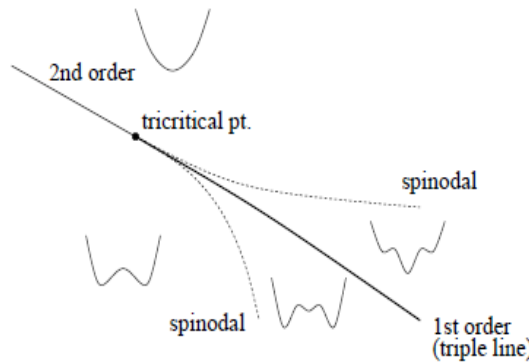
Figure 4.3: *Illustration of the shape of the effective potential for the chiral order parameter near the tricritical point in the $m_q = 0$ plane. Two additional (spinodal) lines, not present in Fig 4.2 indicate the boundary of the existence of metastable minima.*

Once the quark mass m_q is turned back on, the distinction between the symmetric and broken phases is blurred, and the second order phase transition is replaced by a smooth crossover.It is useful to take a look at Fig 4.2, where the 2-dimensional Tμ_B phase diagram is extended to 3-dimensions by adding the quark mass m_q as the third axis. One can see that the second order transition line at $m_q = 0$ does not extend into $m_q \neq 0$. This line can be seen as a boundary of the coexistence surface of the two spontaneously broken phases with $\langle \overline{\psi}\psi \rangle$ of opposite signs. A first order line ending at a critical point, on the other hand, exists for all nonzero (small) m_q, thus making up a surface which looks like two "wings" in Fig 4.2.

The tricritical point can be seen as the end of a first order line where 3 phases coexist (line of triple points).

Another useful sketch is made in Fig 4.3. It shows, in a schematic way, the shape of the effective potential in various regions around the tricritical point. One can see that the three minima, which are equally deep on the triple line fuse into one minimum at the tricritical point.

4.3   Signatures of the Critical Point

The most characteristic feature of a critical point is increase and divergence of fluctuations. Most fluctuation measures discussed to-date can be related to quadratic variances of event-by-event observables, such as particle multiplicities, net charge, baryon number, particle ratios, or mean transverse momentum in the event [86]. Typically, the singular contribution to these variances induced by the proximity of the critical point is proportional to approximately ξ^2, where ξ is the correlation length which, in the idealized thermodynamic limit, would diverge at the critical point [87]. The magnitude of ξ is limited trivially by the system size, but most stringently by the finite-time effects due to critical slowing down [87, 88]. The observation [88] that the correlation length may reach at most the value of 2   3 fm, compared to its "natural" value of 1 fm, may make discovering the critical non-monotonous contribution to such fluctuation measures a challenging task, if the measures depend on ξ too weakly.

Fluctuations and correlations are well-known signatures of phase transitions. In particular, the quark/gluon to hadronic phase transition may lead to significant fluctuations [89]. Dynamical fluctuations in global conserved quantities such as baryon number, strangeness or charge may be observed near a QCD critical point.The commencing of a QCD critical point search at the RHIC has extended the reach of possible measurements of dynamical K/π, p/π and K/p ratio fluctuations from Au+Au collisions to lower energies. The STAR experiment has performed a comprehensive study of the energy dependence of these dynamical fluctuations in Au+Au collisions at the energies $\sqrt{s_{NN}}$ = 7.7, 11.5, 39, 62.4 and 200 GeV. New results are compared to previous measurements and to theoretical predictions from several models. The measured dynamical K/π fluctuations are found to be independent of collision energy, while dynamical p/π and K/p fluctuations have a negative value that increases toward zero at top RHIC energy.

The promising signals of QCP should survive not only in expanding fireball but also even after the freezeout process. Here we investigate two candidates of them: fluctuations and hadron ratios. For fluctuation, naively, we have to pick up fluctuations of conserved values such as charge, baryon number and strangeness during whole process of collisions. Hadron ratios are fixed at chemical freezeout temperature and hold the same value during freezeout process and final state interactions.

4.3.1 Event-by-Event Fluctuations

The critical point search program requires a careful choice of experimental observables and steps in μ_B for this experimentally driven approach to locate the critical point. A non-monotonic dependence of observables sensitive to critical point on $\sqrt{S_{NN}}$ and an increase of long wavelength or low momentum number fluctuations should become apparent only near the critical point. For example, the rise and then fall of this signal as μ_B increases should allow us to ascertain the (T,μ_B) coordinates of the critical point. The magnitude of these non-monotonic excursions, as well as the probability that they will survive the final state interactions, are difficult to predict. Fortunately for the experiments, there may not be a need for the evolution trajectory of the system to pass precisely through the critical point in the (T,μ_B) plane to observe the signatures, as some hydrodynamic calculations show that the critical point attracts the evolution trajectories [90]. In such a case, if the trajectory misses the critical point by a few tens of MeV along the μ_B axis, the signature will be just as strong as if it were to pass directly through it. It should be noted, however, that this attraction is not generic, and relies on specific features of the equation of state (EOS) near the critical point. Available lattice QCD calculations suggest the μ_B region of influence around critical point would be around 100 MeV [91] .

The actively pursued signatures of the critical point, the non-monotonous dependence on $\sqrt{s}$ (and thus, on μ_B) of the event-by-event fluctuation observables [92, 93], can be understood qualitatively by noting that: (1) susceptibilities diverge at the critical point, and (2) the magnitude of the fluctuations are proportional to the corresponding susceptibilities. For example, for the fluctuations of energy or

charge, the well-known relations are

$$\frac{\partial E}{\partial T} = \frac{1}{T^2}\langle(\Delta E)^2\rangle; \frac{\partial Q}{\partial \phi} = \frac{1}{T}\langle(\Delta Q)^2\rangle \tag{4.1}$$

Ideally, one could determine susceptibilities on the left-hand side by measuring the fluctuation on the right-hand side [94]. However, practically, the measurement of the corresponding fluctuations, ΔE or ΔQ, is not feasible because not all the particle end up in the detector [93, 95]. Figure 4.4 shows the behaviour of static and
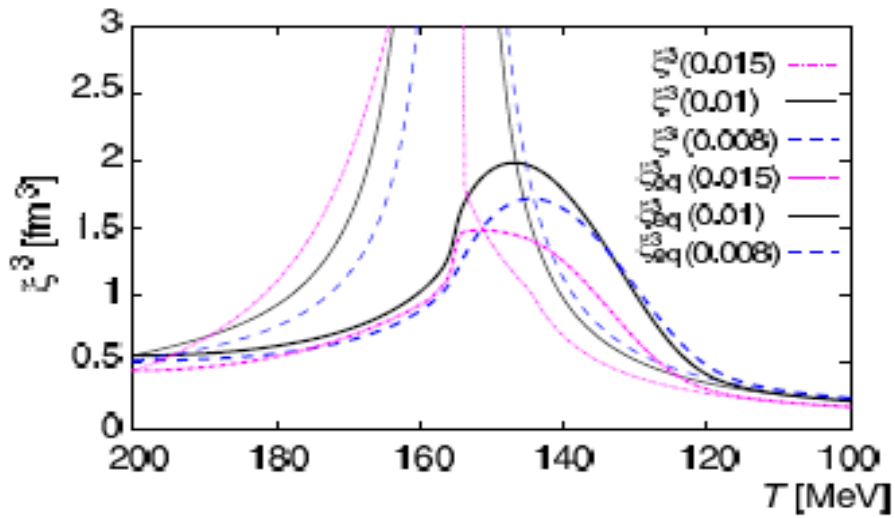
Figure 4.4: *Fluctuations as a function of temperature along isentropic trajectories.*

dynamic fluctuations in 1d hydrodynamic expansion along isentropic trajectories on the μ_B - T plane [96]. In both cases of static and dynamic fluctuations, we can see the effect of QCP, i.e enhancement of fluctuation around QCP. For static case fluctuation becomes maximum just at QCP. However for dynamic case maximum value of fluctuation appears after passing in the vicinity QCP because of the critical slowing down and the maximum value itself is not so large as the static case. There is possibility that fluctuations which are induced by QCP do not become so large as a signal of QCP, if the expansion of fireball is fast.

4.3.2 Hadron Ratios

For hadron ratios key issue from the point of view of QCD critical point is that a chemical freezeout temperature depends on transverse velocity of hadrons. Fig 4.5 shows that $\bar{p}/p$ ratio has has transverse velocity dependence in a microscopic
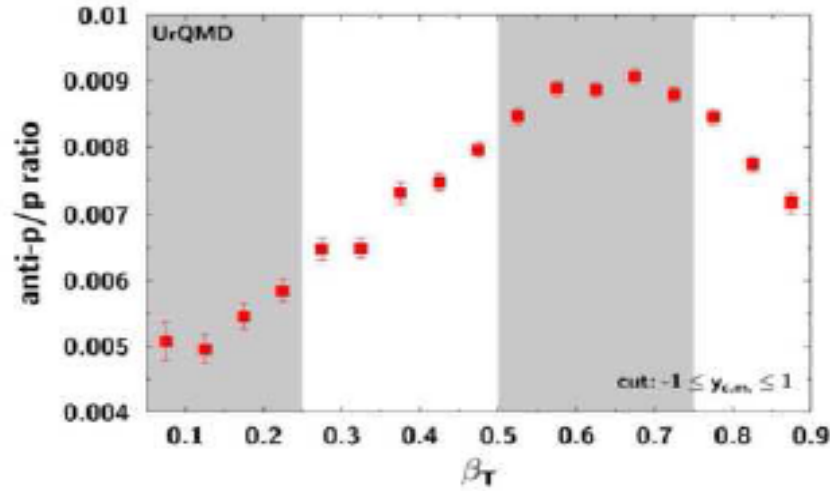
Figure 4.5: *$\bar{p}/p$ ratio as a function of transverse velocity which is obtained with UrQMD.*

transport model, UrQMD in which the QCP does not exist. It has been calculated that on isentropic trajectories the freezeout process occurs gradually [97]: particles with higher transverse velocity are produced at later time. This suggests that hadron ratios may change on isentropic trajectory between a hadronization point on the QCD phase boundary on the μ_B - T plane and chemical freezout point. The hadron ratio,especially $\bar{p}/p$ ratio as a function of transverse velocity (momentum) is sensitive to behaviour of isentropic trajectories on μ_B - T plane and may show a consequence of QCP clearly.

4.3.3 Fluctuations, correlations, and acceptance

Cumulative measures of fluctuations are often used to represent experimental results. These measures suffer an important drawback they depend on the size and shape of the acceptance window of the detector. This makes comparison of differ-

ent experiments, as well as an experiment to a theory, difficult. However, knowing certain properties of the correlator, it is possible to correct for acceptance in such comparisons.

In a thermal system, the correlation length (ξ) diverges at the critical point. ξ is related to various moments of the distribution of conserved quantities such as net-baryons, net-charge and net-strangeness. Finite size and time effects in heavy-ion collisions put constraints on the values of ξ. A theoretical calculation suggests $\xi \approx 23$ fm for heavy-ion collisions at RHIC [98]. It was recently shown [99] that higher moments of distribution of conserved quantities, measuring deviations from a Gaussian, have a sensitivity to critical point fluctuations that is better than that of variance (σ^2), due to a stronger dependence on ξ. As discussed in [99], the numerator of the skewness goes as $\xi^{4.5}$ and kurtosis (k) goes as ξ^7. In addition, crossing of the phase boundary can manifest itself by a change of sign of skewness as a function of energy density [100]. Furthermore, the lattice calculations and QCD-based models have shown that the moments of net-baryon distributions are related to the baryon number susceptibilities. The product $k\sigma^2$, related to the ratio of fourth-order to second-order susceptibilities, shows a large deviation from unity near the critical point. Due to the connection between the ratios of the susceptibilities and the high-order correlation function, one can make a direct comparison between the quantities from experiment and lattice calculations [91]. Experimentally measuring event-by-event net-baryon numbers is difficult. However, the net proton multiplicity distribution can serve as a reasonable replacement. Theoretical calculations have shown that net-proton fluctuations reflect the singularity of the charge and baryon number susceptibility as expected at the critical point [101].

Figure 4.6 shows the recent experimental results [102] on the energy dependence of $k\sigma^2$ for net-protons, compared to several model calculations that do not include a critical point. Also shown at the top of Figure 4.6 are the μ_B values corresponding to various $\sqrt{s_{NN}}$. Within the experimental statistics and kinematics range, it has not yet observed any non-monotonic beam energy dependence. The results, $k\sigma^2$, from three collision energies are consistent with unity, which could imply that the system is thermalized with a small value of correlation length. The results from non-critical point models are constant as a function of $\sqrt{s_{NN}}$ and have values between 1 and 2. The result from the thermal model is exactly unity. Within
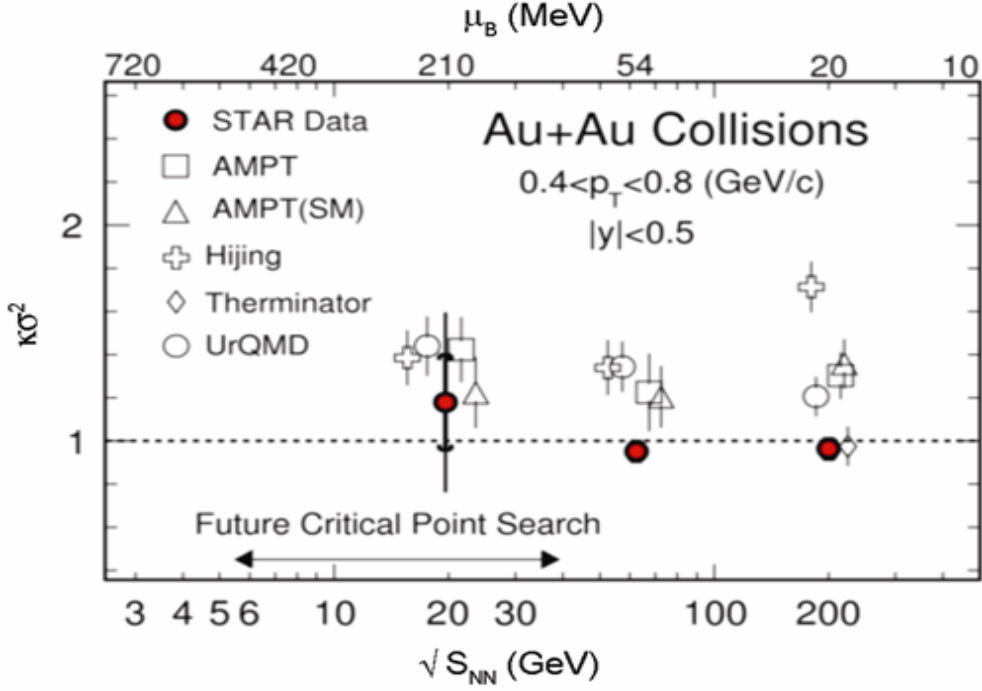
Figure 4.6: *Energy and baryon-chemical potential dependence of $k\sigma^2$ (proportional to ratio of fourth-order baryon number susceptibility to second-order baryon number susceptibility) for net-protons, compared to several model calculations that do not include a critical point. Experimental and model results are shown as filled symbols and open symbols respectively [102].*

the ambit of the models studied, the observable changes little with a change in non-critical point physics (such as collective expansion and particle production) at the various energies studied. From comparison to models and the lack of non-monotonic dependence of $k\sigma^2$ on $\sqrt{s_{NN}}$ studied, they observed that there is no indication from our measurements for a critical point. Clearly the data at RHIC during 2010 and 2011 will be crucial to bridge the gap in baryon chemical potential regions to search for the critical point in the QCD phase diagram. Lattice QCD provides predictions for these ratios. Away from the critical point, the fireball is expected to come to thermal equilibrium and the lattice results should agree with observations. Near the critical point the fireball will fall out of equilibrium because of critical slowing down [98], and hence the lattice results would not describe the

data. If a non-monotonic behaviour of the $k\sigma^2$ is seen, then it will be clear that the system has passed or is close to the critical point.

4.4 Moments Methodology

In statistics [103], moments are used to characterize the shape of a probability distribution. For example, the second central moment (moment about the mean), variance (σ^2) is widely applied to describe the width of a probability distribution. The skewness (S) and kurtosis (k) are used to describe how the distributions skewed and peaked from its mean value, respectively. Another alternative methods to the moments of a distribution is so called cumulant. The cumulants determine the moments in the sense that any two probability distributions whose cumulants are identical will have identical moments as well, and similarly the moments determine the cumulants. In heavy ion collision, the higher moments of distributions of conserved quantities, such as net-baryon, net-charge and net-strangeness, are predicted to be sensitive to the correlation length and to be connected to the thermodynamic susceptibilities computed in lattice QCD [104] and in the Hadron Resonance Gas [105] (HRG) model. As the net-proton can also reflect the net-baryon and net-charge fluctuations, higher moments of net-proton distributions are used to search for the QCD critical point.

4.4.1 Cumulants and Moments

In probability theory and statistics, the cumulants of a probability density distribution can be defined by using the cumulant-generating function [106]. The cumulant-generating function of the random variable X is defined as:

$$G(t) = log[E(e^{tX})] \tag{4.2}$$

Where the E is the expectation operator and some times denoted by angle brackets $\langle\rangle$, $E(e^{tX}) = \langle e^{tX}\rangle = \int\limits_{-\infty}^{+\infty} e^{tX} f(X) dX$, for a real-valued continuous probability density function f(x). Generally, the nth order cumulants C_n can be extracted from the cumulant-generating function via differentiation (at zero) of G(t).

$$C_n = G^{(n)}(0) = \left.\frac{\partial^n G(t)}{\partial t^n}\right|_{t=0} \tag{4.3}$$

Cumulants of a distribution are closely related to the moments of the distribution and the moment-generating function for moments about zero an be written as:

$$g(t) = E(e^{tX}) = 1 + \sum_{n=1}^{\infty} \langle X^n \rangle \frac{t^n}{n!} \tag{4.4}$$

Consequently, the nth order moments about zero $\mu'_n = \langle X^n \rangle$ can be obtained by

$$\mu'_n = \langle X^n \rangle = g^{(n)}(0) = \left. \frac{\partial^n g(t)}{\partial t^n} \right|_{t=0} \tag{4.5}$$

Thus, the cumulant-generating function can be expressed in terms of the moments about zero as:

$$G(t) = log[g(t)] = -\sum_{n=1}^{\infty} \frac{1}{n}(1 - g(t))^n = \sum_{n=1}^{\infty} \frac{1}{n}(-\sum_{m=1}^{\infty} \mu'_m \frac{t^m}{m!})^n$$

$$= \mu'_1 \times t + (\mu'_2 - \mu'^2_1) \times \frac{t^2}{2!} + (\mu'_3 - 3\mu'_2\mu'_1 + 2\mu'^3_1) \times \frac{t^3}{3!} + ... \tag{4.6}$$

Finally, we obtain the connections between the cumulants, moments about zero μ'_n and central moments (moments about mean) $\mu_n = \langle (X - \langle X \rangle)^n \rangle = \langle (\delta X)^n \rangle$:

$$C_1 = \mu'_1 = \langle X \rangle \tag{4.7}$$

$$C_2 = \mu'_2 - \mu'^2_1 = \langle (X - \langle X \rangle)^3 \rangle \tag{4.8}$$

$$C_4 = \mu'_4 - 4\mu'_3\mu'_1 - 3\mu'^2_2 + 12\mu'_2\mu'^2_1 - 6\mu'^4_1$$

$$= \langle (X - \langle X \rangle)^4 \rangle - 3 \times (\langle (X - \langle X \rangle)^2 \rangle)^2 \tag{4.9}$$

...

$$C_n = \mu'_n - \sum_{m=1}^{n-1} \binom{n-1}{m-1} C_m \mu'_{n-m}$$

$$= \mu_n - \sum_{m=1,(n-m,n\geq 2)}^{n-1} \binom{n-1}{m-1} C_m \mu_{n-m} \tag{4.10}$$

In general, we may also consider the joint cumulants, for example, the generating-function of joint cumulants for random variables, $X_1, X_2, ...X_n, (n \geq 2)$ is defined as:

$$G(t_1, t_2, ...t_n) = log\langle e^{\sum_{j=1}^{n} t_j X_j} \rangle \tag{4.11}$$

Then, the joint cumulants of random variables, $X_1, X_2, ...X_n, (n \geq 2)$ can be expressed as:

$$C(X_1, X_2, ...X_n) = \sum_{\pi} (|\pi| - 1)!(-1)^{|\pi|-1} \prod_{B \in \pi} E(\prod_{i \in B} X_i)$$

$$= \sum_{\pi} (|\pi| - 1)!(-1)^{|\pi|-1} \prod_{B \in \pi, |B| \geq 2} E(\prod_{i \in B} \delta X_i) \tag{4.12}$$

Where π runs through the list of all partitions of 1,2,...,n, runs through the list of all blocks of partitions π, $|\pi|$ is the number of parts in the partition and $|B|$ is the number of parts in the block B. For example, if we only have two random variables X,Y, then various order joint cumulants are:

$$C(X,Y) = C_{1X,1Y} = \langle \delta X \delta Y \rangle \tag{4.13}$$

$$C(X,Y,Y) = C_{1X,2Y} = \langle \delta X (\delta Y)^2 \rangle \tag{4.14}$$

$$C(X,X,Y,Y) = C_{2X,2Y} = \langle (\delta X)^2 (\delta Y)^2 \rangle$$

$$-2\langle \delta X \delta Y \rangle^2 - \langle (\delta X)^2 \rangle \langle (\delta Y)^2 \rangle \tag{4.15}$$

$$C(X,Y,Y,Y) = C_{1X,3Y} = \langle \delta X (\delta Y)^3 \rangle - 3\langle \delta X \delta Y \rangle \langle (\delta Y)^2 \rangle \tag{4.16}$$

Where the $\delta X = X - \langle X \rangle, \delta Y = Y - \langle Y \rangle$.

Usually, the central moments are more useful than the moments about zero to describe the shape of the distributions. The second central moment (variance (σ^2)) is used to describe the width of a distributions. The normalized third central moment and fourth central moment so called skewness (S) and kurtosis (k), are used to describe the asymmetry and peakness of distributions, respectively. They are defined as:
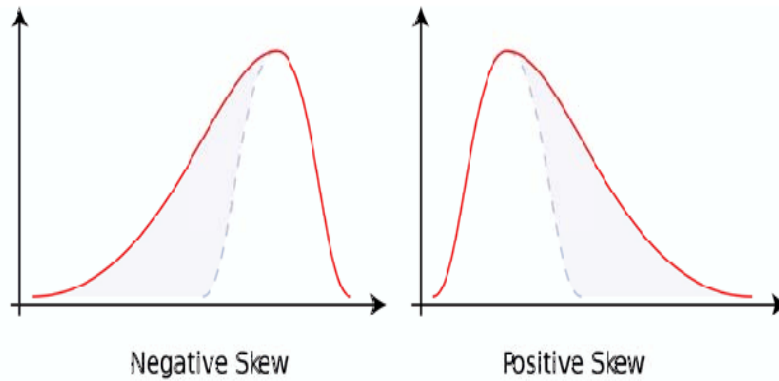
Figure 4.7: *Visual example of distribution with negative skewness (left panel) and positive skewness (right panel) [107]*

$$\sigma^2 = \langle (X - \langle X \rangle)^2 \rangle = C_2 \tag{4.17}$$

$$S = \frac{\langle (X - \langle X \rangle)^3 \rangle}{\sigma^3} = \frac{C_3}{(C_2)^{3/2}} \tag{4.18}$$

$$k = \frac{\langle (X - \langle X \rangle)^4 \rangle}{\sigma^4} - 3 = \frac{C_4}{(C_2)^2} \tag{4.19}$$

Fig 4.7 gives a visual example for determining which of the two kinds of skewness a distribution has. The distribution shown in the left panel, which gives negative skewness, is said to be left skewed. It has a longer left tail and the centre of the distribution is concentrated on the right of the distribution. The distribution in the right panel of fig 4.7 shows a distribution with positive skewness, which is said to be right skewed. It has a longer right tail and the centre of the distribution is concentrated on the left of the distribution. A zero value indicates that the values are relatively evenly distributed on both sides of the mean, typically but not necessarily implying a symmetric distribution.
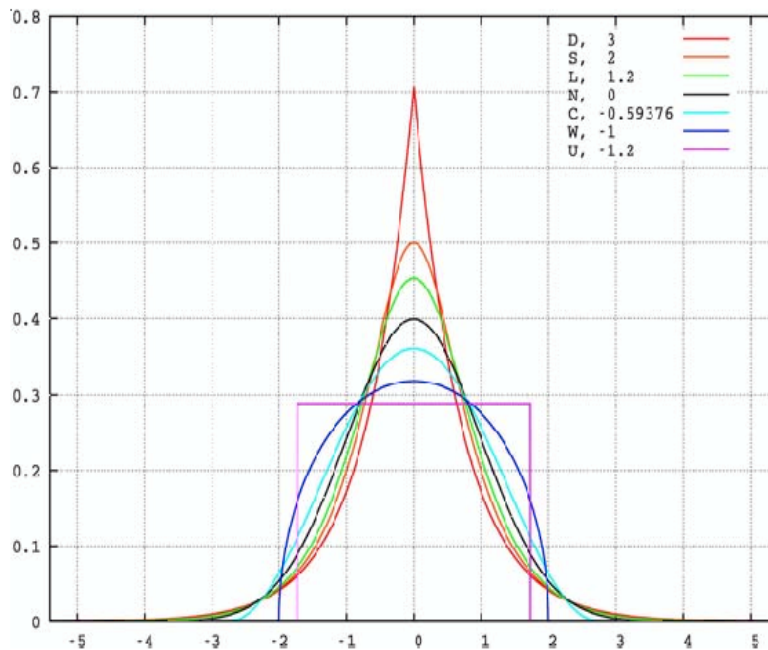
Figure 4.8: *Visual example of kurtosis for seven well-known distributions from different parametric family. The fig is taken from [108]*

Fig 4.8 shows the kurtosis of seven well-known distributions from different parametric families. All distributions here are symmetric and with unity variance and

zero mean and skewness. From top to bottom, those distributions are Laplace distribution (D), hyperbolic secant distribution (S), logistic distribution (L), normal distribution (N), raised cosine distribution (C), Wigner semicircle distribution (W) and uniform distribution (U). It is found that the distributions with a sharp peak have a larger kurtosis value than those distributions with broad tails. In fig 4.8, the kurtosis values for Laplace distribution, normal distribution and uniform distribution are 3, 0, -1.2 respectively. A high kurtosis distribution has a sharper peak and longer, fatter tails, while a low kurtosis distribution has a more rounded peak and shorter thinner tails. The kurtosis must be at least -2, which can be realized by the Bernoulli distribution with p = 1/2. There is no upper limit to the kurtosis and it may be infinite.

For normal distributions, both, the skewness and the kurtosis are equal to zero. Thus, they are ideal probes of the non-gaussian fluctuations.

4.4.2   Moments in Heavy Ion Collision

Experimentally, heavy ion collision provides us a good opportunity to search for the CP. To access the QCD phase diagram, we can tune the chemical freeze out temperature (T) and baryon chemical potential (μ_B) by varying the colliding energy. As the characteristic signatures of the CP in a static and infinite medium is the divergence of the correlation length (ξ) and increase of non-Gaussian fluctuations. Thus, non-monotonic signals of CP are expected to be observed if the evolution trajectory (T, μ_B) in the QCD phase diagram of the system pass nearby the critical region and the signals are not washed out by the expansion of the colliding system.

Due to the finite size effect, rapid expansion and critical slowing down etc., the typical correlation length (ξ) developed in the heavy ion collision near the QCD critical point is a small value about 2   3 fm [109]. Recently, model calculations reveal that higher moments of conserved quantities distributions are proportional to the higher power of the correlation length [110, 111], such as fourth order cumulant $\langle (\delta N)^4 \rangle - 3 \langle (\delta N)^2 \rangle^2 \sim \xi^7$, where $\delta N = N M$, N is the particle multiplicity in one event and M is the averaged particle multiplicity of the event sample. On the other hand, the higher moments as well as moment products of conserved quantities distributions are also directly connected to the corresponding susceptibilities in Lattice QCD [104, 112] and HRG model [105] calculations, for e.g. the third order

susceptibility of baryon number $\chi_B^{(3)}$ is related to the third cumulant ($\langle(\delta N_B)^3\rangle$) of baryon number distributions as $\chi_B^{(3)} = \langle(\delta N_B)^3\rangle/VT^3$; V, T are volume and temperature of system respectively. It has been found that the volume independence baryon number susceptibility ratio can be directly connected to the moment products of baryon number distributions as $k\sigma^2 = \chi_B^{(4)}/\chi_B^{(2)}$ and $S\sigma = \chi_B^{(3)}/\chi_B^{(2)}$, which allows us to compare the theoretical calculations with experimental measurements. Theoretical calculations also demonstrate that the experimental measurable net-proton number (proton minus anti-proton number) event-by-event fluctuations can reflect the baryon number and charge fluctuations [113]. Thus, higher moments of the net-proton multiplicity distributions are applied to search for the QCD critical point in the heavy ion collisions [114, 115, 116]. When approaching the QCD critical point, the moment products $k\sigma^2$ and $S\sigma$ will show large deviation from its Poisson statistical value. The skewness is expected to change its sign when system evolution trajectory in the phase diagram cross phase boundary [117].

In year 2010, RHIC Bean Energy Scan (BES) program [118] was carried out to map the first order QCD phase boundary and search for the QCD critical point by tuning the colliding energy from 39 GeV down to 7.7 GeV with the corresponding μ_B coverage about 100-410 MeV. With the large uniform acceptance and good capability of particle identification STAR detector, it provides us very good opportunities to find the QCD critical point with sensitive observable, if the existence of QCD critical point is true.

Experimentally, we measure particle multiplicities event-by-event wise. In the following, we use N to represent the particle number in one event. The average value over the whole event ensemble is denoted by $\langle N \rangle$, where the single angle brackets are used to indicate ensemble average of an event-by-event distributions.

The deviation of N from its mean value is defined by

$$\delta N = N - \langle N \rangle \tag{4.20}$$

Then, we can define the various order cumulants of event-by-event distributions of

a variable N.

$$C_{1,N} = \langle N \rangle \tag{4.21}$$

$$C_{2,N} = \langle (\delta N)^2 \rangle \tag{4.22}$$

$$C_{3,N} = \langle (\delta N)^3 \rangle \tag{4.23}$$

$$C_{4,N} = \langle (\delta N)^4 \rangle - 3\langle (\delta N)^2 \rangle^2 \tag{4.24}$$

Once we have the definition of cumulants, various moments can be denoted as:

$$M = C_{1,N}, \sigma^2 = C_{2,N}, S = \frac{C_{3,N}}{(C_{2,N})^{3/2}}, k = \frac{C_{4,N}}{(C_{2,N})^2} \tag{4.25}$$

And also, the moments product $k\sigma^2$ and $S\sigma$ can be expressed in terms of cumulant ratios.

$$k\sigma^2 = \frac{C_{4,N}}{C_{2,N}}, S\sigma = \frac{C_{3,N}}{C_{2,N}} \tag{4.26}$$

With above definition of various moments, we can calculate various moments and moment products with the measured event-by-event particle number fluctuations in a certain p_T and rapidity range for each centrality. Higher moments of conserved quantities, such as net-baryon, net-charge and net-strangeness number are predicted to be sensitive to the correlation length developed in heavy ion collisions and are directly linked to the thermodynamic susceptibilities computed in Lattice QCD [104] and in the Hadron Resonance Gas (HRG) [105] model. As the net proton fluctuations can also reflect the net-baryon and net-charge fluctuations in heavy ion collision [119], higher moments of net-proton distributions can be used to search for the QCD critical point.

The window in rapidity should be at least about one unit wide, in order for the results to apply without significant acceptance corrections. Furthermore, the longitudinal expansion of the matter produced in the collision reduces correlations among particles separated by much more than one unit in rapidity, making larger windows unnecessary.

4.5   Higher-order moments of the fluctuations

Most fluctuation measures discussed to-date can be related to quadratic variances of event-by-event observables, such as particle multiplicities, net charge, baryon number, particle ratios, or mean transverse momentum. In the vicinity of the QCD

critical point, these variances are proportional to the square of the correlation length which is expected to diverge at the critical point. However, the magnitude of the correlation length is limited by the system size and by finite time effects (critical slowing down), and could be as small as 2 - 3 fm. Hence, the contribution to the fluctuations from the critical point might be too weak as to be discovered experimentally, if only the second moments are measured. Therefore, it has been proposed to measure higher, non-Gaussian moments of the fluctuations which are expected to be much more sensitive to the critical point [110]. Recently, both have been suggested as possible probes for the QCD critical point in heavy-ion collision experiments. For instance, it has been suggested that, contrary to susceptibilities, third moments change their sign as the phase transition is crossed which may allow for additional information being gained from experimental data [120]. In addition, higher-order fluctuations diverge with a higher critical exponent than susceptibilities and might thus give stronger hints on the position of the CP in the phase diagram than susceptibilities [110]. As another important application, higher-order moments are often used to check whether effective theories are able to reproduce lattice calculations [121, 122]. Since lattice calculations are limited to μ = 0, higher-order moments w.r.t. μ are crucial because they allow for expansions to finite chemical potential. In this case, the focus is put on the behaviour of moments (also of even higher order) on the T-axis.

4.5.1 Third and Fourth Moments near the QCD Critical Point

It has been estimated that the third and fourth moment ("skewness" and "kurtosis") of the event-wise measured pion and proton multiplicity distribution are proportional to the $4^{th} - 5^{th} and 7^{th}$ power of the correlation length [110]. Thus if the correlation length increases only by 10% in the vicinity of the critical point, one should see an enhancement by a factor of two in the fourth order cumulant, whereas the second order cumulant, i.e. the fluctuations, would only increase by 20%.

For example, the ratio of the fourth order susceptibility (kurtosis) over the

second order susceptibility for baryon number

$$R_{4,2}^B \equiv \frac{\chi_B^{(4)}}{\chi_B^{(2)}} \tag{4.27}$$

has been determined by lattice QCD calculations with three flavors and almost physical light quark masses [60]. The result is shown in Fig. 4.9. The full line indicates the estimate for a hadron gas (labelled "HRG") at low temperatures, and the limit of non-interacting quarks at high temperatures (labelled "SB"). The peak close to the transition temperature softens considerably when going to smaller lattice spacings, i.e, from $N_\tau = 4$ to $N_\tau = 6$. The results shown in Fig 4.9 can be
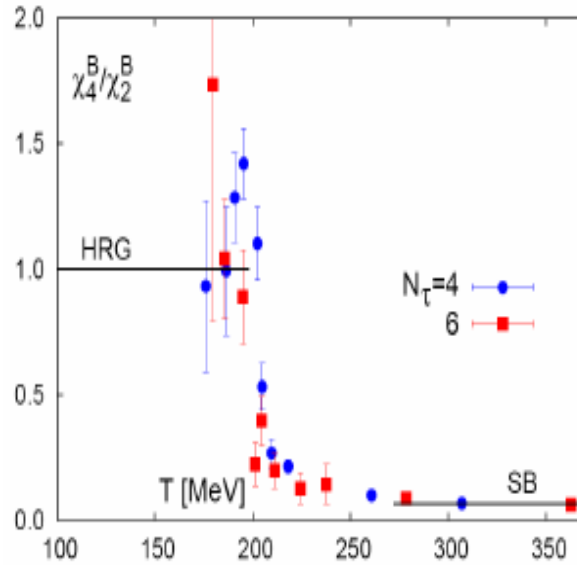
Figure 4.9: *[color online] Ratio of fourth order to second susceptibilities for baryon number. The line at low temperature, labelled "HRG" indicates the results for a hadron gas. The limit of free quarks is shown on the right and denoted by "SB" [123]*

easily understood in terms of hadrons on the low temperature side and independent quarks on the high temperature side. Consider a classical ideal gas of particles with baryon number b. Then we have

$$\chi_B^{(2)} = b^2(\chi_N^{(2)} + \chi_N^{(2)}) \tag{4.28}$$

$$\chi_B^{(4)} = b^4(\chi_N^{(4)} + \chi_N^{(4)}) \tag{4.29}$$

where $\chi_N^{(2)}$ and $\chi_N^{(2)}$ are the particle-number cumulants for particles and antiparticles, respectively.

$$\chi_N^{(2)} = \langle N^2 \rangle - \langle N \rangle^2 = \langle N \rangle \tag{4.30}$$

$$\chi_N^{(4)} = \langle N^4 \rangle - 3\langle N \rangle^2 = \langle N \rangle \tag{4.31}$$

Consequently, the ratio of the cumulants is $R_{4,2}^B = b^2$, and since all baryons in the hadronic phase have baryon number $|B_{hadronic}| = 1$ and all quarks have baryon number $|B_{quark}| = 1/3$ the final result is $R_{4,2}^B = 1$ for the hadronic phase and $R_{4,2}^B = 1/9$, for the quark-Gluon Plasma. Since baryons are fermions, one would have to correct the above result for quantum statistics. In case of massless particles this can be done analytically and one would have to multiply the results by a factor of $6/\pi^2 \simeq 0.6$. The effect of quantum statistics for the massive baryons in the hadronic phase can only be evaluated numerically and for baryons with mass M = 1GeV and a temperature of T = 170 MeV the correction is less than 1%. The results of this simple estimate are also shown in figure 4.9 as the full lines at low (hadron gas) and high (QGP) temperatures.

According to Fig 4.9 the system is well described by a gas of independent quarks above $\sim 1.5 T_c$. If the calculation with $N\tau = 6$ is indeed close to the continuum limit, then we see a rapid change from hadrons to independent quarks, both in the flavor off-diagonal susceptibilities as well as in the fourth order baryon number cumulants. This would lend theoretical support of the rather surprising finding of the so-called quark number scaling at RHIC which can be simply understood within a recombination/coalescence picture. In this picture hadrons are formed at T_c by simple phase-space coalescence, which is consistent with the rather rapid buildup of correlations around T_c seen in the lattice results for the susceptibilities.

Finally, it is important to note that non-Gaussian moments of the fluctuations like skewness and kurtosis may receive contributions from other sources like remnants of initial fluctuations, flow, and jets - to name just a few obvious contributors. The experimental challenge will be to identify and evaluate these background contributions, and to extract the genuine critical point effect.

4.6   Results from Previous Experiments

The beam energy scan program at the RHIC is aimed at discovering the QCD critical point by varying the collision energy per nuclear pair $\sqrt{s}$ and detecting non-monotonic signatures characteristic of the criticality. For example, if the critical point resides in the range of μ_B between 150 and 550 MeV, it can be discovered by varying the collision energy per nuclear pair $\sqrt{s}$ from about 27 GeV down to 5 GeV. The search for the critical point is also planned at the super proton synchrotron (SPS) at CERN, the future Facility for Antiproton and Ion Research (FAIR) at GSI, and Nuclotron-based Ion Collider Facility (NICA) in Dubna (see, e.g., [124]).

4.6.1   QCD Critical Point at SPS Energies
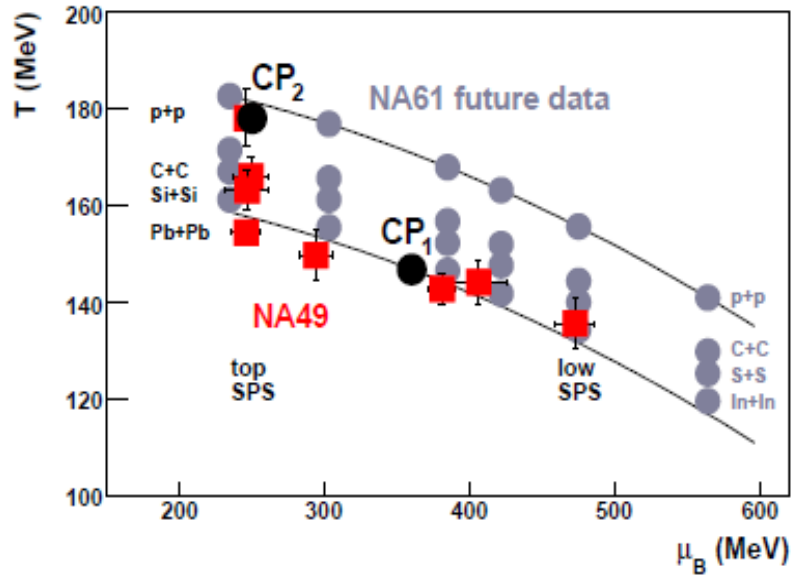
Figure 4.10: *Chemical freeze-out points in NA49 (red) and those expected in NA61 (violet). CP1 and CP2 were considered in NA49 as possible locations of the critical point: μ_B (CP1) from lattice QCD calculations [125] and CP2 assuming that the chemical freeze-out point of p+p data at 158A GeV may be located on the phase transition line.*

Theoretical calculations suggest that the critical point (CP) of strongly in-

teracting matter may be accessible in the SPS energy range [125]. They studied event-by-event average p_T and multiplicity fluctuations, as well as transverse mass spectra of baryons and anti-baryons which are suggested observables sensitive to effects of the CP in ultra-relativistic heavy ion collisions.

The effects are expected to be maximal when freeze-out happens near the critical point. The position of chemical freeze-out point in the (T μ_B) diagram can be varied by changing the energy and the size of the colliding system (Fig. 4.10). Therefore they analyzed in NA49 [126] the energy dependence of the proposed CP sensitive observables for central Pb+Pb collisions (beam energies 20A-158A GeV), and their system size dependence (p+p, C+C, Si+Si, and Pb+Pb) at the highest SPS energy.

Event-by-event average p_T and multiplicity fluctuations

Enlarged event-by-event fluctuations of multiplicity N and mean p_T were suggested as a signature of the critical point [127]. The NA49 experiment used the Φp_T correlation measure [128, 129] and the scaled variance of the multiplicity distribution ω [130, 131] to study average p_T and N fluctuations, respectively. For ω, they
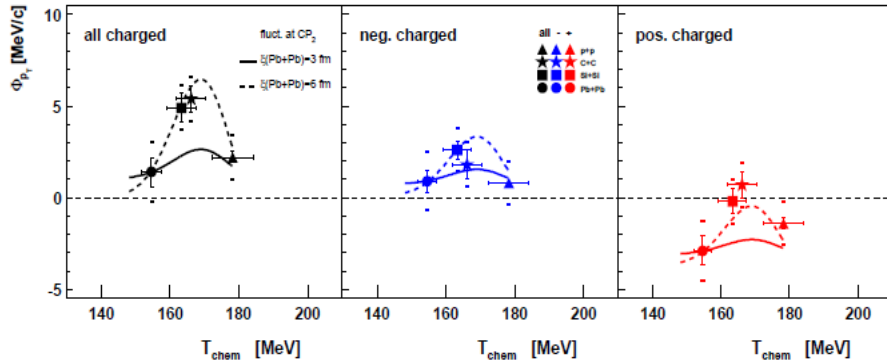
Figure 4.11: *System size dependence of Φp_T at 158A GeV (forward rapidity, NA49 azimuthal angle acceptance) showing results from p+p, semi-central C+C (15.3%) and Si+Si (12.2%), and 5% most central Pb+Pb collisions [128]. Lines correspond to CP2 predictions (see text) shifted to reproduce the Φp_T value for central Pb+Pb collisions.*

selected very central collisions only (1% most central) due to its strong dependence on fluctuations of the number of participants Npart.

The energy (μ_B) dependence of Φp_T and ω together with predictions for CP1 are discussed in [132]. The NA49 data show no significant peak in the energy dependence of Φp_T and ω at SPS energies thus providing no indications of the critical point at CP1 (see Fig 4.10).
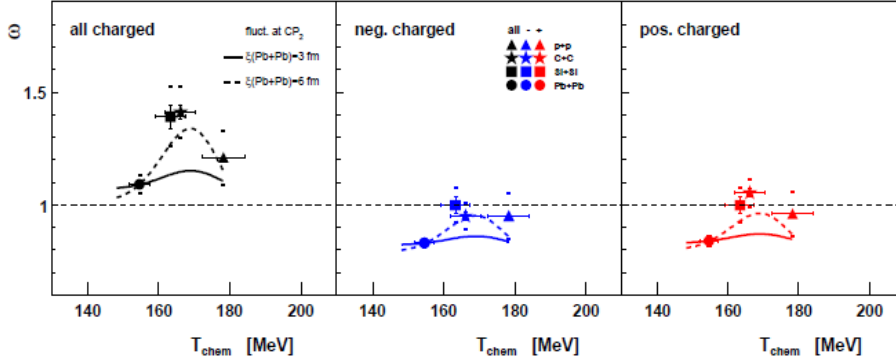
Figure 4.12: *System size dependence of ω at 158A GeV (forward rapidity, NA49 azimuthal angle acceptance) for the 1% most central p+p [130], C+C and Si+Si [134], and Pb+Pb collisions [131]. Lines correspond to CP2 predictions (see text) shifted to reproduce the ω value for central Pb+Pb collisions*

Figures 4.11 and 4.12 present the system size (Tchem [133]) dependence of Φp_T and ω. The lines correspond to predictions for CP2 (see Fig. 4.10) with estimated magnitude of the effects for Φp_T and ω at CP2 [127] assuming correlation lengths ξ decreasing monotonically with decreasing system size: (a) ξ(Pb+Pb) = 6 fm and ξ(p+p) = 2 fm (dashed lines) or (b) ξ(Pb+Pb) = 3 fm and ξ(p+p) = 1 fm (solid lines). The width of the enhancement due to CP in the (T,μ_B) plane [135] and taken as σ(T) $\approx$ 10 MeV. A maximum of Φp_T and ω is observed for C+C and Si+Si interactions at the top SPS energy. It is two times higher for all charged than for negatively charged particles, as expected for the effect of the CP [190]. Results presented in Figs. 4.11 and 4.12 suggest that the NA49 data are consistent with CP2 predictions.

It is expected that fluctuations due to the CP originate mainly from low p_T pions [127]. Therefore the NA49 analysis of Φp_T was performed also for two separate p_T regions (Fig 4.13 and 4.14). Indeed, the high p_T region shows fluctuations consistent

with zero (Fig 4.13) and correlations are observed predominantly at low p_T (Fig 4.14). However, in low p_T region, data do not show a maximum of Φp_T, but a continuous rise towards Pb+Pb collisions. The origin of this behaviour is currently being analysed (short range correlations are considered).

Transverse mass spectra of baryons and anti-baryons

It was suggested [136] that the critical point serves as an attractor of hydrodynamical trajectories in the (T, μ_B) phase diagram. This was conjectured to lead to a decrease of the anti-baryon to baryon ($\overline{B}/B$) ratio with increasing transverse momentum. The $\bar{p}/p, \overline{\Lambda}/\Lambda$, and Ξ^+/Ξ ratios versus reduced transverse mass $m_T m_0$ were studied by the NA49 experiment [132]. The slopes of all three $\overline{B}/B$ ratios show no significant energy dependence, thus implying that transverse mass spectra of B and $\overline{B}$ do not provide evidence for the critical point in the SPS energy range.
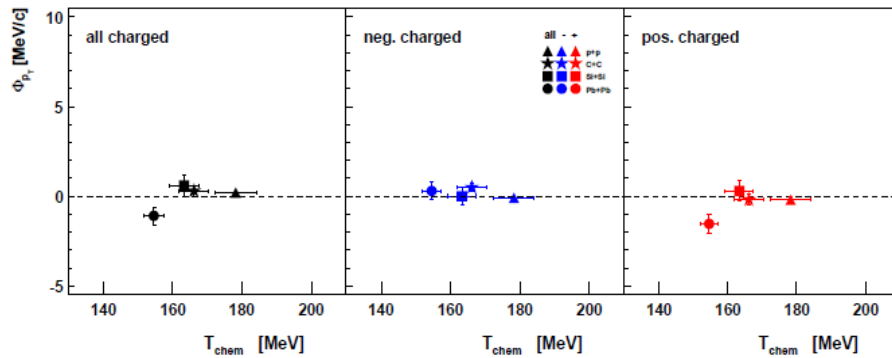
Figure 4.13: *The same as Fig 4.11 but high p_T region shown (0.5 < p_T < 1.5 GeV/c).*

The energy dependence of average p_T and multiplicity fluctuations, and ratios of the antibaryon/baryon transverse mass spectra in central Pb+Pb collisions provide no indications of the critical point. The system size dependence at 158A GeV exhibits a maximum of mean p_T and multiplicity fluctuations in the complete p_T range (consistent with CP2 predictions) and an increase (from p+p up to Pb+Pb) of mean p_T fluctuations in the low p_T region. The low p_T region will be carefully analyzed for the effects of short range correlations on Φp_T and ω.
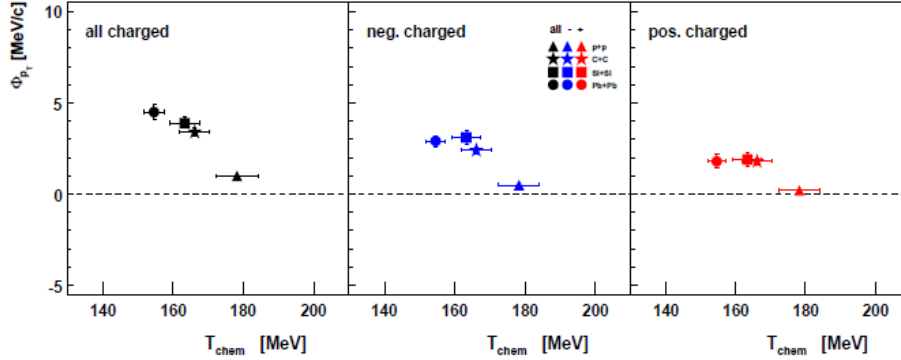
Figure 4.14: *The same as Fig 4.12 but low p_T region shown (0.005 < p_T < 0.5 GeV/c).*

4.6.2 QCD Critical Point at RHIC Energies

The experiments at RHIC have found that a strongly coupled quark-gluon plasma (sQGP) is created in heavy ion collisions at $\sqrt{S_{NN}} \sim 62$ to 200 GeV/N [137]. The observed v_2 scaling of light and multi-strange hadrons with the number of constituent quarks implies that the hot and dense matter with partonic degrees of freedom has been formed. Particularly strong evidence came from elliptic flow measurements of ϕ mesons [138]. ϕ mesons are formed via coalescence of thermalized strange quarks, and since it is believed that they do not interact in the late hadronic state, their significant elliptic flow v_2 clearly must have been developed in the partonic phase, prior to hadronization.

At RHIC energies, the baryon chemical potential μ_B extracted from the thermal model is very small (~ 0.025 GeV, [139]), so these collisions are from "above" the cross-over transition line in the phase diagram (dashed line in Fig.4.15). The lowering of the collision energy will allow one to move the freeze-out point to larger μ_B (to the right in Fig. 4.15). While stepping in μ_B, one needs to pay close attention to many observables, in particular the signatures predicted for ordered phase transition and the CP. A nonmonotonic dependence of variables on $\sqrt{S}$ and an increase of long wavelength Gaussian fluctuations should become apparent only near the critical point. The onset of the non-equilibrium "lumpy" final state is expected after cooling through a first order phase transition. Those fluctuations will have non- Gaussian character. The rise and then fall of the signal as μ_B
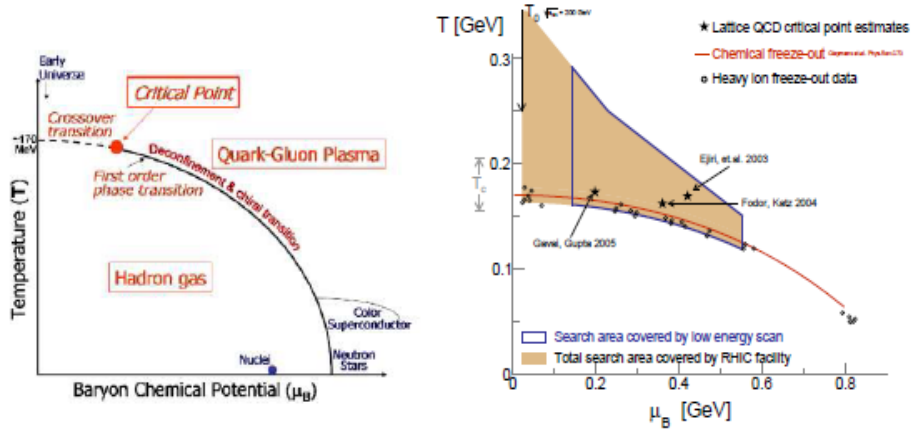
Figure 4.15: *The QCD Phase Diagram: schematic (left panel), RHIC BES program coverage of the QCD Phase Diagram (right panel).*

increases should allow one to ascertain the (T, μ_B) coordinates of the critical point (. . . if it exists).

However, the magnitude of these oscillations as well as the probability that they will survive the final state interactions is hard to predict. Fortunately for the experiments, there is no need for a trajectory to "pass" precisely through the CP in the (T, μ_B) plane to see the signatures. The hydrodynamical calculations show that the critical point "attracts" trajectories, so if the trajectory is missing the CP by 100-150 MeV along the μ_B axis, the signature will be just as strong as if it would pass directly through it. Therefore, there is no need to take very small steps in μ_B; collecting data at a few values of $\sqrt{S_{NN}}$ should be enough [140].

Beam Energy Scan at RHIC

The low energy runs at CERN SPS ($\sqrt{S} = 6.317.3$GeV) reported some interesting phenomena, possibly related to phase transition, but the evidence remains inconclusive [141].

Using the collider experiment for the energy scan studies, instead of a fixed target experiment, possesses two tremendous advantages:

(1) The phase space covered by the detectors in collider experiments changes very little with beam energy, which allows for direct comparison. At fixed target experiments, the detector acceptance changes significantly with energy and com-

parisons require extrapolation to a common phase space. This process is based on assumptions and therefore introduces additional systematic uncertainties.

(2) Track density at mid-rapidity varies very slowly with energy for collider geometry, while it increases dramatically with energy in fixed target experiments. This results in increased technical difficulties in tracking (e.g. changes in hit sharing and track merging, changes in dE/dx and momentum resolution).

4.6.3 QCD Critical Point by the Higher Moments in STAR Experiment
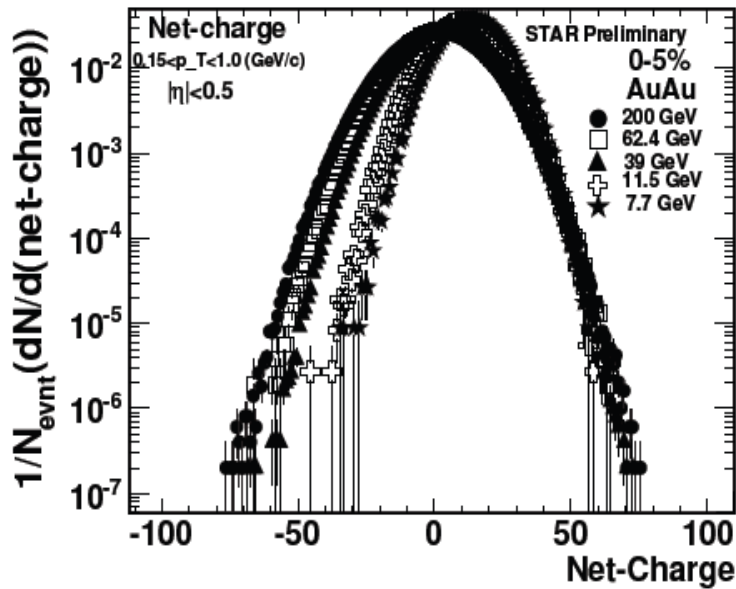
Figure 4.16: *The event normalized net-charge multiplicity distribution for 0-5% central events of Au+Au collisions at colliding energies 200 GeV (filled circle), 62.4 GeV (rectangle), 39 GeV (filled triangle), 11.5 GeV (cross) and 7.7 GeV (filled star).*

The STAR experiment provides the excellent particle identification and large acceptance for the event-by-event fluctuation analysis. The Time Projection Chamber (TPC) is the main tracking device. For the better particle identification efficiency, Time of Flight (TOF) detector is used. The TPC detector is used to identify

the charged particles within full azimuthal angle and ± 1.8 unit of pseudo-rapidity (η). For the centrality selection, uncorrected charged particles multiplicity measured within $0.5 < |\eta| < 1.0$ from the TPC is utilized to avoid auto-correlation effect in the net-charge higher moments calculation. To get the average number of participant (<Npart>) for each centrality, Glauber model calculation is done.

We report on the STAR results of the higher moments of net-charge, net-proton distribution and the products of their higher moments for Au+Au collisions at $\sqrt{s_{NN}}$ ranging from 7.7 to 200 GeV. The charged particles in low transverse momentum $0.15 < \text{pT} < 1.0 (\text{GeV/c})$ and $|\eta| < 0.5$ region are measured. Figure 4.16 shows the net-charge multiplicity distribution for the Au+Au collisions at various colliding energies. The protons and anti-protons are measured in rapidity ($|y| < 0.5$) and low transverse momentum ($0.4 < \text{pT} < 0.8$ GeV/c). The energy dependence of the 0-5% central events of the Sσ and σ^2 the net-charge multiplicity distribution are compared with the Hadron Resonance Gas (HRG) model [142], and that of the net-proton results are compared with the HRG and Lattice gauge theory calculation [143].

Chapter 5

Simulation Studies

5.1 Introduction

We need highly sensitive and specialized instruments called particle detectors to be able to study fundamental particles at a detailed level at which they can deduce their properties.Such detectors can only be designed and tuned with the help of a precise simulation system reproducing the fine details of each detector as well as the materials been used down to bolts and nuts. No data analysis or physics can be performed without the help of simulated data acting as a reference to the experimental output. All events take in to account the efficiency and acceptance correction factors. These can only be determined by comparing the experimental events to the simulated events. The associated systematic errors also include the simulation uncertainties, so that the quality of a physics result strongly depends on the quality of the physics and detector simulation involved.

A simulation package is an intrinsic part of any high-energy physics experiment in as much as the detectors themselves; it is a mandatory component of any experiment from the design stage to the final result. Simulation is the art of mimicking nature and man-made detectors.

Simulation studies are very much essential for High Energy Physics experiments which involves high degree of complexity. Simulation studies are helpful in the following ways:

1. Designing and optimizing the detectors.

2. Developing and testing the reconstruction and analysis programs, and

3. Interpretation of the experimental data.

A (computer) simulation applies mathematical methods to the analysis of complex, real-world problems and predicts what might happen depending on various actions/scenarios. we use Monte Carlo simulations because the other numerical methods typically need a mathematical description of the system (ordinary or partial differential equations) and become more and more difficult to solve as complexity increases.

5.2   Simulation

A technique which has had a great impact in many different fields of computational science is a technique called "Monte Carlo Simulation". A simulation is a fictitious representation of reality, a Monte Carlo method is a technique that can be used to solve a mathematical or statistical problem, and a Monte Carlo simulation uses repeated sampling to determine the properties of some phenomenon (or behavior).

Monte Carlo simulation is sometimes called stochastic simulation. The basic requirement of Monte Carlo simulation is to have means to generate random numbers which follow density functions typical in the physical processes in question. For example γ-spectra have peaks which can be simulated with Gaussians.

The use of Monte Carlo methods to model physical problem allow us to examine more complex systems. If we solve equation which describes the interaction between two random atoms is fairly simple but solving same equation for hundreds of atoms is difficult. With Monte Carlo methods, a large system can be sampled in a number of random configurations and that data can be used to describe the system as a whole.

In ultra-relativistic heavy ion collision, reaction dynamics is generally complex. We have to solve basically many-body system involved several hundred particles at initial stage but due to the large number of multi-particle productions, number of particles are reached to about the several thousands depending on both the incident energy and impact parameter. We may use Monte Carlo simulation to solve these many-body system.

Monte Carlo methods vary, but tend to follow a particular pattern:

1.Define a domain of possible inputs.

2.Generate inputs randomly from a probability distribution over the domain.

3.Perform a deterministic computation on the inputs.

4.Aggregate the results.

A Monte Carlo simulation uses random numbers to model some sort of a process. This technique works particularly well when the process is one where the underlying probabilities are known but the results are more difficult to determine. A great deal of the CPU time on some of the fastest computers in the world is spent performing Monte Carlo simulations because we can write down some of the fundamental laws of physics but cannot analytically solve them for problems of interest.

Random number is a number that is determined entirely by chance and whose value is not dependent upon the value of any other number. A random number is simply a particular value taken on by a random variable. Random numbers are of two types:

1.<u>Pseudo-random numbers</u>

These are the numbers that appear at random, but are obtained in a deterministic, repeatable, and predictable manner.

2.<u>True random numbers</u>

These are the numbers that are generated in non-deterministic ways. They are neither predictable nor repeatable.

Monte Carlo simulation methods do not always require truly random numbers to be useful while for some applications, such as primality testing, unpredictability is vital.Many of the most useful techniques use deterministic, pseudo-random sequences, making it easy to test and re-run simulations. The only quality usually necessary to make good simulations is for the pseudo-random sequence to appear "random enough" in a certain sense.

5.3   Detector Simulation

The simulation of a detector is one of the most important activities during its preparation as it can provide a better understanding of the detector response and how the acquired data will eventually look like.

For each recorded collision, which is called an event, the goal is to count, trace

and characterize all the different particles that were produced and fully reconstruct the process. An interaction is simulated. Particle with initial momenta and energies are generated. The propagation of all particles created in the collision is simulated through the detector. In this process, particles can decay, interact with matter or create additional particles which are then simulated through the detector as well. The total number of particles after the simulation step of a typical event is of the order of three to four times the number of particles created at the interaction. Furthermore, all hits with detector parts are recorded. If the detector produced a signal when it is exposed to a hit, the corresponding digital output is calculated and recorded. The output of this step corresponds to the output of the detector in case of an interaction of this kind with in the detector.

The combined output from all the detectors is used to identify tracks. In this process, momenta and vertices are determined. Particle identification is performed and has probabilities for several particle types as a result.

5.4 Various Software Packages For Simulation Studies

We need various software packages for simulation studies. Some of these software packages used for simulations of MUCH are as:

- GEANT
- ROOT
- CBM software framework: ROOT

5.4.1 GEANT

GEANT is a platform for "the simulation of the passage of particles through matter," using Monte Carlo methods. GEANT software packages can be used to describe complicated detector configurations. Many GEANT based simulation packages has been developed to offer central facilities for Monte Carlo studies for different experiments.

GEANT includes facilities for handling geometry, tracking, detector response, run management, visualization and user interface. For many physics simulations,

this means less time need to be spent on the low level details, and researchers can start immediately on the more important aspects of the simulation.

The GEANT program simulates the passage of elementary particles through the matter. Originally designed for the High Energy Physics experiments, it has today found applications also outside this domain in areas such as medical and biological sciences, radio-protection and astronautics.

The principal applications of GEANT in High Energy Physics are:

- the transport of particles (tracking in this manual) through an experimental setup for the simulation of detector response;

- the graphical representation of the setup and of the particle trajectories.

The two functions are combined in the interactive version of GEANT. This is very useful, since the direct observation of what happens to a particle inside the detector makes the debugging easier and may reveal possible weakness of the setup.

GEANT is an abundant set of physics models to handle the interactions of particles with matter across a very wide energy range. Data and expertise have been drawn from many sources around the world and in this respect, GEANT acts as a repository which incorporates a large part of all that is known about particle interactions.

In view of these applications, the GEANT system allows us to:

- describe an experimental setup by a structure of geometrical volumes. A MEDIUM number is assigned to each volume by the user. Different volumes may have the same medium number. A medium is defined by the so-called TRACK-ING MEDIUM parameters, which include reference to the MATERIAL filling the volume;

- accept events simulated by Monte Carlo generators;

- transport particles through the various regions of the setup, taking into account geometrical volume boundaries and physical effects according to the nature of the particles themselves, their interactions with matter and the magnetic field;

- record particle trajectories and the response of the sensitive detectors

- visualise the detectors and the particle trajectories

The program contains dummy and default user subroutines and the user has the responsibility to:

- the relevant user subroutines providing the data describing the experimental

environment;

- assemble the appropriate program segments and utilities into an executable program;

- compose the appropriate data records which control the execution of the program.

5.4.2 ROOT

The ROOT system is an object oriented framework for large scale data analysis. ROOT written in C++, contains among others, an efficient hierarchical OO database, a C++ interpreter, advanced statistical analysis (multidimensional histogramming, fitting, minimization, cluster finding algorithms) and visualization tools. The user interacts with ROOT via a graphical user interface, the command line or batch scripts. The command and scripting language is C++ (using the interpreter) and large scripts can be compiled and dynamically linked in. The OO database design has been optimized for parallel access (reading as well as writing) by multiple processes.

It is believed that ROOT is the ideal environment to introduce physicists quickly to the new world of objects and C++. With ROOT we try to provide a basic framework that offers a common set of features and tools for domains, such as data analysis, data acquisition, event reconstruction, detector simulation and event generation.

The backbone of the ROOT architecture is a layered class hierarchy with, currently, around 250 classes grouped in about 20 frameworks divided in 9 categories. This hierarchy is organised in a mostly single-rooted class library, that is, most of the classes inherit from a common base class TObject.

The complete system consists of about 450,000 lines of C++ and 80,000 lines of C code. There are about 310 classes grouped in 24 different frameworks (each represented by their own shared library).

5.4.3 CBMROOT

The CBMROOT framework is fully based on the ROOT system [144]. The user can create simulated data and/or perform analysis with the same framework. Moreover,

Geant3, Geant4 and Fluka transport engines are supported, however the user code that creates simulated data do not depend on particular Monte Carlo engine.

The framework delivers base classes which enable the user to construct their detectors and/or analysis tasks in a simple way, it also delivers some general functionality like track visualization. Moreover an interface for reading magnetic field maps is also implemented. The CBMROOT framework has may features as:

- It is fully ROOT based framework.

- **Virtual Monte Carlo**: For simulation the Virtual Monte Carlo concept was chosen [145], this concept allows performing simulations using Geant3, Geant4 or Fluka without changing the user code or geometry description. The same framework is then used for the data analysis. An Oracle database with a built-in version management is used to efficiently store the detector geometry, materials and parameters.

- Root based IO scheme (TChain, TTree etc.)

- TTask mechanism to implement different action.

- Only ROOT based services are used.

- Geometry modeller (TGeomanager) is used.

The storage of all information collected by the different sensitive detectors is done on an event by event basis (an event means in this context one interaction between one beam particle and the target). All persistent objects are serialized and stored into binary ROOT files. An interface class (CbmMCPoint) is provided to define the structured of registered hit in a detector. Each detector can then provide a more specific implementation following the CbmMCPoint API. All registered hits will be collected into dedicated lists, one list corresponding to one detector entity. The ROOT class TTree is used to organize the output data into a "ntuple like" data structure. In the analysis case, the CbmRootManager provides methods to read this information. A partial input/output mechanism is also supported.

5.5   Event Generator

Several different models have to be included in the event generator, either to describe the reactions which are under study, or a number of background channels [146]. Event generators provide simulated events that are as close as possible to

the real interactions as that occurs at the collision point, limited by the present understanding of the underlying physics. Event generators combine perturbative solutions for well-understood areas and phenomenological approaches for other areas that can yet only be modelled. Generated events are used to obtain an understanding of the data and signals that are to be expected, for preparing the analysis strategies and implementing the needed analysis code, as well as for estimating the needed corrections to obtain from the raw measured result, the underlying true signal. In addition, results of event generators together with further simulation software are used to plan and optimize the detector design. Ultimately, although only to a limited extent, comparing results from event generators to events measured in an experiment allows the underlying physics to be understood.

5.5.1 The UrQMD Model

The Ultra Relativistic Quantum Molecular Dynamics (UrQMD) model is a transport model for simulating heavy ion collisions in the energy range from SIS energy ($\sqrt{s} \approx 2GeV$) to the RHIC energy ($\sqrt{s} = 200GeV$). The UrQMD-model [147] is a microscopic transport theory based on the covariant propagation of all hadrons on classical trajectories in combination with stochastic binary scatterings, color string formation and resonance decay.At the highest energies, a huge number of different particle species can be produced. The model should allow for subsequent rescatterings. The collision term in the UrQMD model includes more than fifty baryon species and five meson nonetts (45 mesons).It simulates multiple interaction of on-going and newly produced particles,the excitation and fragmentation of color strings formation and decay of hadronic resonances. Towards higher energies, the treatment of sub- hadronic degrees of freedom is of major importance. In this model, the degrees of freedom enter via the introduction of a formation time for hadrons produced in the fragmentation of strings [148, 149, 150] and by hard scattering via the PYTHIA [151] model.

The UrQMD model reproduces nicely the total, elastic and inelastic cross-sections of numerous hadronic reactions. The model also predicts the particle multiplicities (i.e. the inclusive cross-sections) as well as the (Lorentz-invariant) cross-sections, which may come in the form of rapidity, or transverse momentum distributions. The UrQMD model reproduces the cross-sections and spectra of par-

ticles in hadronic collisions fairly well. Since hadronic interactions build up the basic input to simulate the hadron-nucleus and nucleus-nucleus interactions in the model, it is interesting to examine the applicability of the UrQMD model to these reactions.

The main goals of UrQMD model are to gain understanding about the following physical phenomena within a single transport model:

- Creation of dense hadronic matter at high temperatures.
- Properties of nuclear matter, Delta & Resonance matter.
- Creation of mesonic matter and of anti-matter.
- Creation and transport of rare particles in hadronic matter.
- Creation, modification and destruction of strangeness in matter.
- Emission of electromagnetic probes.

Furthermore, the UrQMD model has also been used as a component of various hybrid transport approaches.

5.5.2   The Pluto Model

The software structure of the Pluto event generator [152] originally developed for the HADES experiment [153] but successfully used by other collaborations in the hadronic physics field as well.Pluto is a collection of C++ classes, adding up to the framework of a simulation package for hadronic physics interactions in the energy regime up to a few GeV. It is launched interactively within the ROOT [154] environment, and makes use of ROOT only, without requiring additional packages. The focus is on streamlining particle generators by providing the tools to set up and manipulate particles, reaction channels, and complex reactions, as well as applying experimental filters on the reaction products, such as geometrical acceptance and kinematical conditions. Typical simulations may be executed with a few lines of input, with no expertise required on the part of the user. It standardizes simulations by providing a common platform that is accessible via the analysis environment (ROOT), with a straightforward user interface that does not inhibit non-experts in simulations. via the analysis environment (ROOT), with a straightforward user interface that does not inhibit non-experts in simulations.

The output may be analyzed on line, or further forwarded to a digitization package. The Pluto framework includes models for hadronic and electromagnetic decays,

resonance spectral functions with mass-dependent widths, and anisotropic angular distributions for selected channels. A decay-manager interface enables "cocktail" calculations. An extensive particle data base is available, with capabilities to support user-defined ones. Various particle properties and decay modes are included in the data base. Thermal distributions are implemented, enabling multi-hadron decays of hot fireballs.

The general philosophy of Pluto is that on one hand the users should be able to drive the package in a very easy way, but on the other hand are allowed to customize it without much restrictions. This means that the steering application has the opportunity to add new decays/particles among with new models up to the incorporation of plugins.

The package "Pluto" [155, 156] is geared towards elementary hadronic as well as heavy-ion induced reactions at intermediate to moderately high energies, mainly motivated by the physics program of the HADES [157] experiment, which is installed at the SIS synchrotron of the GSI. As the HADES experiment has published the first data and successfully finished various experimental runs, the need for realistic and detailed simulations is evident and growing. Pluto is an available, standardized and efficient tool that facilitates such simulations. Moreover, it can be adapted and integrated into simulation environments for other experiments. In particular it has been used for the simulations in the context of the planned CBM experiment [158] which is going to be operated at the new FAIR facility.

Starting from the basic philosophy, that an event generator has to fulfil different tasks during the life-time of an experiment, the Pluto framework was designed to have a standard user-interface allowing for quick studies, but can be changed on the other hand in such a way to include sophisticated new models, including coupled channel approaches as well as interferences between various channels.

5.5.3 The HSD Model

The Hadron-String Dynamics (HSD) transport approach is a covariant microscopic transport model developed to simulate

- relativistic heavy-ion collisions
- proton-nucleus reactions
- pion-nucleus reactions

in the energy range from SIS to RHIC [160].

The HSD transport approach provides the numerical test particle solution of a coupled set of relativistic transport equations for particles with in-medium self energies (optionally). It is based on quark, diquark, string and hadronic degrees of freedom. High energy inelastic hadron-hadron collisions in HSD are described in FRITIOF 7.02 string model (including PYTHIA and JETSET) [159] whereas low energy hadron-hadron collisions are modeled based on experimental cross sections. The transport approach is matched to reproduce the nucleon-nucleon, meson-nucleon and meson-meson cross section data [161] in a wide kinematic range. HSD takes into account the formation and multiple rescattering of leading pre-hadrons and hadrons with cross sections in line with the additive quark model.

High-energy inelastic hadron-hadron collisions in HSD are described by the FRITIOF string model [163] (including PYTHIA [164]) whereas low energy hadron-hadron collisions are modelled on the basis of experimental cross sections (when available) or OBE calculations whenever no data exist. Optionally multi-meson fusion channels for baryon-antibaryon production can be included as well as the off-shell propagation of particles [165]. The major aim of HSD is - within a single transport model - to gain an understanding about the nuclear dynamics, the creation of dense and hot hadronic matter[162] and the modification of hadron properties in a medium.

More recently an extended version of HSD was developed which is denoted as PHSD (Parton-Hadron-String Dynamics) [166]. Additionally it includes an early partonic phase. Here the equation-of-state is taken from lattice QCD and the quasi-particle properties for quarks, antiquarks and gluons are obtained from fits to lattice results [167, 168]. Due to the large damping width of the partonic degrees of freedom an off-shell propagation is implemented by default. Partonic elastic and inelastic reactions are included ($qq \longleftrightarrow qq, q\bar{q} \longleftrightarrow q\bar{q}, gg \longleftrightarrow gg, gg \longleftrightarrow g, q\bar{q} \longleftrightarrow g$ etc.) with non-perturbative cross sections taken from [167] or of Breit-Wigner form which are fixed by the quasiparticle spectral functions. The transition from partonic degrees of freedom to hadronic resonant states is performed with the help of transition matrix elements that strongly peak at an energy density of about 1 GeV/fm^3. In all reactions 'detailed balance' is implemented in the partonic sector an energy-momentum conservation strictly holds in the parton-hadron transition.

Furthermore, the conservation of flavor currents is exactly fulfilled. The PHSD approach is presently tested in a wide dynamical regime up to LHC energies.

5.6   Reconstruction

The reconstruction starts from digits, which can either be in ROOT tree format or in raw data format. The first step consists in the local reconstruction performed by each single detector module: the data corresponding to each detector are elaborated by specific algorithms in order to clusterize the signals and to define the space points. Once these operations have been performed by all the selected detectors for which the local reconstruction feature is available, the tracking is carried on. It consists of fitting the space points, reconstruction vertices and tracks and identifying the particles.

5.6.1   Track Reconstruction

MUCH track reconstruction in CBM is based on track following using reconstructed tracks in the STS as seeds. In the STS track reconstruction is based on the cellular automation method [169] and STS track parameters are used as starting point for the following track prolongation. This track following is based on the standard Kalman Filter Technique [170] and is used for the estimation of track parameters [171] and trajectory recognition.

Track Propagation

The Track propagation algorithm estimates the trajectory and its errors in a covariance matrix while taking into account three physics effects which influence the trajectory, i.e, energy loss, multiple scattering and the influence of the magnetic field. A detailed description of the developed track propagation can be found in [172, 173].

Track Finding

In the track finding algorithm tracks are prolongated subsequently from one detector station to the next adding additional hits in each detector. For the attachment of hits a validation gate is calculated, according to the chosen probability for rejecting the correct hit. The nearest neighbour approach is used to choose the hit to be assigned to a track, i.e the algorithm attaches the nearest hit if lying in the

validation region at all. After the hit is attached, track parameters are updated with the Kalman Filter.

<u>Track Selection</u>

After track finding, so-called clone tracks (consisting of a very similar set of hits) and ghost tracks (consisting of a set of hits from different tracks) have to be rejected while keeping correctly found tracks with high efficiency. The selection algorithm works in two steps. First, tracks are sorted by their quality which is defined by the track length and χ^2. Then, starting from the highest quality tracks all hits belonging to a track are checked. In particular, the number of hits shared with other tracks is calculated and the track is rejected if more than 15% of the hits are shared.

5.6.2 Event Reconstruction

The CBM experimental setup has to fulfil the following requirements: identification of electrons which requires a pion suppression factor of the order of 10^5, identification of hadrons with large acceptance, determination of the primary and secondary vertices (accuracy $\sim 30\mu$m), high granularity of the detectors, fast detector response and read-out, very small detector dead time, high-speed trigger and data acquisition, radiation hard detectors and electronics, tolerance towards delta-electrons.

Event reconstruction quality tools were considerably improved. The developed routines allow one to calculate tracking performance in STS, TRD, MUCH, TOF detectors as well as global tracking performance, ring reconstruction efficiency in RICH detector, electron identification and pion suppression performance and other useful quality values.

Simulation of the experiment requires to perform a lot of systematic and detector optimization studies. In order to improve and speedup such studies, the developed routines were extended to be able to generate a summery report out of many different simulation results.

The CBM setup is optimized for heavy-ion collisions in the beam energy range from about 8 to 45 AGeV. The typical central Au-Au collision in the CBM experiment will produce up to 700 tracks in the inner track (see fig 5.1). Large track multiplicities together with the presence of non-homogeneous magnetic field make
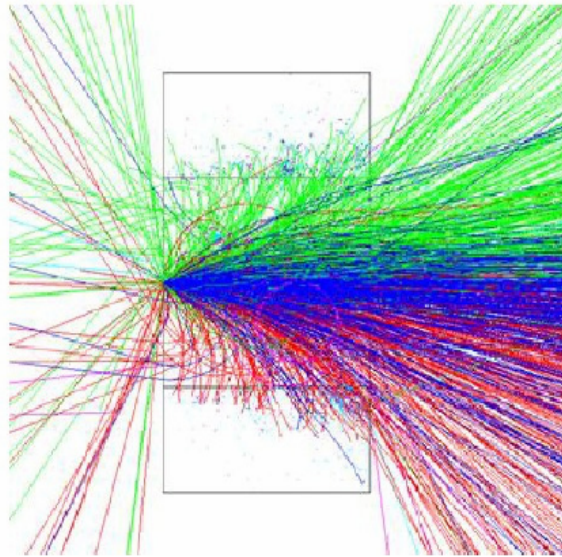
Figure 5.1: *Visualization of a typical CBM event.*

the reconstruction of events extremely complicated. It comprises local tracks finding and fitting in the STS and TRD, ring finding in RICH, cluster reconstruction in ECAL, global matching between STS, RICH, TRD ,TOF and ECAL, and the reconstruction of primary and secondary vertices. Therefore, the collaboration performs the extensive analysis of different event recognition and recognition methods, in order to better understand the geometry of detectors and to investigate specific features of useful events [174]

Chapter 6

Analysis and Results

6.1 Introduction

The preliminary analysis has to be carried out in order to study the QCD Critical Point at FAIR energies and also to optimize the detector design of MUCH in CBM experiment at FAIR energies. In this chapter, we have calculated the multiplicity distribution of particles at different FAIR energies say 8 GeV, 10 GeV and 25 GeV and also at different first absorber thickness of MUCH detector for central Au - Au collisions. Since many efforts have been made by theorist and experimentalist to search for the Critical Point, its exact location or even the existence is still not confirmed yet [175].

Experimentally, heavy ion collision provides us a good opportunity to search for the critical point. To access the QCD phase diagram, we can tune the chemical freeze out temperature (T) and baryon chemical potential (μ_B) by varying the colliding energy. It has been suggested that in the vicinity of the QCD Critical Point, the most possible probes are the fluctuations, which can be measured as the particle multiplicities, particle ratios, or mean transverse momentum as well as the fluctuations of the conserved quantities like net charge, baryon number and strangeness.

we have calculated the multiplicity fluctuations of particles, fluctuations of recorded hit distribution of particles on first absorber detector of MUCH in CBM experiment by optimizing detector design with reduced geometry and the fluctua-

tions on charge for central Au-Au collisions with the impact parameter, b = 0 on 8 GeV, 10 GeV, and 25 GeV.

6.2   Simulation Tools

The tools used for analysis is categorized into the following parts as:

1. Various software packages as FairSoft july'09 version [176], ROOT DEC'09 version of cbmroot [177] and the GEANT3 transport code.

2. Different event generators as

(a) PLUTO for generating the signal (J/ψ) mesons and

(b) UrQMD for generating the background particles.

The PLUTO event generator model will generate the signal particles such as the J/ψ particles and the low mass vector mesons as ρ, ω and ϕ mesons decaying into di-muons with multiplicities taken from the HSD model. And the UrQMD model will generate the background particles for muons consists mainly of weak decays of charged pions and kaons for central Au - Au collisions.

6.3   Results

6.3.1   Multiplicity of particles at different energies

For analysis,we have used the STS detector of 8 stations positioned at 30, 35, 40, 50, 60, 75, 90, and 100 cm from the target made of 250 μm thick gold plate and the MUCH detector of 6 stations positioned at 20, 20, 20, 30, 35 and 100 cm as shown in

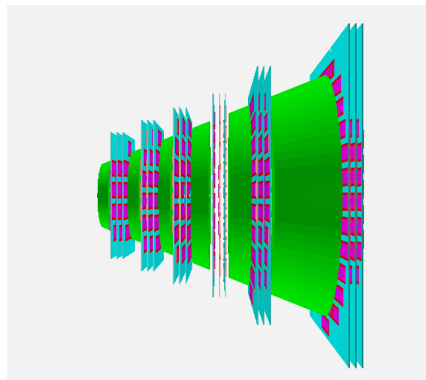Figure 6.1: *Standard geometry of MUCH with 6 stations and 6 absorbers*

Particles	25 GeV	10 GeV	8 GeV
μ^+	6302	4005	3337
μ^-	4978	3198	2667
e^+	176616	86017	67872
e^-	312614	152159	120743
p	124874	108049	100432
n	0	0	0
k^+	12808	7800	6421
k^-	3301	1252	927
Σ^+	24	13	5
Σ^-	50	16	11
π^+	90567	47216	37714
π^-	97037	52902	42737

Table 6.1: *Multiplicity of particles at 25 GeV, 10 GeV, and 8 GeV.*

fig 6.1. We generated the signal (J/ψ) particles for 1000 events from PLUTO event generator and the background particles for 1000 events from UrQMD model at different energies 8 GeV, 10 GeV, and 25 GeV and then merge the signal particles and background particles for embedded events. Then we calculated the particle wise multiplicities on first MUCH absorber at different energies of 8 GeV, 10 GeV, and 25 GeV as shown in table 6.1.

From the table 6.1, it is said that their is the fluctuations of particles at different energies which give us the indication that their must exist the critical point somewhere in the QCD phase diagram at low temperature and high baryon chemical potential.

6.3.2 Multiplicity of particles at different first absorber thickness

Here we have calculated the multiplicity of particles at different first absorber thickness's by using the STS detector of 8 stations and the reduced MUCH geometry

of 3 absorbers positioned at 20, 70 and 135 cm and 3 stations with 9 layers and the pad size of 0.4/0.4 mm, 0.5/0.5 mm, 0.6/0.6 mm respectively as shown in fig 6.2. we again generated the signal (J/ψ) particles for 1000 events from PLUTO
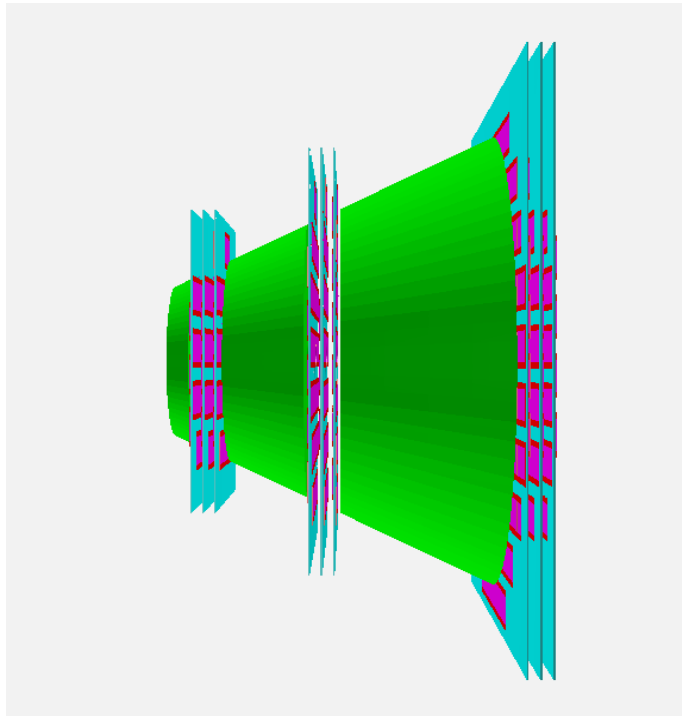

Figure 6.2: *Reduced MUCH geometry with 3 stations and 3 absorbers*

event generator and background particles for 1000 events from UrQMD model for central Au - Au collisions of 25 GeV, but with the reduced geometry shown in fig 6.2 separately on different first absorber thickness of 20, 10, and 5 cm. Then we calculate the particle multiplicities on different first absorber thickness of MUCH detector as shown in table 6.2

Particles	20 cm	10 cm	5 cm
μ^+	6131	7749	8347
μ^-	4754	6358	6973
e^+	194579	405758	471821
e^-	348799	645490	678228
p	124353	185248	203411
n	0	0	0
k^+	12579	17719	20403
k^-	3281	5514	6933
Σ^+	49	12	13
Σ^-	63	47	46
π^+	89343	154706	187166
π^-	95889	169432	210030

Table 6.2: *Multiplicity of particles at different first absorber thickness of 20, 10, and 5 cm.*

From the table 6.2, we again see that their is the multiplicity fluctuations of particles which are recorded at different first absorber thickness of MUCH detector for central Au - Au collisions at 25 GeV. Here, we see that the multiplicity of particles goes on increasing as the thickness of first MUCH absorber is reduced from 20 cm, 10 cm and 5 cm.

6.3.3   Hit distributions on MUCH

Here we again generated the signal and background particles for 1000 events with the reduced geometry of MUCH with 3 stations and 3 absorbers and calculated the hit distribution of particles at each station and each layer are shown in figures below. On this comparison of these hit distribution of MUCH   detector, we again
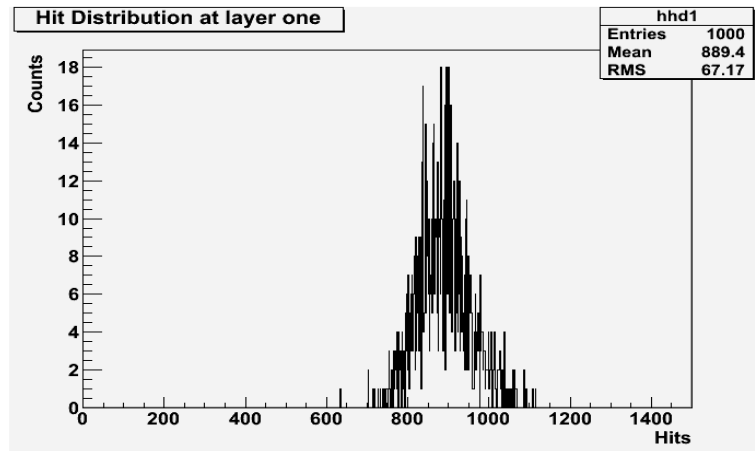
Figure 6.3: *Hit distribution on first layer of MUCH detector (station first) for central Au - Au collisions at 25 GeV.*
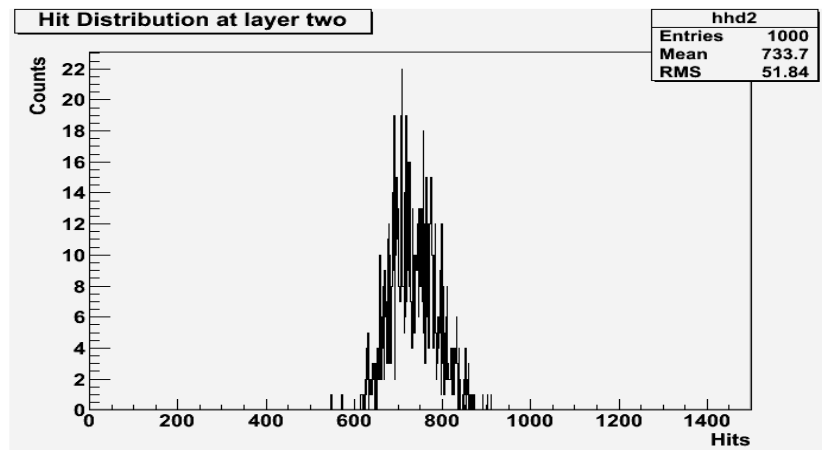

Figure 6.4: *Hit distribution on second layer of MUCH detector (station first) for central Au - Au collisions at 25 GeV.*
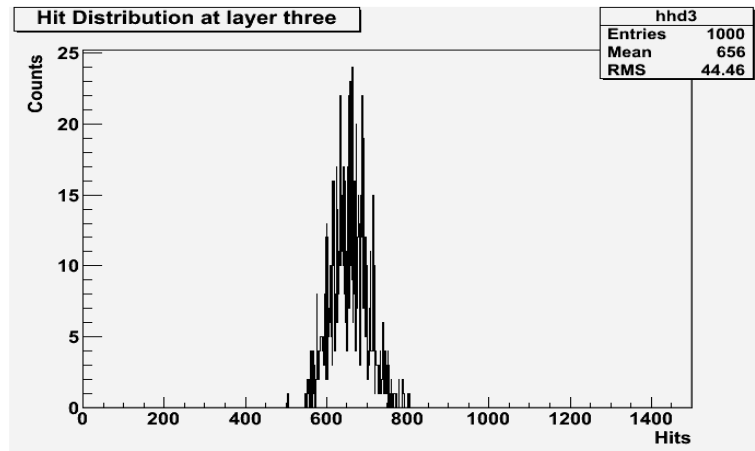
Figure 6.5: *Hit distribution on third layer of MUCH detector (station first) for central Au - Au collisions at 25 GeV.*
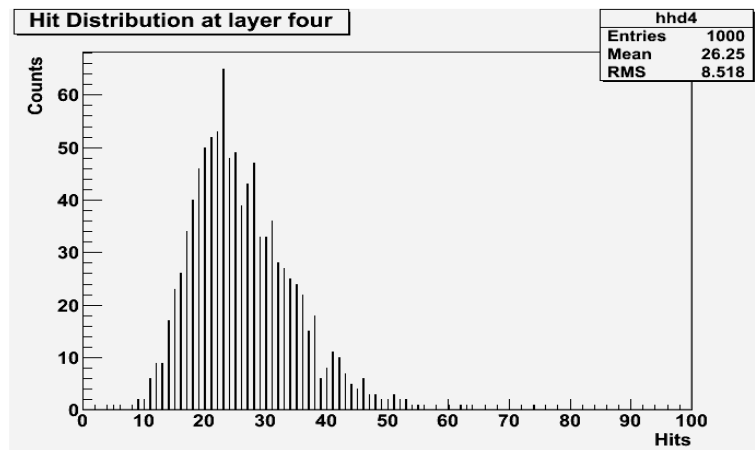

Figure 6.6: *Hit distribution on fourth layer of MUCH detector (station second) for central Au - Au collisions at 25 GeV.*
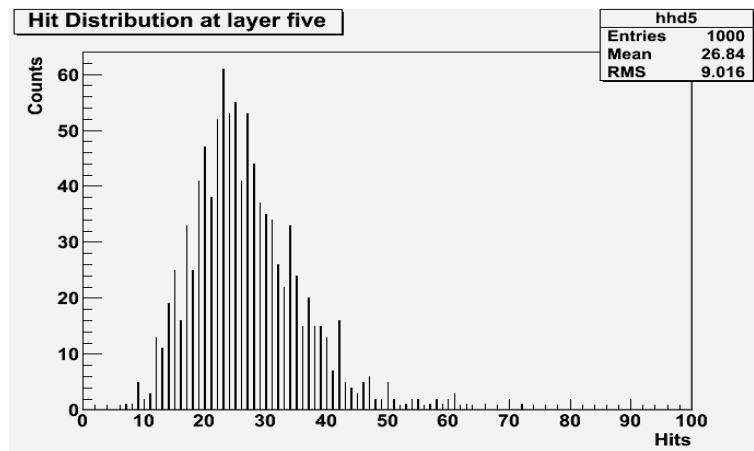
Figure 6.7: *Hit distribution on fifth layer of MUCH detector (station second) for central Au - Au collisions at 25 GeV.*
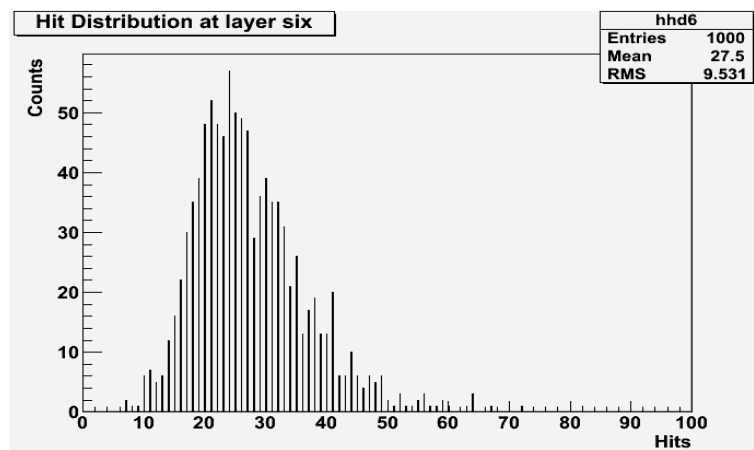

Figure 6.8: *Hit distribution on sixth layer of MUCH detector (station second) for central Au - Au collisions at 25 GeV.*
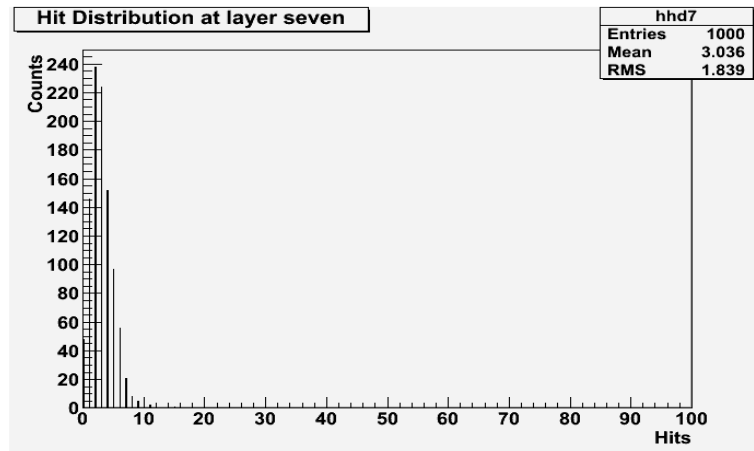
Figure 6.9: *Hit distribution on seventh layer of MUCH detector (station third) for central Au - Au collisions at 25 GeV.*
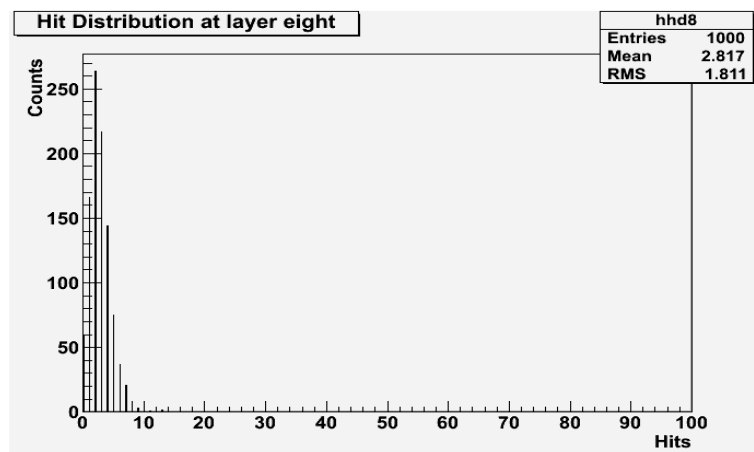

Figure 6.10: *Hit distribution on eighth layer of MUCH detector (station third) for central Au - Au collisions at 25 GeV.*
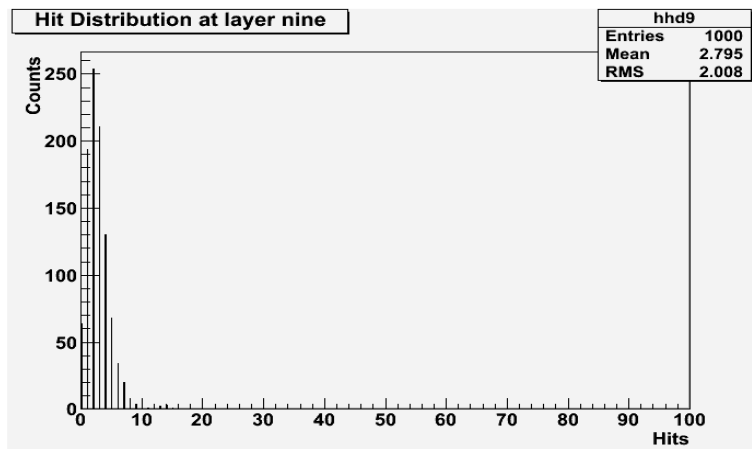
Figure 6.11: *Hit distribution on ninth layer of MUCH detector (station third) for central Au - Au collisions at 25 GeV.*

see that there is the slight variation in the hits in each layer in each station but large variation in the hits in different stations. This large variation in the hits in second and third station as compared to the first station is due to the big absorbers of 70 and 135 cm in between them, which is expected that only high p_T particles will reach the last station of MUCH detector.

From this comparison, we also say that their is the fluctuation of particles as the mean varies from first, second and third stations. Since the critical point is expected to occur at the end of the first order phase transition line which is associated with the latent heat, while the cross-over suggests a continuous change in thermodynamic variables. Therefore, the first order phase transition are expected to lead to large fluctuations due to the formation of droplets or more generally density or temperature fluctuations.

6.3.4   Charge fluctuations

We measured the charged particle multiplicity fluctuations for central Au - Au collision on MUCH detector at FAIR energies of 8 GeV, 10 GeV, and 25 GeV and then compared the results.

Figure 6.12: *Charge particle multiplicity fluctuations (all charged particles) for central Au - Au collisions at 8 GeV.*

Figure 6.13: *Charge particle multiplicity fluctuations (positively charged particles) for central Au - Au collisions at 8 GeV.*

Figure 6.14: *Charge particle multiplicity fluctuations (negatively charged particles) for central Au - Au collisions at 8 GeV.*
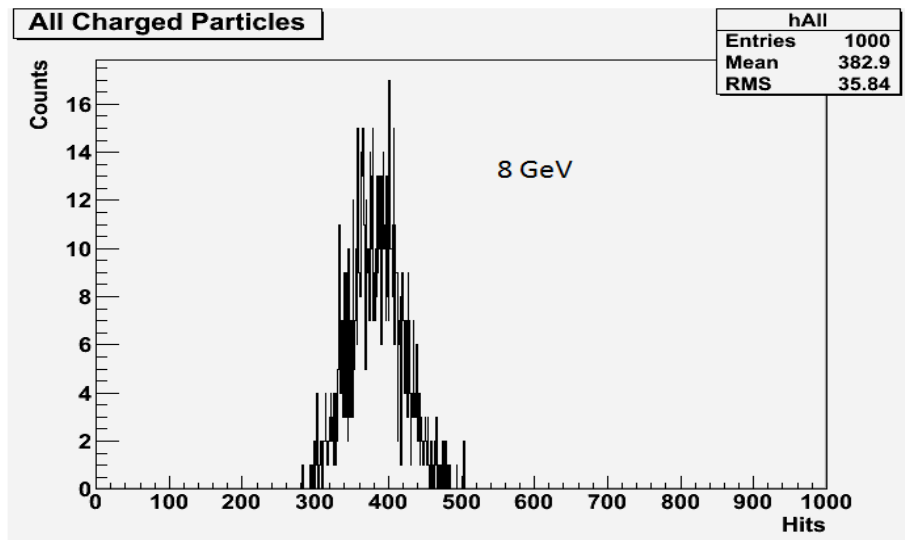
Figure 6.15: *Charge particle multiplicity fluctuations (all charged particles) for central Au - Au collisions at 10 GeV.*
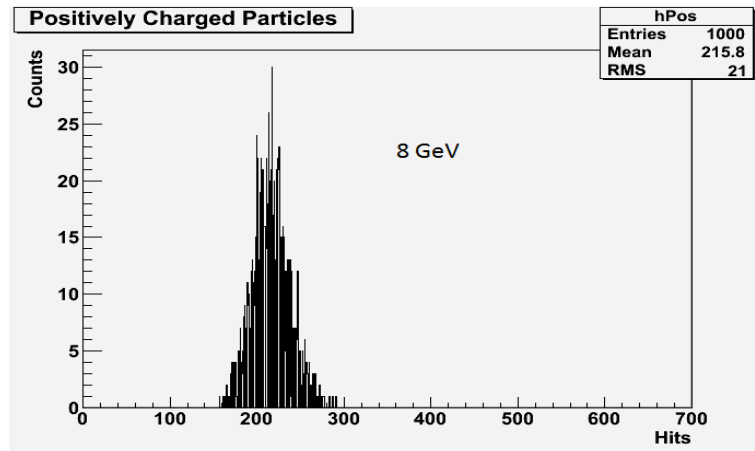
Figure 6.16: *Charge particle multiplicity fluctuations (positively charged particles) for central Au - Au collisions at 10 GeV.*

Figure 6.17: *Charge particle multiplicity fluctuations (negatively charged particles) for central Au - Au collisions at 10 GeV.*

Figure 6.18: *Charge particle multiplicity fluctuations (all charged particles) for central Au - Au collisions at 25 GeV.*

Figure 6.19: *Charge particle multiplicity fluctuations (positively charged particles) for central Au - Au collisions at 25 GeV.*
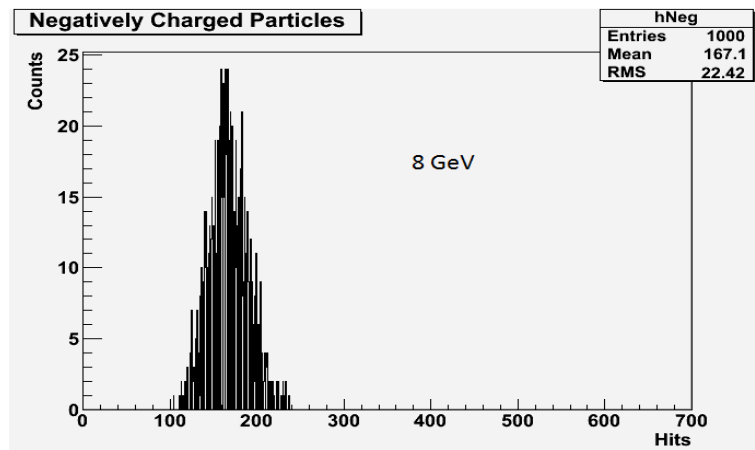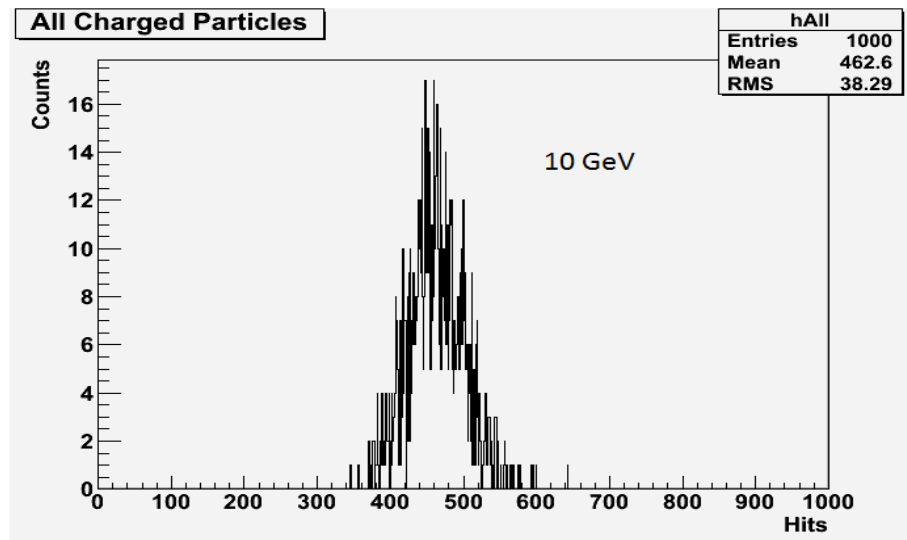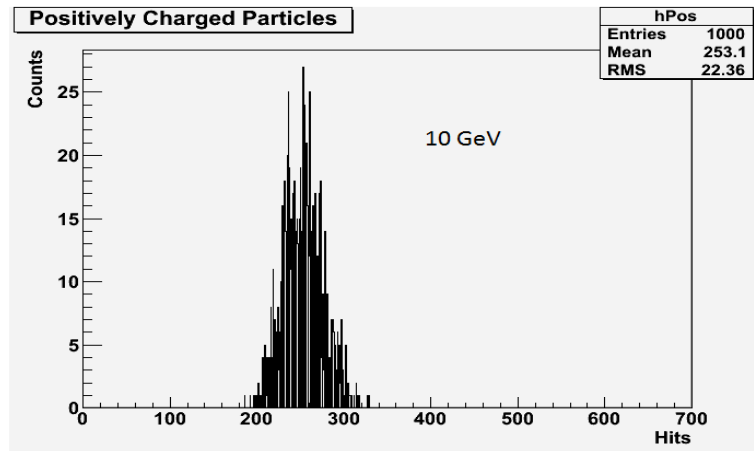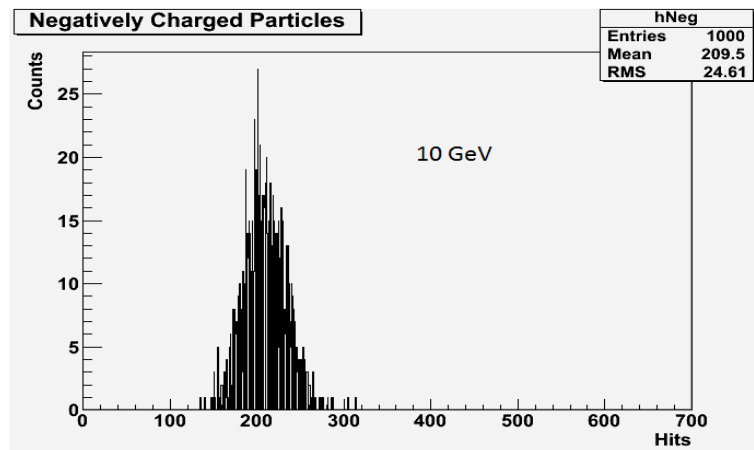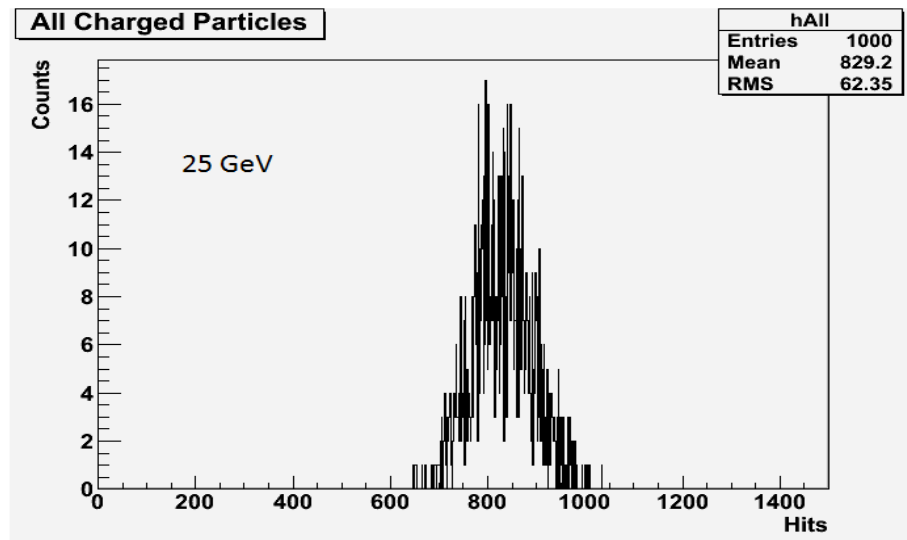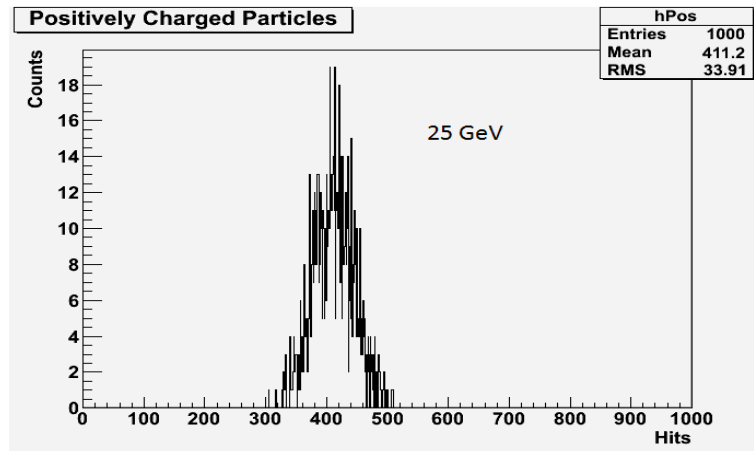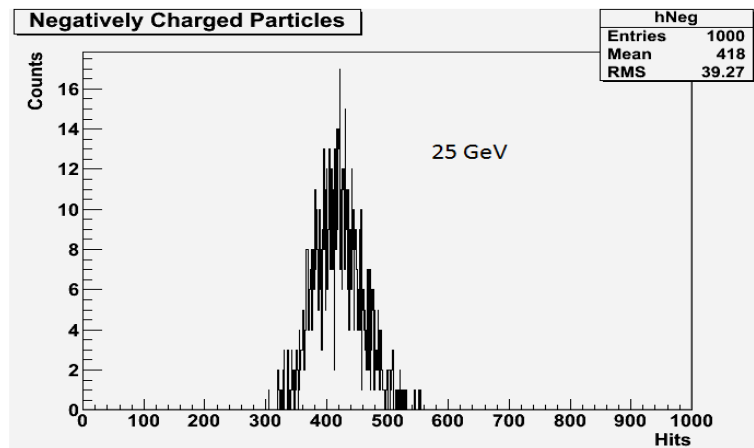

Figure 6.20: *Charge particle multiplicity fluctuations (negatively charged particles) for central Au - Au collisions at 25 GeV.*

Here again, we observe that their is the fluctuations of charge of positively and negatively charged particles from the all charged particles in every energies but the total charge number remains conserved.

6.4   Conclusion

As far as observables of the QCD Critical Point are concerned we have discussed the multiplicity fluctuation of particles and the electric charge multiplicity fluctuations at different FAIR energies of 8 GeV, 10 GeV and 25 GeV. All these have been measured over a wide range of beam energies, from the CERN SPS to RHIC, and none of the excitation functions, with the possible exception of the kaon-to-pion ratio, show any significant beam energy dependence. Concerning the QCD critical point there is only limited theoretical guidance clarifying the relevant beam-energy range for an experimental search. The model predictions for its location in the phase diagram vary quite a bit. It is important to note that a first-order phase-coexistence region might be much easier to detect than the critical point. Both phenomena are equally important for our understanding of the QCD phase diagram. The first-order phase transition corresponds to a large region in the T-ρ phase diagram, and the system most probably spends sufficient time in this region to develop measurable signals. Moreover, fluctuations caused by spinodal instabilities [178]- which are a generic phenomenon of first-order phase transitions - may be much less suppressed by the finite size and the short lifetime of the system, as compared to critical fluctuations. Spinodal instabilities have been studied and successfully identified in the context of the nuclear liquid-gas phase transition [179]. In the case of the QCD first-order transition, spinodal instabilities could lead to kinematic correlations among particles [180] and to enhanced fluctuations of strangeness [181].

Nevertheless, one should keep in mind that the fluctuations and correlations induced by the critical point or by a phase transition may be masked by other effects like impact parameter (or volume) fluctuations, and correlations due to collective flow. Moreover, the signals may be severely degraded by subsequent hadronic processes such as rescattering and resonance interactions and decays. Therefore, the hadronic effects and the background sources should be carefully studied in transport simulations in order to correct the measurements for, and to reveal the primordial

information. However, the existing transport codes need further development before they can reliably treat scenarios where a phase transition is present. This presents several distinct challenges, particularly the following three:

(1) The development of a realistic equation of state that displays the expected phase structure with a first-order phase transition and an associated critical end point at a finite chemical potential.

(2) The ability to describe the change in the active degrees of freedom as the system enters and leaves the deconfined phase region.

(3) The proper dynamical evolution of the system as it encounters the thermodynamic and mechanical instabilities associated with the presence of a phase transition, in particular the growth and further development of the correlated fluctuations that ultimately form the basis for observable signals.

Bibliography

[1] P. Braun-Munzinger and J. Wambach, Rev. Mod. Phys. **81**, 1031 (2009).

[2] M. G. Alford, A. Schmitt, K. Rajagopal and T. Schafer, Rev. Mod. Phys. **80**, 1455 (2008).

[3] N. Yamamoto, M. Tachibana, T. Hatsuda and G. Baym, Phys. Rev. **D 76**, 074001 (2007).

[4] L. D. Landau and E. M. Lifshitz, *Statistical Physics, Third Edition, Part 1* (Butterworth-Heinemann, 1980).

[5] M. A. Stephanov, K. Rajagopal and E. V. Shuryak, Phys. Rev. Lett. **81**, 4816 (1998).

[6] M. A. Stephanov, K. Rajagopal and E. V. Shuryak, Phys. Rev. **D 60**, 114028 (1999).

[7] M. Asakawa, S. Ejiri and M. Kitazawa, Phys. Rev. Lett. **103**, 262301 (2009).

[8] M. A. Stephanov, Phys. Rev. Lett. **102**, 032301 (2009).

[9] H. Fritzsch,and M. Gell-Mann, arXiv: hep-ph/0208010v1 (2002).

[10] G. Dissertori, I. Knowles, and M. Schmelling, *Quantum Chromodynamics - High Energy Experiments and Theory*, (Oxford University Press, 2003).

[11] R. Gupta, arXiv: hep-lat/9807028 (1998).

[12] URL http:// en. wikipedia.org/wiki/Color-Confinement.

[13] A. Pich, arXiv: hep-ph/9505231 (1995).

[14] Leonard Susskind. *Lattice Models of Quark Confinement at High Temperature.* Phys. Rev., **D 20**, 2610-2618, (1979).

[15] I. Arsene et al. (BRAHMS Collaboration), Phys. Rev. Lett. **93**, 242303 (2004).

[16] D. Kharzeev, E. Levin, and L. McLerran, Phys. Lett. **B 561**, 93 (2003).

[17] I. G. Bearden et al. (BRAHMS Collaboration), Phys. Rev. Lett. **93**, 102301 (2004).

[18] I. Arsene et al. (BRAHMS Collaboration), Nucl.Phys. **A 757**, (2005).

[19] J. D. Bjorken, Phys. Rev. **D 27**, 140 (1983).

[20] J. Kapusta, P. Lichard, and D. Siebert, Nucl.Phys. **A 544**, 485 (1992). P. V. Ruuskanen, Nucl.Phys. **A 544**, 169 (1992).

[21] E. L. Feinberg, Nuo. Cim., **34**, 391 (1976) ; E. Shuryak, Phys. Lett. **B 78**, 150 (1978).

[22] K. Kajantie, J. Kapusta, L. McLerran, and A. Mekjian, Phys. Rev. **D 34**, 2746 (1986).

[23] J. Kapusta, P. Lichard, and D. Seibert, Phys. Rev. **D 44**, 2774 (1991).

[24] P. V. Ruuskanen, Nucl. Phys. **A 522**, 255 (1991).

[25] P. J. Siemens, and S. A. Chin, Phys. Rev. Lett. **55**, 1266 (1985).

[26] D. Seibert Phys. Rev. Lett. **68**, 1476 (1992); D. Seibert, V. K. Mishra, and G. Fai Phys. Rev. **C 46**, 330 (1992).

[27] C. Gale, and J. Kapusta, Phys. Rev. **C 35**, 2107 (1987).

[28] F. Karsch, K. Redlich, and L. Z. Turko, Phys. **C 60**, 519 (1995).

[29] U. Heinz, K. S. Lee, Phys. Lett. **B 259**, 162 (1991).

[30] T. Matsui, H. Satz, Phys. Lett. **B 178**, 416 (1986).

[31] F. Karsch, M. T. Mehr, H. Z. Satz, Phys. **C 37**, 617 (1988).

[32] J. Rafelski, and B. Muller, Phys. Rev. Lett. **48**, 1066 (1982).

[33] Y. Aoki et al., Nature **443**, 675 (2006).

[34] M. A. Stephanov, PoS LAT 2006 **024**, (2006); M. A. Stephanov, Int. J. Mod. Phys. **A 20**, 4387 (2005).

[35] E. Laermann, O. Philipsen, Ann. Rev. Nucl. Part. Sci. **53**, 163 (2003).

[36] P. de Forcrand, S. Kim, and O. Philipsen, PoS LAT **178** (2007).

[37] Z. Fodor, and S. D. Katz, JHEP **0404**, 50 (2004).

[38] S. Ejiri, C. R. Allton, S. J. Hands, O. Kaczmarek, F. Karsch, E. Laermann, and C. Schmidt, Prog. Theor. Phys. Suppl. **153**, 118 (2004).

[39] C. Alt et al. (NA49 Coll.), Phys. Rev. **C 77**, 024903 (2008).

[40] V. D. Toneev, E. G. Nikonov, B. Friman, W. N. Norenberg,and K. Redlich, Eur. Phys. J. **C 23**, 399 (2004).

[41] I. C. Arsene, L. V. Bravina, W. Cassing, Yu. B. Ivanov, A. Larionov, J. Randrup, V. N. Russkikh, V.D. Toneev, G. Zeeb, and D. Zschiesche, Phys. Rev. **C 75**, 034902 (2007).

[42] http://www.gsi.de/fair.

[43] *An International Accelerator Facility for Beams of Ions and Antiprotons*, Conceptual Design Report, GSI, Darmstadt, 2001; http://www.gsi.de/GSI-Future/cdr.

[44] http://www.gsi.de/fair/reports/btr.html.

[45] http://www.gsi.de/fair/experiments/NUSTAR/indexe.html.

[46] H Geissel et al, Nucl. Instrum. Methods **B 204**, 71 (2003).

[47] http://www.gsi.de/fair/experiments/superfrs/indexe.html.

[48] http://www.gsi.de/forschung/kp/kp2/nustar.html.

[49] http://www.gsi.de/fair/$index_e$.html.

[50] http://www.gsi.de/fair/experiments/CBM/$indedx_e.html$.

[51] R. Rapp and J. Wambach, Nucl. Phys. **A 661**, 33 c (1999).

[52] C. Blume et al., J. Phys. G: Nucli. Part. Phys. **31**, 685 (2005).

[53] C. M. Hung and E. V. Shuryak, Phys. Rev. Lett. **75**, 4033 (1995).

[54] http://www.gsi.de/fair/experiments/CBM/indedx-e.html.

[55] J. M. Lattimer, and M. Prakash, Pys. Rev. Lett. **94**, 111101 (2005).

[56] UrQMD model, see http://www.th.physik.uni-frankfurt.de/ urqmd/.

[57] A. Sibirtsev, K. Tsushima, and A. W. Thomas, Eur. Phys. J. **A 6**, 351 (1999).

[58] T. Matsui and H. Satz, Phys. Lett. **B 178**, 416 (1986).

[59] D. Gonzalez-Diaz et al.,*Progress in the CBM-TOF Wall, R&D and Simulation*, GSI Report 2007 and 2008.

[60] D. Kresan and C. Hhne, *Event-by-Event Fluctuations of the K/π Yield Ratio in the CBM Experiment, "CBM Progress Report"* 2008 and (2009).

[61] M. Golubeva, et al., Nucl. Instr. Meth. **A 598**, 268 (2009).

[62] A. Ivashkin, *Projectile Spectator Detector in CBM set-up at SIS 300, Talk given on the 1st CBM-Russia-JINR Collaboration Meeting in Dubna*, (2009).

[63] A. Kiseleva, and P. P. Bhaduri et al., Indian J. Phys. **85**, 211-216, (2011).

[64] A. Dubey et al., *R&D with GEMs and THGEMs Towards Developing a Muon Tracker for CBM, "CBM Progress Report"*, 2007 and (2008).

[65] F. Sauli, Nucl. Instrum. Methods Phys. Res. **A 386**, 531 (1997).

[66] F. Sauli, US Patent 6 **011**, 265 (2000).

[67] http://cbmroot.gsi.de.

[68] *Compressed Baryonic Matter Experiment, "Technical Status Report"*, (2005).

[69] V. Peshekhonov et al., *"CBM Progress Report"* 2008, *"GSI Darmstadt Report"* **35**, (2009).

[70] I. Boguslavskiy et al., *"CBM Progress Report"* 2009, *"GSI Darmstadt Report"* **29**, (2010).

[71] K. Davkov et al., Nucl. Instrum. Methods Phys. Res. **A 584**, 285 (2008).

[72] V. Davkov et al., Part. Nucl. Lett., **4**, 545 (2007).

[73] Yu. V. Gusakov et al., Part. Nucl. Lett. **7**, (12), 132 (2010).

[74] S. N. Bazylev et al., Nucl. Instrum. Methods Phys. Res. **A 632**, 75 (2011).

[75] V. I. Davkov et al., Nucl. Instrum. Methods Phys. Res. **A 634**, 5 (2011).

[76] C. Hoehne *Quark Matter Proceedings* J. Phys. G. (2008).

[77] E. Shuryak, Phys. Lett. **B 78** 150 (1978).

[78] H. Satz, Nucl. Phys. **A 661**, 104 (1999); **A 681**, 3 (2001).

[79] M. Asakawa and K. Yazaki, Nucl. Phys. **A 504**, 668 (1989).

[80] Z. Fodor and S. D. Katz, JHEP **0203**, 014 (2002); R. V. Gavai and S. Gupta, Phys. Rev. **D 71**, 114014 (2005).

[81] M. A. Stephanov, K. Rajagopal, and E. V. Shuryak, Phys. Rev. Lett. **81**, 4816 (1998); Phys. Rev. **D 60**, 114028 (1999).

[82] F. R. Brown et al., Phys. Rev. Lett. **65**, 2491 (1990).

[83] M. Asakawa, K. Yazaki, Nucl. Phys. **A 504**, 668 (1989).

[84] A. Barducci, R. Casalbuoni, S. De Curtis, R. Gatto, and G. Pettini, Phys. Lett. **B 231**, 463 (1989); Phys. Rev. **D 41**, 1610 (1990).

[85] A. Barducci, R. Casalbuoni, G. Pettini, and R. Gatto, Phys. Rev. **D 49**, 426 (1994).

[86] S. Jeon and V. Koch, arXiv:hep-ph/0304012.

[87] M. A. Stephanov, K. Rajagopal and E. V. Shuryak, Phys. Rev. **D 60**, 114028 (1999).

[88] B. Berdnikov and K. Rajagopal, Phys. Rev. **D 61**, 105017 (2000).

[89] V. Koch arXiv:0810.2520 [nucl-th] (2008).

[90] M. Asakawa, et al., Phys. Rev. Lett., **101** (2008).

[91] R. V. Gavai, and S. Gupta, Phys. Rev. **D**, 78 2008.

[92] M. A. Stephanov, K. Rajagopal, and E. V. Shuryak, Phys. Rev. Lett. **81**, 4816 (1998).

[93] M. A. Stephanov, K. Rajagopal, and E. V. Shuryak, Phys. Rev. **D 60**, 114028 (1999).

[94] L. Stodolsky, Phys. Rev. Lett. **75**, 1044 (1995); E.V. Shuryak, Phys. Lett. **B 423**, 9 (1998).

[95] S. A. Voloshin, V. Koch, and H. G. Ritter, Phys. Rev. **C 60**, 024901 (1999).

[96] C. Nonaka, and M. Asakawa, phys. Rev. **C 71** 044904 (2005).

[97] M. Asakawa, S. A. Bass, B. Muller and C. Nonaka, phys. Rev. Lett. **101** 122302 (2008).

[98] B. Berdnikov, and K. Rajagopal, Phys. Rev. D, **D 61**, 105017-1 105017-9 (2000).

[99] M. A. Stephanov, Phys. Rev. Lett., **102** 032301-1032301-4 (2009).

[100] M. Asakawa, et al., Phys. Rev. Lett., **103**, 262301-1262301-4 (2009).

[101] Y. Hatta, and M. Stephanov, Phys. Rev. Lett., **91**, 102003-1102003-4 (2003).

[102] M. M. Aggarwal, et al. (STAR Collaboration), Phys. Rev. Lett., **105**, 022302-1-022302-6 (2010).

[103] William Mendenhall, J. Robert Beaver, M. Barbara Beaver, *Introduction to probability and statics* twelfth edition, (THOMSON BROOKS/COLE, 2006).

[104] R. V. Gavai and S. Gupta, phys. Lett. **B 696**, 459 (2011).

[105] F. Karsch and K. Redlich, phys. Lett **B 695**, 136 (2011).

[106] A. Hald, *International statistical review* **68**, 137-153 (2000).

[107] http://en.wikipedia.org/wiki/Skewness.

[108] http://en.wikipedia.org/wiki/Kurtosis.

[109] M. A. Stephanov et al., Phys. Rev. **D 60** 114028 (1999); B. Berdnikov and K. Rajagopal, Phys. Rev. **D 65**, 105017 (2000).

[110] M. A. Stephanov, Phys. Rev. Lett. **102**, 032301 (2009).

[111] C. Athanasiou et al., Phys. Rev. **D 82**, 074008 (2010)

[112] M. Cheng, et al., Phys. Rev. **D 79**, 074505 (2009).

[113] Y. Hatta and M. A. Stephanov, Phys. Rev. Lett. **91**, 102003 (2003).

[114] X. Luo et al., arXiv:1105.5049.

[115] M. M. Aggarwal et al. (STAR Collaboration), Phys. Rev. Lett. **105**, 022302 (2010).

[116] X. Luo et al., J. Phys. G: Nucl. Phys. **37** 094061 (2010).

[117] M. Asakawa et al., Phys. Rev. Lett. **103** 262301 (2009).

[118] B. I. Abelev et al. (STAR Collaboration), Phys. Rev. **C 81** 024911 (2010); STAR Internal Note. **S 493**, (2009).

[119] Y. Hatta and M. A. Stephanov, Phys. Rev. Lett. **91**, 102003 (2003).

[120] M. Asakawa, S. Ejiri and M. Kitazawa, Phys. Rev. Lett. **103**, 262301 (2009).

[121] S. Roessner, C. Ratti and W. Weise, Phys. Rev. **D 75**, 034007 (2007).

[122] B. Stokic, B. Friman and K. Redlich, Phys. Lett. **B 673**, 192 (2009).

[123] C. Miao, C. Schmidt, (RBC-Bielefeld Collaboration), PoS(LATTICE 2008) 172 (2008).

[124] B. Mohanty Nucl. Phys. **A 830**, 899 C-907 C (2009).

[125] Z. Fodor and S. D. Katz, *Critical point of QCD at finite T and μB, lattice results for physical quark masses*, JHEP **0404**, 050 (2006).

[126] S. Afanasiev et al. (NA49 Collab.), *The NA49 large acceptance hadron detector, Nucl. Instrum. Meth.* **A 430**, 210.

[127] M. Stephanov, K. Rajagopal, and E. V. Shuryak, **Event-by-event fluctuations in heavy ion collisions and the QCD critical point**, Phys. Rev. **D 60**, 114028 [hep-ph/9903292].

[128] T. Anticic et al. (NA49 Collab.), *Transverse Momentum Fluctuations in Nuclear Collisions at 158 AGeV*, Phys. Rev. **C 70**, 034902 [hep-ex/0311009].

[129] T. Anticic et al. (NA49 Collab.), *Energy dependence of transverse momentum fluctuations in Pb+Pb collisions at the CERN Super Proton Synchrotron (SPS) at 20A to 158A GeV,* Phys. Rev. **C 79**, 044904[arXiv:0810.5580].

[130] C. Alt et al. (NA49 Collab.), *Centrality and system size dependence of multiplicity fluctuations in nuclear collisions at 158A GeV*, Phys. Rev. **C 75**, 064904 [nucl-ex/0612010].

[131] C. Alt et al. (NA49 Collab.), *Energy Dependence of Multiplicity Fluctuations in Heavy Ion Collisions at the CERN SPS*, Phys. Rev. **C 78**, 034914 [arXiv:0712.3216].

[132] K. Grebieszkow et al. (NA49 Collab.), *Search for the critical point of strongly interacting matter in NA49*, arXiv:0907.4101.

[133] F. Becattini, J. Manninen, and M. Gazdzicki, *Energy and system size dependence of chemical freeze-out in relativistic nuclear collisions*, Phys. Rev **C 73**, 044905 [hep-ph/0511092].

[134] B. Lungwitz, Ph.D thesis, https://edms.cern.ch/document/989055/1 (unpublished) (2008).

[135] Y. Hatta and T. Ikeda, Universality, *the QCD critical/tricritical point and the quark number susceptibility*, Phys. Rev. **D 67**, 014028 [hep-ph/0210284].

[136] Askawa, et al., *Transverse Velocity Dependence of the Proton-Antiproton Ratio as a Signature of the QCD Critical Point*, Phys. Rev. Lett **101**, 122302; Luo et al., *Signature of QCD critical point: Anomalous transverse velocity dependence of antiproton-proton ratio*, Phys. Lett. **B 673**, 268 [arXiv:0903.0024].

[137] J. Adams et al. (STAR Collaboration), Nucl. Phys. **A 757**, 102 (2005); K. Adcox et al. (PHENIX Collaboration), Nucl. Phys. **A 757**, 184 (2005); I. Asene et al. (BRAHMS Collaboration), Nucl. Phys. **A 757**, 1 (2005); B. Back et al., (PHOBOS Collaboration), Nucl. Phys. **A 757**, 28 (2005).

[138] S. Blyth et al. (STAR Collaboration), J. Phys. G. **34**, 5933 and references therein.

[139] J. Cleymans et al., Phys. Rev. **C 73**, 034905 (2006).

[140] M. Asakawa et al., Phys. Rev. Lett. **101**, 122302 (2008).

[141] S. V. Afanasiev et al. (NA49 Collaboration), Phys. Rev. **C 66**, 054902 (2002); C. Alt et al. [NA49 Collaboration], Phys. Rev. **C 68**, 034903 (2003); C. Roland et al. [NA49 Collaboration], J. Phys. G 30, **S 1381** (2004).

[142] F. Karsch and K. Redlich, Phys. Lett. **B 695** (2011).

[143] R. Gavai and S. Gupta, Phys. Lett. **B** (2011).

[144] R. Brun, F. Rademakers, P. Canal, I. Antcheva, D. Buskulic, O. Couet, A. and M. Gheata ROOT User Guide (CERN,Geneva,) 2005.

[145] R. Brun, F. Carminati, I. Hrivnacova, A. Morsch, *The Virtual Monte Carlo Computing in High Energy and Nuclear Physics*, 24-28 March 2003, La Jolla, California (2003).

[146] http://www-hades.gsi.de/computing/pluto/html/PlutoIndex.html

[147] S. A. Bass, M. Belkacem, M. Bleicher, M. Brandstetter, L. Bravina, C. Ernst, L. Gerland, M. Hofmann, S. Hofmann, J. Konopka, G. Mao, L. Neise, S. Soff, C. Spieles, H. Weber, L. A. Winckelmann, H. Stocker, W. Greiner, Ch. Hartnack, J. Aichelin, and N. Amelin, Prog. Part. Nucl. Phys. **41**, 225 (1998).

[148] B. Andersan, G. Gustafson and B. Nilsson-Almqvist, Nucl. Phys. **B 281**, (1987).

[149] B. Nilsson-Almqvist and E.stenlund, Comput. Phys. Common. **43** 387 (1987).

[150] T. Sjostrand, comput. Phys. Commum. **82** (1998).

[151] T. Sjostrand, comput. Phys. Commun. **39** (1986).

[152] I. Frohlich et al., PoS ACAT2007, **076**, (2007).

[153] G. Agakishiev et al. (The HADES Collaboration), arXiv:0902.3478 [nucl-ex].

[154] http://root.cern.ch.

[155] M. A. Kagarlis, GSI Report 2000-03 (2000), unpublished.

[156] http://wwwhades.gsi.de/computing/pluto/html/PlutoIndex.html

[157] G. Agakichiev et al., Phys. Rev. Lett. **98** 052302 (2007).

[158] P. Senger, J. Phys. G: Nucl. Part. Phys. **S 1087**, 30 (2004).

[159] B. Andersson, A. Tai, and Ben-Hao Sa, *"final state interactions in the (nuclear) FRITIOF string interaction scenarion"*, Z. Phys. **C 57**, 485 (1993).

[160] W. Ehehalt and W. Cassing, *" Relativistic transport approach for nucleus-nucleus collisions from SIS to SPS"*, Nucl. Phys. **A 602** 449 (1996).

[161] J. Geiss, W. Cassing and C. Greiner, *"Strangeness production in the HSD transport approach from SIS to SPS energies"*, Nucl.Phys. **A 644** 107 (1998).

[162] W. Cassing and E. L. Bratkovskaya, *"Hadronic and electromagnetic probes of hot and dense nuclear matter"*, Phys. Reports **308**, 65 (1999).

[163] B. Andersson, G. Gustafson, H. Pi, Z. Phys. **C 57**, 485 (1993).

[164] T. Sjostrand, Comput. Phys. Commun. **82**, 74 (1994).

[165] W. Cassing, S. Juchem, Nucl. Phys. **A 672**, 417 (2000).

[166] W. Cassing, (2005). URL http://conferences.jlab.org/ECT/program.

[167] A. Peshier, W. Cassing, Phys. Rev. Lett. **94**, 172301 (2005).

[168] W. Cassing, Nucl. Phys. **A 791**, 365 (2007).

[169] I. Kisel, *Event Reconstruction in the CBM experiment* Nucl. Instr. Meth. **A 566**, 85-88 2006.

[170] R. Kalman, *A New Approach to Linear Filtering and Prediction Problems*, Transactions of the ASME: J. of Basic Engine. Ser. **D 82**, 35-45 (1960).

[171] R. Fruhwirth, *Application of Kalman Filtering to Track and Vertex Fitting* Nucl. Instr. Meth. **A 262**, 444-450 (1987).

[172] A. Lebedev, G. Ososkov. *LIT Track propagation for CBM.* CBM Note. Darmstadt, 2008; https://www.gsi.de/documents/DOC-2008-Dec-182-1.pdf.

[173] A. Lebedev et al. *Track Reconstruction and Muon Identification in the Muon Detector of the CBM Experiment at FAIR* PoS. ACAT **08**, 068 (2008).

[174] *Compressed Baryonic Matter Experiment.* Technical Status Report, GSI, Darmstadt, (2005).

[175] M. A. Stephanov, Int. J. Mod. Phys. **A 20** 4387 (2005); B. Mohanty, Nucl. Phys. **A 830** 899 c (2009).

[176] http://cbmroot.gsi.de

[177] https://subversion.gsi.de/fairroot/release/DEC09.

[178] P. Chomaz, M. Colonna, J. Randrup, Phys. Rept. **389**, 263 (2004).

[179] B. Borderie, et al. (INDRA Collaboration), Phys. Rev. Lett. **86**, 3252 (2001)

[180] J. Randrup, Acta Phys. Hung. **22**, 69 (2005).

[181] V. Koch, A. Majumder, J. Randrup, Phys. Rev. **C 72**, 064903 (2005).